SDI

SDI

MAY 2 1969

THE UNIVERSITY OF MICHIGAN
RADIO ASTRONOMY OBSERVATORY

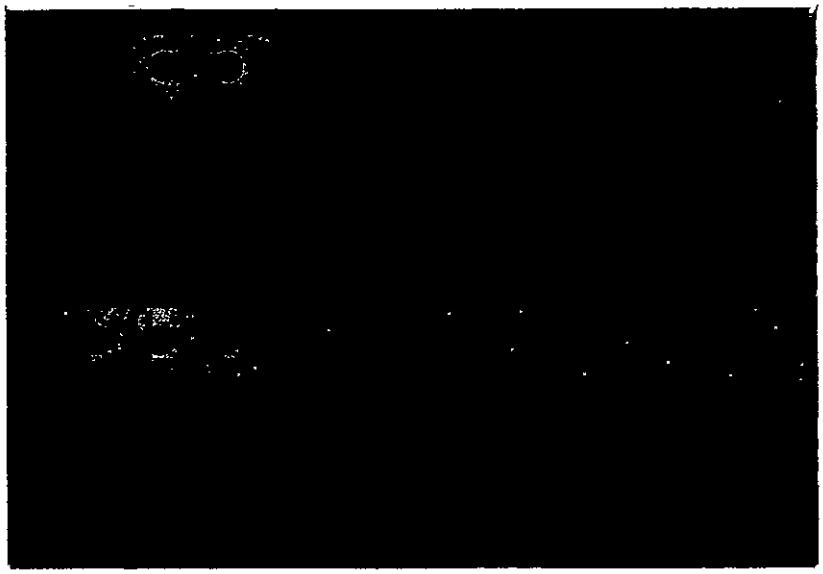

DEPARTMENT OF ASTRONOMY

DYNAMIC SPECTRA OF 4-2 MHZ SOLAR BURSTS: RESULTS FROM ORBITING GEOPHYSICAL OBSERVATORY III

Thomas E. Graedel

NASA Contract NA5-2051

Final Report, Part I: Scientific

ACKNOWLEDGEMENTS

I am greatly in the debt of Professor Fred T. Haddock for allowing me to use data from a space experiment which he conceived, and for which he directed the development, and for the direction of and discussions concerning this dissertation He and the staff of the University of Michigan Radio Astronomy Observatory have demonstrated a consistently high standard of scientific and engineering competence from the initial design stage of the experiment to the resulting analysis of the experimental output In particular I wish to acknowledge the efforts of Dr. Lyman Orr for initial design and breadboarding of the experiment, Mr W J Lindsay for supervising the development of the experiment hardware, Mr R G Peltzer for following the payload through spacecraft integration and test, and for many helpful discussions regarding the experiment, Mr C.E Lindahl and Mr D.W. Wyche for the initial concept and development of data processing techniques and programs, and Mr B D MacRae for discussions regarding the calibration of the UM/RAO experiment aboard the OGO-V spacecraft

The UM/RAO experiment aboard OGO-III was funded by the National Aeronautics and Space Administration under contract number NA5-2051 I acknowledge with thanks the support provided through the contract

PREFACE

The scientific research described herein was performed under the direction of Professor Fred T. Haddock, Principal Investigator for NASA Contract NA5-2051. This document constitutes the final scientific report for the contract. As presented here, the report was submitted by the author to the Horace H. Rackham Graduate School of The University of Michigan, in partial fulfillment of the requirements for the degree of Doctor of Philosophy.

The engineering aspects of this program will be published separately, as Part II of the final contract report.

The task of correlating the spacecraft data with the optical features of the sun was accomplished at the McMath-Hulbert Observatory of the University of Michigan I am grateful to Dr Helen D. Prince and her staff for allowing me the use of their comprehensive and carefully assembled records concerning the daily behavior of the sun, and for many helpful discussions

Professor Herschel Weil has willingly discussed with me problems of plasma physics and of antenna theory which were relevant to proper treatment of the data. His comments have resulted in an improved analysis

Drs Orren C Mohler and Richard G. Teske read critically the first draft of the manuscript. I am indebted to them for suggestions and comments which have greatly improved the final document

My entire program of graduate study, including this dissertation research, has greatly benefitted from numerous discussions with my fellow graduate students. In this regard, I wish to specifically thank George W Brandie, Michael J Klein, and Roger J. Thomas for their assistance

Finally, I express my special thanks to my wife, Susannah, who has been of great assistance in typing and proof-readings of the early drafts of this work, and has been unfailingly encouraging and helpful.

TABLE OF CONTENTS

LIST OF TABLES

LIST OF ILLUSTRATIONS

CHAPTER I

INTRODUCTION

In 1950, Wild published a series of classic papers describing the properties of solar radio bursts at meter wavelengths, and separating them into distinct classes (Wild and McCready, 1950, Wild, 1950). His observations over the frequency range 120-70 MHz were the first to be made with a sweep-frequency radiometer, and confirmed the frequency drifting of the bursts previously suggested by Payne-Scott, Yabsley, and Bolton (1947) Subsequent observations extended the frequency range from 4000 MHz (Kundu and Haddock, 1961; Thompson and Maxwell, 1962) to 5 MHz (Sheridan and Attwood, 1962) This latter frequency is the cutoff imposed by the earth's atmosphere.

Interferometric observations of fast drift bursts (Wild's Type III) at a number of frequencies have clearly demonstrated that the frequency of emission is inversely proportional to the distance of the emitting region from the solar surface These observations are satisfactorily explained as emission which occurs chiefly at the local plasma frequency Because of the decrease in electron density with increasing radial distance from the sun, low-frequency solar radio bursts originate from very great heights in the corona

The development of spacecraft as scientific experiment platforms provided the means for gathering radio burst data at frequencies below the ionospheric cutoff As early as 1960 a radio astronomy experiment was proposed by the University of Michigan Radio Astronomy Observatory, under the direction of Professor Fred T Haddock, for the Orbiting Geophysical Observatory Series OGO-I, with the experiment aboard, was launched in September, 1964 The spacecraft failed to deploy its appendages fully and to orient itself automatically toward the sun The attempt to extend the radio astronomy antenna about 15 days after launch was apparently unsuccessful No evidence of solar bursts has been obtained from OGO-I The first reported low-frequency solar burst observations from spacecraft were made using ionospheric sounder data from Alouette I at several discrete frequencies in the 10-1 5 MHz range (Hartz, 1964) The amount and quality of low-frequency solar radio burst data were greatly increased two years later with the successful operation of the University of Michigan sweep-frequency experiment on OGO-III The data from the OGO-III experiment constitute the observational base of this dissertation. The University of Michigan Radio Astronomy Observatory eight-channel radiometer aboard OGO-V, which was launched in March, 1968, has since detected solar bursts to frequencies as low as 100 kHz

The OGO-III spacecraft was placed into an elliptical orbit about the earth, with apogee at approximately 19 earth radii. Such an orbit minimized the data loss by ionospheric effects and occultation of the sun by the earth, thus permitting essentially twenty-four hour operation. The antenna used was a thirty-foot whip with a near-dipole radiation pattern, feeding a radiometer which swept over the 4-2 MHz band every two seconds. Because of the high radio noise conditions in the spacecraft environment the dynamic range of the equipment was reduced from 60 db to 30 db

The solar radio burst data analyzed in this paper constitute the first large sample at low frequencies, and are the only low-frequency data obtained thus far by sweep-frequency techniques. For the period June 7, 1966 to September 30, 1967, 218 solar bursts were detected by the experiment Analysis has shown that nearly all are of the fast drift type Type V continuum radiation, which has been observed to follow fast drift bursts on occasion at higher frequencies, has been seen on the OGO-III data Type I solar noise storms are possibly present in a few cases Types II and IV have not been observed

The availability of the OGO-III data in digital form has permitted detailed quantitative analysis of the bursts at selected frequencies. The burst data are plotted as a graph of output voltage against time; such a single-frequency plot is referred to hereafter as a "radio burst profile" or simply a "profile". These profiles

allow accurate determinations of the burst durations, drift rates, flux densities, and other properties, with greater accuracy than is normally achieved by analyses of analog sweep-frequency records of solar bursts

Chapter II of this dissertation describes the OGO-III spacecraft and the radio astronomy experiment The observed properties of the solar radio bursts are described and illustrated in Chapter III. Chapter IV reviews the current state of knowledge regarding the physical conditions of the corona at distances greater than 3 $R_\odot$ ($R_\odot$ = solar radius), the characteristics of solar particle bursts, and the properties of fast drift radio bursts as measured by other observers In this chapter the evidence for the plasma frequency burst hypothesis is also reviewed, and it is concluded that the solar burst radiation observed by OGO-III originates from coronal distances of 5. 3 to 6 3 $R_\odot$ In Chapter V various theoretical models for fast drift solar radio bursts are reviewed The growth and development of the bursts is then studied as a function of the burst emission bandwidth, the time scale of the electron injection, and the temperature of the region from which the burst originates. This appears to be the first attempt to study the combined effects of these factors on the development of radio bursts, and has permitted a consistent derivation of their values. Finally, Chapter VI compares the observational results with the properties of fast drift bursts at higher frequencies, and relates the bursts to the plage regions on

the sun from which the electron streams responsible for the bursts originate. Implications of this work with respect to the density and temperature structure and the morphology of coronal streamers are also discussed in the final chapter.

CHAPTER II

THE OGO-III RADIO ASTRONOMY EXPERIMENT

A The Spacecraft and Its Characteristics

Orbiting Geophysical Observatory III, depicted in Figure 1, is a rectangular aluminum panelled box weighing approximately 1125 pounds, including a total experiment weight of approximately 150 pounds Two solar arrays with Solar Oriented Experiment Packages (SOEP), experiment booms, two telemetry antennas and one experiment antenna are included in the major appendages of the spacecraft

In its design configuration following full deployment, OGO-III utilizes reaction wheels and gas jets to maintain an attitude with respect to the sun, earth and orbital plane such that its solar paddles are normal to the sun-spacecraft line and the telemetry antenna pointing is parallel to the earth-spacecraft line.

The spacecraft orbit selected enabled the vehicle to traverse the Van Allen radiation belts twice during each orbit and to make geophysical measurements from near the earth to the region of cislunar space. The initial orbit achieved by OGO-III was very near that specified, with orbital elements summarized in Table 1:

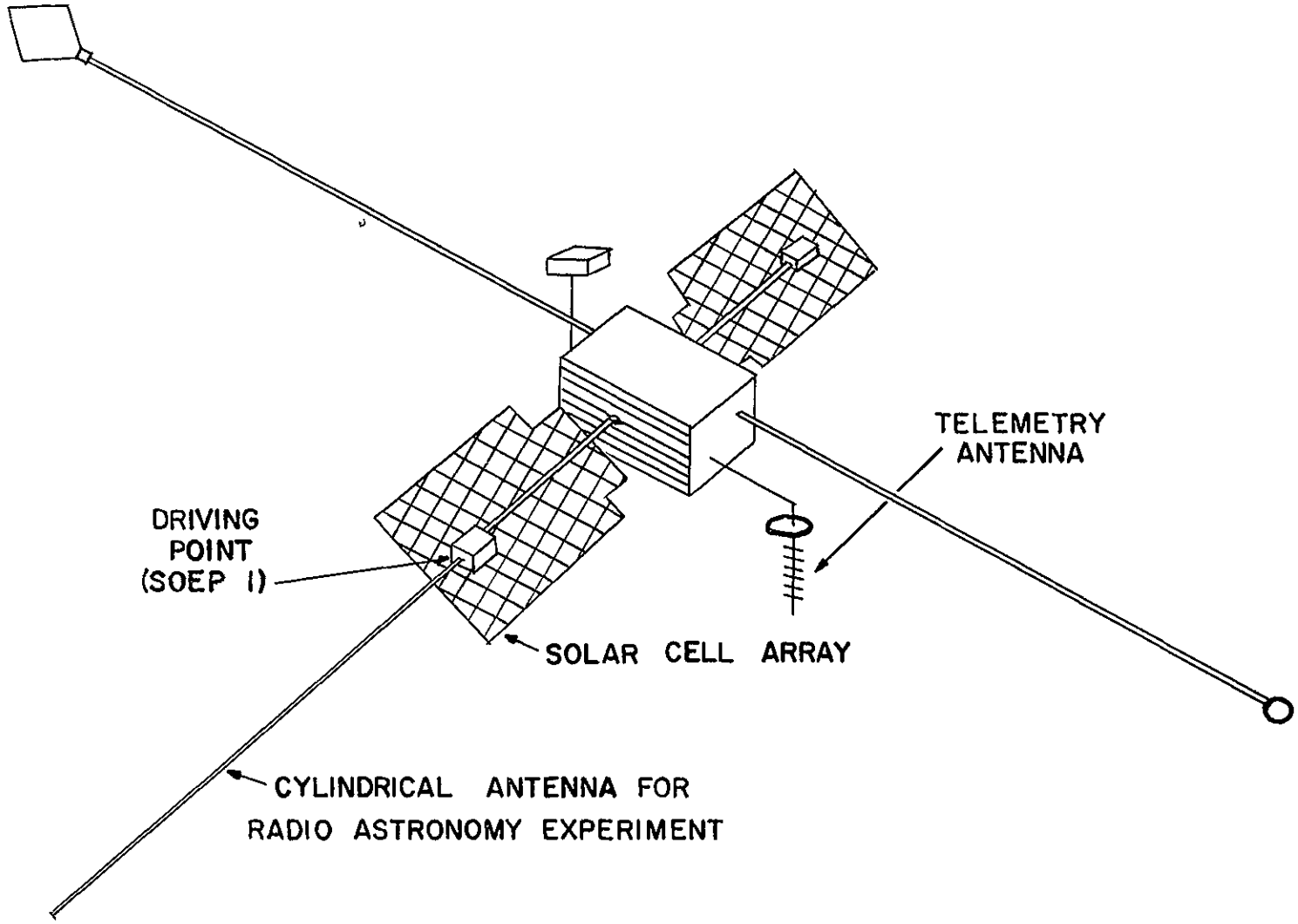

Figure 1 The OGO-III Spacecraft.

Semi-Major Axis	67635 km
Eccentricity	0.90133
Inclination	30.976°
Mean Anomaly	0.109°
Argument of Perigee	312.368°
Motion +	0 1005°/day
R.A. of Asc Node	101.008°
Motion -	0.0643°/day
Anomalistic Period	2917.5 min (48.6 hr)
Height of Perigee	295.3 km
Height of Apogee	122219 km
Velocity at Perigee	38365 km/hr
Velocity at Apogee	1991 km/hr

Table 1. OGO-III Orbital Elements, June 7, 1966.

The gravitational fields of the earth, moon, and sun exert a continuous force on the spacecraft which gradually alters the orbital elements. The combined effect has been to decrease the eccentricity of the orbit; thus the apogee distance decreases and the perigee distance increases somewhat with time. By October 11, 1967, some sixteen months after launch, the eccentricity was 0.8623, and perigee and apogee distances were 2924 km and 119435 km, respectively. These changes have no detectable effects on the burst radiation received by the radio astronomy experiment, which is insensitive to

orbital position except for the brief periods of time spent within the earth's ionosphere, or when occulted by the ionosphere.

The data acquisition and transmission capability of the spacecraft was designed with the options of real time telemetry or playback telemetry In the real time mode the spacecraft can transmit data at rates of 64000, 8000 or 1000 bits per second (64, 8 and 1 "kilobits per second", abbreviated "kb"), subject to the equipment constraints of the ground stations in line-of-sight at the time of transmission. When operating in playback mode, the spacecraft records data on one of its two on-board tape recorders at the rate of 1 kb, and transmits this record to a ground station on command, at the rate of 64 kb Since the second tape recorder can be operating during this transmission, it is possible to obtain continuous data coverage throughout the orbit, even when ground receiving stations are not in line-of-sight view.

B The Radio Astronomy Experiment Package

1 Concept of the Experiment

The purpose of the University of Michigan Radio Astronomy Observatory OGO-III Experiment Package is to measure the radio bursts incident upon an electrically short antenna in the frequency band 4-2 MHz, with the objective of studying solar (and possibly Jovian) radio bursts at these frequencies

2 The Sweep-Frequency Radiometer

The receiver is of the electrically tuned sweep-frequency transistorized type, with a two-second sweep period synchronized by alternate one second clock pulses from the spacecraft. The receiver bandwidth is 10 kHz, and the dynamic response approximately 60 db Primary power for the receiver is 1.75 watts and is provided by the spacecraft The block diagram of the receiver is shown in Figure 2.

The first stage of the receiver (Figure 3) is located with the antenna and its associated erection mechanism in SOEP #1, on one of the solar arrays of OGO-III. This unit is composed of a radio-frequency (rf) amplifier stage and a mixer stage with local oscillator. Frequency tuning is accomplished by use of voltage tunable elements in the tuned circuits.

The second stage of the receiver (Figure 4) is located in the main body of the spacecraft. It consists of an intermediate-frequency (if) amplifier, detector and automatic gain control (AGC) unit. The AGC unit is a cascade of synchronously tuned amplifier stages driving a suitable detector. The amplifier stages are gain controlled by AGC to provide the desired dynamic range.

The total weight of the receiver is 2 25 pounds Dimensions of the containers are 1 inch by 2 5 inches by 6 inches (first stage) and 2 inches by 6 inches by 8 inches (second stage)

The detector output is a signal which varies over the range 0 to +5 volts, as a function of the radiation flux incident on the antenna.

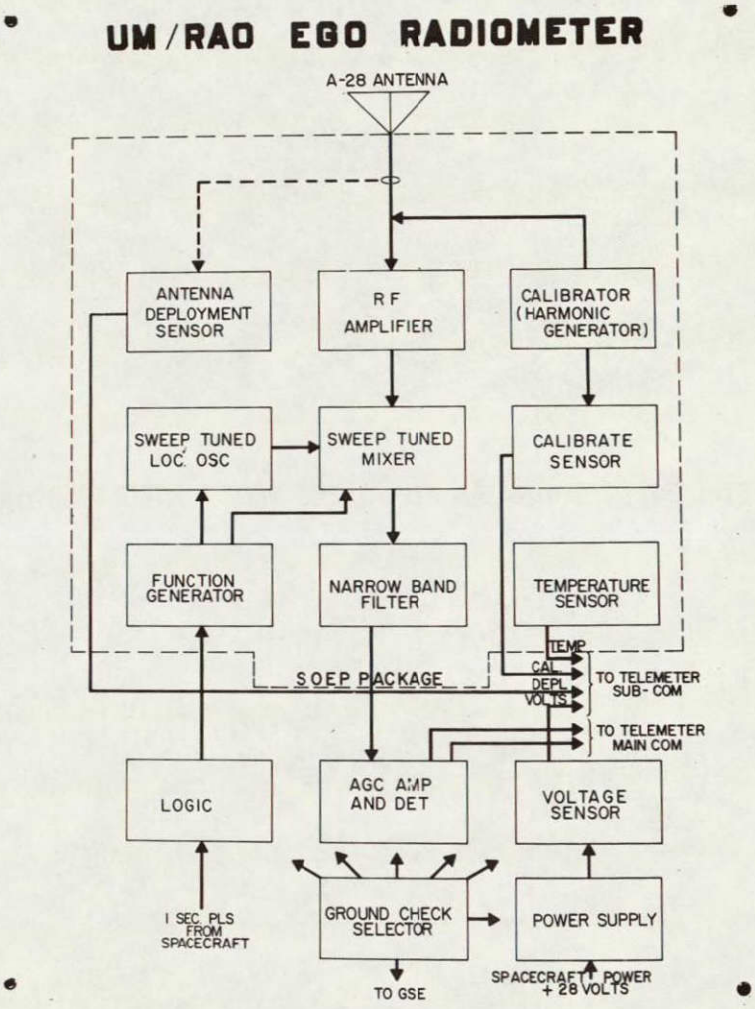

Figure 2. Block Diagram of the Radio Astronomy Instrument Package. (UM/RAO Chart)

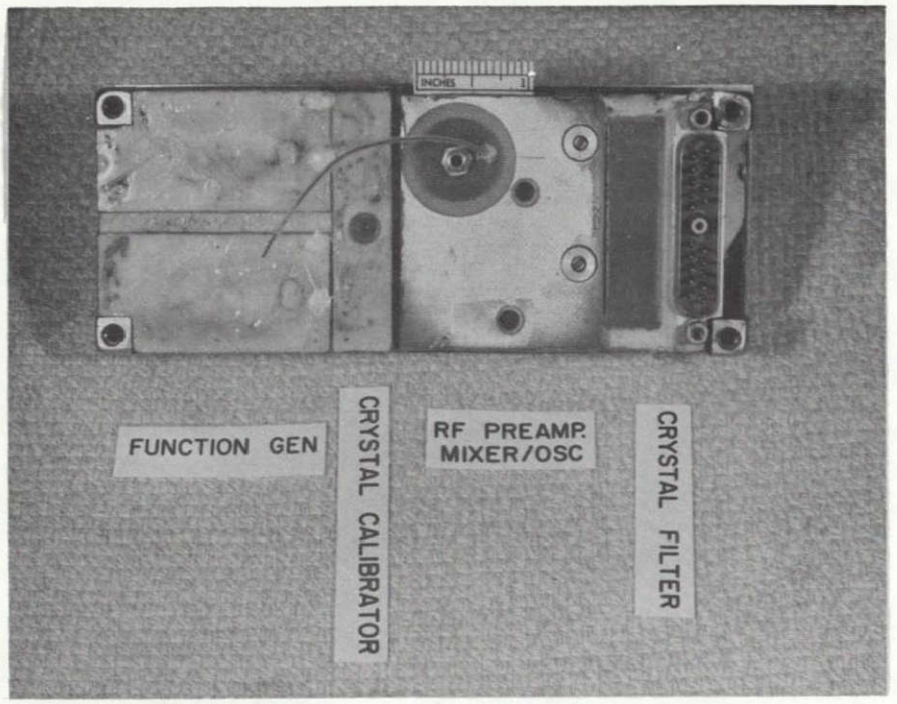

Figure 3. The First Stage Electronics. (UM/RAO Photograph)

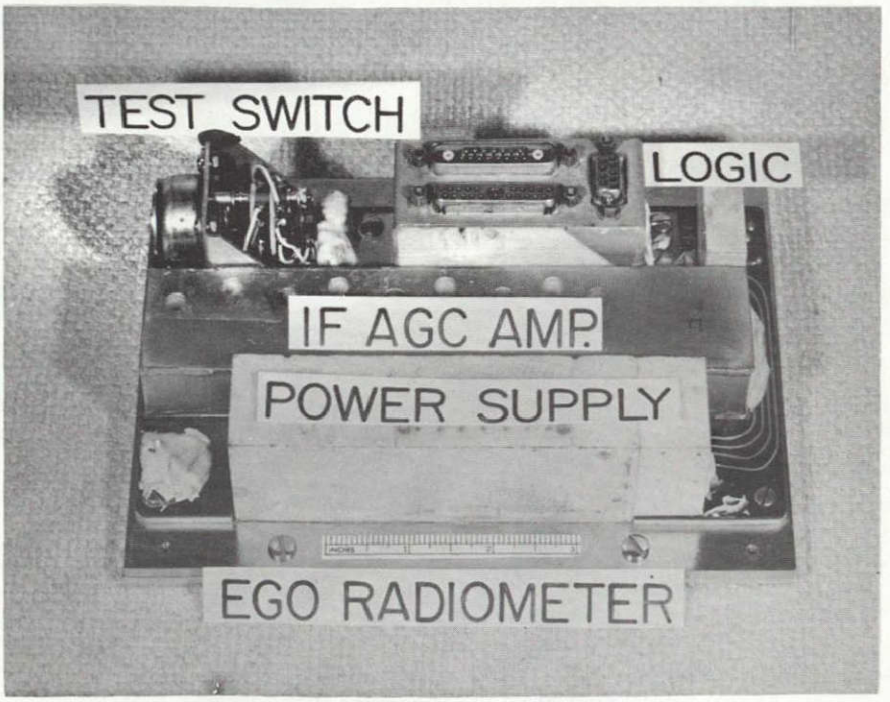

Figure 4. The Second Stage Electronics. (UM/RAO Photograph)

The voltage as a function of time (and of frequency, as a result of the sweeping feature of the radiometer) is transmitted to ground stations. The calibration of the output signal is discussed later in this chapter.

3 The Antenna and Its Reception of Radiation

The OGO-III antenna was constructed of beryllium copper, pre-stressed to a cylindrical shape, and then wound onto a spool in the form of a thirty-foot long strip After the spacecraft had been successfully inserted into orbit, a ground command activated the antenna motor, thus deploying the antenna from the spool. The pre-stressing caused the deployed antenna to assume the standard shape of a long cylindrical antenna.

The effective antenna pattern for the OGO-III antenna was similar to that of a standard asymmetric dipole, because of the negligible ground plane provided by the spacecraft. For a symmetric short dipole the radiation resistance is given by

$$R_r = 30 (\pi L/\lambda)^2$$

The OGO-III antenna (and that of the subsequently launched OGO-V) was 9.15 meters long. Thus at 3.5 MHz (λ = 85.7 m),

$$R_{rd} = 3.4 \text{ ohms}$$

The deviation of the antenna from a perfect dipole causes the radiation resistance to be reduced somewhat from this value In the best judgment of Radio Astronomy Observatory personnel,

$$R_r \text{ (OGO-III)} = 2.8 \text{ ohms}$$

4 Evaluation of Incident Flux Density

The flux density of a solar radio burst may be related to the antenna temperature by the standard equation

$$S_\nu = \frac{4\pi K T_A}{\lambda^2 G} ,$$

where K is Boltzmann's constant and G is the gain of the antenna The determination of T_A is discussed later in this chapter

C. Calibration of the Experiment

1 The Calibration Concept

The radio astronomy experiment aboard OGO-III was conceived as a scanning or monitoring instrument As such it was concerned primarily with relative intensity measurements over its reception band Such an instrument is similar to most ground-based sweep-frequency receivers, with two important exceptions. First, the sweeping rate was slow enough that the time constant did not materially affect an output measurement over a narrow frequency band Second, the data as received were already in digital form It was thus possible to get an accurate value for the output voltage as a function of frequency at a particular time, and the problem was reduced to one of determining the transfer function for the system between the flux density incident on the antenna and the output voltage

Accurate determination of the system transfer function requires knowledge of the antenna impedance This parameter was not measured in flight by the OGO-III experiment and had to be estimated in order that the transfer function might be specified An improved means of calibration became available in the spring of 1968 with the launch of OGO-V on March 4. This spacecraft carried a University of Michigan Radio Astronomy Observatory eight-channel stepping radiometer, with the highest frequency channel at 3. 5 MHz The antenna and its mounting were identical to those of OGO-III A combination of good bench testing, complete measurement of electrical parameters after installation on the spacecraft, and an in-flight noise calibrator permitted specification of the characteristics of the equipment within reasonable limits (MacRae, 1968) For selected intervals, quick-look data from OGO-V and real time data from OGO-III were processed A comparison showed two solar radio bursts which were common to both experiments It was then possible to estimate a calibration for OGO-III by using the approximate OGO-V calibration and assuming an equal flux density of radiation at 3 5 MHz at both spacecraft

2 Bench Calibration of the OGO-III Receiver System

a Calibration Techniques

Two distinct calibration setups were used for bench testing. In the "static" calibration a fixed frequency signal was introduced through a dummy antenna to the radiometer front end, and the output fed to an oscilloscope. This setup was used to measure several

specific parameters of the equipment, including the dynamic range for a single frequency input, and the rise and fall time constants

The test setup for the "dynamic" calibration was much more elaborate The noise source used was that initially designed for testing the radio astronomy experiment aboard OGO-II (POGO) It produced white noise, flat to within 1 db from 100 kHz to 3 5 MHz, falling off slightly outside those limits The noise-diode current and noise-amplifier gain were constant, so that a signal of constant voltage was fed to an attenuator bank. The attenuators acted to simulate radio bursts of different flux density levels by decreasing the noise signal by measured amounts. The antenna was represented by a fixed resistance and five capacitances The latter were used because the characteristics of the antenna in free space were unknown. From the dummy antenna the signal was fed to the radiometer.

The radiometer outputs were connected to 22 kHz and 70 kHz voltage-controlled oscillators (VCOs). In order to determine accurately the beginning and the end of a sweep period, the two-second sweep multivibrator output of the radiometer was fed into a 14 5 kHz VCO. The outputs of the VCOs were then added in a resistive mixer, and the resultant composite signal recorded redundantly on a tape recorder. The calibration information was recovered by playback of the magnetic tape, with the output of one of the direct-record channels fed through the appropriate set of discriminators to a chart recorder.

The radiometer output was calibrated by injecting a number of precisely known voltages into the VCO system in place of the radiometer signal This permitted recovery of an output voltage from the system during noise calibration which represented the system transfer function at specific values of the noise voltage, attenuation, and ambient temperature.

From the dynamic calibration it is possible to construct the transfer function for the radiometer In practice this is expressed as the output voltage produced by a constant white noise signal under specific levels of attenuation. The time and frequency limits of the sweep are also derived from this calibration

The characteristics of the radiometer as derived from calibration data are discussed in detail in the following paragraphs.

b Dynamic Range

The dynamic range of the instrument is very nearly 60 db, independent of temperature, although the response within that range varies slightly with the thermal conditions. The voltage output for the top 30 db of range is 3 0 - 4 2 volts. Below this range, the data obtained in flight were obscured by radio frequency noise generated aboard the spacecraft. The actual dynamic range over which observations took place, therefore, was approximately 30 db.

c. Time Duration of Sweep

The duration of the frequency sweep of the instrument was measured against a crystal reference oscillator. The design value of 2 seconds was reproduced consistently to within 1 msec.

d. Rise and Fall Time Constants

The radiometer time constants were measured by injecting a square-wave signal into the radiometer, and photographing the oscilloscope-displayed output At 25 ^{o}C the measured values are

$$t_{rise} = 0.91 \text{ msec}$$
$$t_{fall} = 3.15 \text{ msec}$$

These values vary by about 20% and 5%, respectively, at the extremes of temperature operation of the experiment aboard the spacecraft Since all known types of low-frequency burst activity have durations of several minutes or longer, the rise and fall time constants do not significantly influence the measurements

e Frequency Limits

The center frequency of the radiometer at the beginning and end of each sweep was determined by injecting a signal with frequency spikes every 100 kHz into the radiometer. The output signal thus contained a peak every 100 kHz in addition to the radiometer keying signal every 500 kHz The measured frequency range for full-sweep operation was 2330 kHz, extending from 4150 kHz to 1820 kHz. In the half sweep mode, the limits were 4150 kHz and 2980 kHz,

respectively There were no measurable differences in these values attributable to changes in local thermal conditions

f. Response Curve

Derivation of the flux density from a solar burst, based upon the radiometer output voltage, requires the specification of the transfer function of the entire radiometer/antenna package. In its most convenient form, this will be given as a graph of the flux density as a function of equipment output voltage. This curve is not directly available for the OGO-III experiment It is possible, however, to specify its shape using the measurements of output voltage as a function of signal attenuation which were made during the testing. With the form of the curve known, determination of one point on the curve with known flux density would fix the zero-point of the entire response curve.

3 Joint OGO-III/OGO-V Calibration

The procedure for calibrating the OGO-III radiometer through the use of the OGO-V equipment was based on the assumption that the flux densities observed by both spacecraft for the same solar radio burst were equal The 3 5 MHz frequency was common to both radiometers and, for the two bursts observed in common, solar radial distance differences were negligible. The use of this approach results in a calibration which is strictly valid only for the 3 5 MHz common frequency The time-voltage plots for each spacecraft were constructed for each common burst from the data, and those of OGO-V converted to time-T_A plots through the use of the OGO-V calibration

curve Comparison with the OGO-III time-voltage plots then permitted an OGO-III calibration to be derived. By using the full range of observed flux density values, the OGO-III instrument was calibrated over its total observed voltage range The result of this joint calibration was that the limits of detectable solar burst radiation for the OGO-III experiment were

$$2\ 8 \times 10^{-19} \leq S_{\nu} \leq 1\ 06 \times 10^{-15} \text{ watt m}^{-2}\text{Hz}^{-1}$$

D Data Processing

1 Analog-to-Digital Conversion and Data Telemetry

The data acquired by the radio receiver are measurements of only one parameter directly connected with the incident radiation at a given frequency, i e , the instantaneous voltage across the antenna terminals This voltage is amplified in the first stage electronics and passed to the second stage Here amplification and detection of the signal take place, and an analog-to-digital conversion is performed. The digital output is then sampled by the spacecraft data system at one of three predetermined rates, and telemetered to ground-based data receiving stations.

It is enlightening to examine the telemetry process more closely. At the 1 kb data collection rate the main commutator frame, containing 128 eight-bit channels, is sampled by the spacecraft system every 1. 152 seconds. The channel time interval is thus 1152/128 = 9 milliseconds and the i-th channel lags behind the first

channel starting time by 91 milliseconds Channel assignments to the radio astronomy experiment were 8, 26, 45, 64, 85, 103 and 120, giving lag times of 72, 184, 405, 576, 765, 927 and 1080 milliseconds, respectively. A true picture of the frequency sampling by the experiment requires that these values be correlated with the 2000 millisecond sweep period of the radiometer Reference to Figure 5 shows that complete frequency coverage requires 26 sweeps of the radiometer or a total of 52 seconds of observing time, and that some frequency pockets are filled redundantly by the data handling process during this period

The radio astronomy experiment package was designed with the response characteristics necessary to permit sampling data at the spacecraft telemetry rates of 1, 8 and 64 kb. This gives fourteen data samples per two-second radiometer sweep at the 1 kb rate, 112 samples at 8 kb and 896 samples at 64 kb With a system bandwidth of 20 kHz, the result is an eightfold redundancy at 64 kb, a nearly complete sampling at 8 kb, and a spotty sampling at 1 kb

In each data channel eight bits are available for data transmission, so that a maximum of 256 variations in the digital output can be transmitted. Since the radio astronomy experiment was designed to produce an output voltage in the range $0 \text{ v} \leq v_o < 5 \text{ v.}$, each datum increment represents approximately 0 02 volts This is a technical constraint on the accuracy of the experiment, but, as discussed in the previous section, it is not the controlling limit.

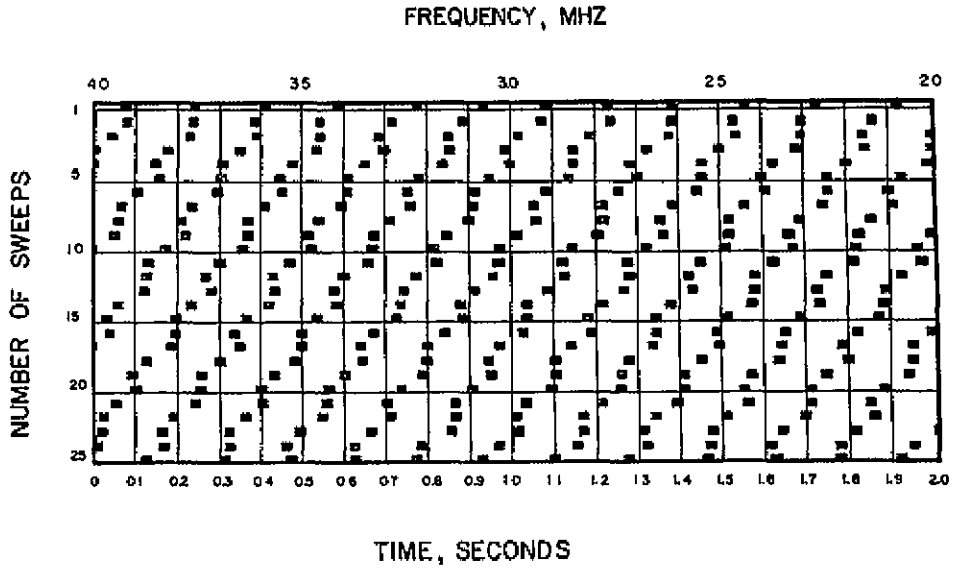

Figure 5. Frequency Coverage as a Function of Number of Sweeps for OGO-III Main Commutator Channel Assignments. (Adapted from a UM/RAO Chart by W. J. Lindsay)

Telemetered data are received by one or more of eight existing ground stations which are in the line-of-sight of the spacecraft. Small antennas and associated equipment at some of these stations limit the transmission data rates. The data received at these stations are recorded on magnetic tapes, which are transferred to the Goddard Space Flight Center for detailed processing

2 The NASA Experimenter's Data Format

Data tapes from ground receiving stations are processed at Goddard on a Univac 1108 computer line. It is at this point that data quality is checked, and the data from the different experiments aboard the spacecraft separated. A tape is made for each experimenter. Each tape contains information concerning spacecraft parameters of interest, time designators and data quality indicators, and the data from the individual experiment.

The radio astronomy data tapes contain from one to six files of information. Each file includes one label record of fixed length. The label record format is standard for all experimenters It contains, among other items, the day and year of observation, the starting time of the observation in seconds, the data rate used and the NASA designation of the master tape from which the data were generated. The data record format was specified by the University of Michigan Principal Investigator. It includes the starting time of the observation in milliseconds, the ambient temperature of the two electronics packages and repeated samplings of the radiometer output

Magnetic tapes recorded in the format described are intentionally generated in a form which does not specify the subsequent method or concept of data processing In the case of this experiment, the flexible format permitted transfer of processing from an IBM 7090 computer (a 36 bit-per-word machine) to an SDS 930 computer (a 24 bit-per-word machine) without the necessity for rewriting the data tapes

3. First-Pass Data Processing

In anticipation of a large quantity of data from OGO-III, the reduction/conversion program was conceived with the aim of maximizing the ease of data scanning For this reason, the final output medium chosen was 35 mm film in 100 foot rolls Figure 6 illustrates the sequence involved: the NASA data tapes are read into the digital computer and a reformatted data tape produced for off-line processing on the tape-to-film converter (TFC) The TFC uses the tape to produce images of the data on an oscilloscope and to control film exposures on an oscilloscope camera.

The data processing involved in the SDS 930 computer is essentially a three-stage process. In the first stage, data from one data sequence (i. e , one sequential reading of the main commutator channels) is checked to insure its quality and then placed in the proper frequency "pocket", analogous to the correlation technique used to construct Figure 5 Any redundant data are averaged, and the result placed in the appropriate pocket Unfilled pockets are then filled by

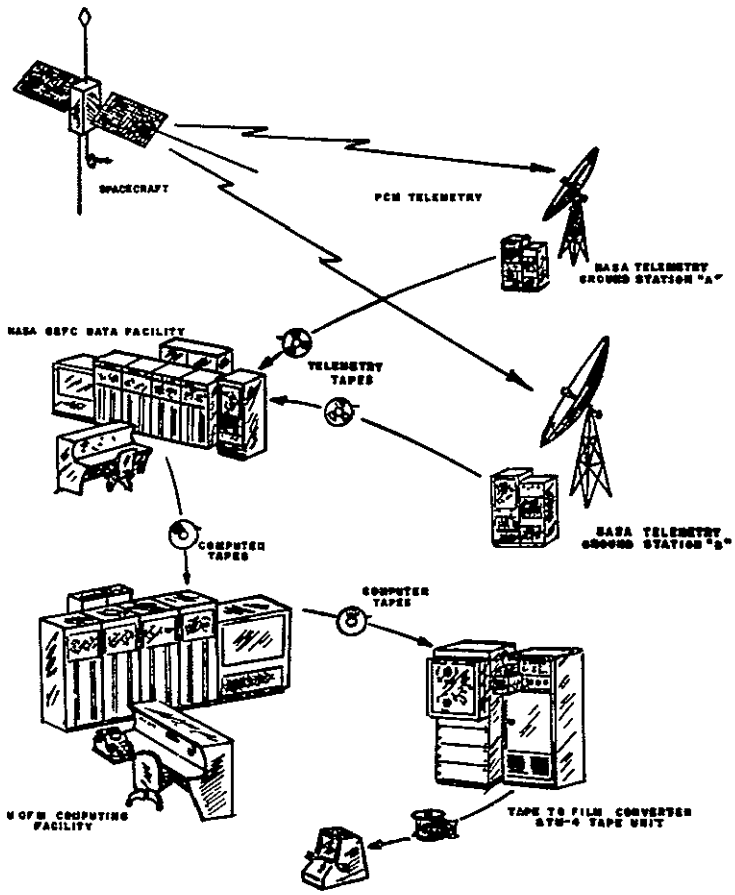

Figure 6. Orbiting Geophysical Observatory Data Flow
(UM/RAO Chart by D. R. McCreery)

interpolation Stage two of the program takes the "line" of filled frequency pockets and adds timing marks, bit error indicators and camera control codes. Stage three consists of writing the output tape with a specially formatted output from stage two, along with title frames generated from the data tape label records.

Analysis of the dynamic spectra produced by this procedure consists of visual scanning of the films with the aim of identifying the distinctive radiometer output resulting from solar radio bursts. The date and time of the burst are noted, the time being given to approximately ± 0.5 minutes, and a qualitative description of the type and intensity of the event is assigned. This information is used as a guide for the more detailed second-pass processing, which concentrates upon the significant events detected and briefly described by the preliminary data analysis.

5. Second-Pass Data Processing and Analysis

Second-pass data processing consists of taking the qualitative information provided by the preliminary analysis and using it as a guide to recover as much quantitative information as is available in the experimental data. Using the event times indicated by the initial data scan, a small amount of data is read from the data tape into computer storage. The radiometer voltages corresponding to several chosen frequencies are then plotted as functions of time, using the on-line CALCOMP plotter.

Two factors contribute to the possibility of an individual frequency pocket containing data which do not represent the true flux density of radiation on the antenna as a function of time and reception frequency The first factor is the inability of the experiment to provide coverage of more than a few frequencies in a short period of time To retain time resolution, unfilled frequency pockets are filled by interpolation from nearby filled pockets This is satisfactory only if pockets near the frequency in question contain good data. The second factor is the frequent occurrence of "data dropout" due to imperfect telemetry which results in either bad data or no data at all for these points.

To minimize the statistical effects of poor data and still retain the time resolution inherent in the experiment, the 100 frequency pockets are combined by averaging into 20 frequency pockets prior to interpolation The second-pass processing thus reduces experimental resolution in frequency to 100 kHz, while retaining time resolution of one to three seconds, depending on the data rate.

From the plotted output the following information about the solar burst event is recovered: flux density as a function of frequency, burst initiation time, drift rate and burst duration These items provide direct quantitative information concerning the energy dissipation of the low-frequency solar burst

E. Spacecraft and Experiment Operation

1 The OGO-III Spacecraft

The spacecraft was satisfactorily launched on June 7, 1966 and functioned without any significant problems for 46 days after launch. At 1804 UT, July 23, 1966, a short circuit occurred in one of the amplifiers in the reaction wheel attitude control system (ACS), causing the solar array paddles to lock into place. This prevented the spacecraft from maintaining solar pointing, which resulted in a decrease in the power output from the solar cells and curtailment of the operation of some of the experiment and housekeeping functions aboard the spacecraft.

The OGO-III spacecraft retained some reorientation capability due to the continued availability of the supplementary gas jet ACS. Using this capability, the mission control center placed the spacecraft in a controlled spin about the Z axis of the vehicle (mutually perpendicular to the line connecting the solar paddles and the line parallel to the length dimension of the spacecraft). This enabled the solar paddles to view the sun during a portion of the spin and to provide enough power for quasi-normal operation of the scientific experiments. As the earth-sun vector changed during the passage of time, successive reorientations became necessary in order to maintain an adequate power supply. These were accomplished by repeated use of the gas jets, together with the utilization of knowledge of the precession introduced into the spacecraft orientation during re-spin operations. Such

reorientations have been necessary at about three-month intervals since the ACS failure.

The effects of a spinning spacecraft may complicate the data analysis which has been discussed previously. This is due chiefly to the directional response pattern of the antenna. A point source which lies end-on to a dipole antenna will not produce an output at the antenna terminals. Therefore, if the sun is nominally in the plane of spin of the spacecraft, the response of the detection system will be influenced by such factors as the spin rate and the exact antenna pattern. In the actual case of OGO-III, the solar paddles happened to lock into position in such an orientation that the solar cell surface was approximately in the spacecraft spin plane. Subsequent reorientations were designed, therefore, to place the spacecraft in an orientation in which the sun-spacecraft line was approximately parallel to the spin axis. The sun was thus well within the antenna pattern of the radio astronomy experiment Except for brief periods prior to reorientation maneuvers, this positioning has been maintained The effects of the spacecraft spin have thus rarely been detectable on the radio astronomy data

The loss of positive spacecraft pointing had one significant consequence for the radio astronomy experiment The highly directional data transmission antenna was originally earth-oriented, and allowed data at high data rates to be transmitted from most segments of the orbit. With the loss of earth-pointing, transmission began to be made exclusively by the less efficient omnidirectional telemetry

antenna The effect was to reduce the percentage of high-data-rate data, transmission of which became possible only near perigee.

2. The Radio Astronomy Experiment

The equipment package for this experiment was designed to operate over a dynamic range of 65 db, producing an output signal ranging from zero to five volts The first limitation on the experiment was anticipated by pre-launch tests and confirmed shortly after launch, when it was found that the output noise level coming from the spacecraft environment of the package was nearly three volts. The dynamic range of the experiment was thus cut approximately in half, thereby decreasing the detection possibility for low intensity events.

A second limitation on the experimental data is the method of repeating the sweep through the frequency range. The spacecraft clock furnishes pulses every second to the experiment, which was designed to begin a new sweep after receiving two timing pulses. Forty-five days after launch, however, the spacecraft power supply began to develop transient pulses which were interpreted by the experiment as timing pulses. Since these pulses were frequent, they often arrived just after the first timing pulse, causing the radiometer to return to 4 MHz reception after only one second of sweep operation rather than the two second sweep operation designed. The result is a series of frequency sweeps from 4 MHz to 3 MHz with repetition time of one second, rather than two second sweeps from 4 MHz to 2 MHz.

Time resolution is thus increased by a factor of two, while the frequency band is decreased by the same amount

The reduced sweep problem was first noted at 1700 UT on July 22, 1966. It is worth noting that this is one day prior to the failure of the ACS; the two malfunctions are apparently not directly connected From the time of first incidence, the percentage of data containing only the 4-3 MHz band increased steadily; by October 10, 1966 the radiometer was operating entirely in the one-second sweep mode. This obviously decreased the information available for measurement of impulse drift rates At the same time, it permitted increased accuracy for measurements of burst initiation times and burst durations.

CHAPTER III

OBSERVATIONS OF SOLAR RADIO BURSTS

A Data Characteristics

1. Time Coverage

Over the time covered by this study, the radio astronomy experiment was in operation and in one of the three data rate modes for 90 8% of the possible hours of operation (see Table 2). Time gaps in the data do not follow a set pattern, but they are more likely to occur near perigee when the spacecraft is subject to occultation by the earth, as seen from the ground stations.

2 Detectability Limits

It has been stated in the previous chapter that the flux density detection limit for the OGO-III equipment in its operational configuration is approximately 3×10^{-19} watt $m^{-2} Hz^{-1}$. This high threshold indicates that only the more intense solar radio bursts will be detected. Therefore, it must be remembered that these bursts specify coronal conditions which are probably significantly different from those of the quiescent state.

In connection with this detection limitation, it is interesting to note that, in general, the strength of a burst bears no relationship to its other characteristics. That is, a strong burst is likely to have

Month	Hours in Month	Hours of OGO-III Operation	Fraction of Operation
June, 1966	425[1]	422	0.99
July	744	577	0.78
August	744	528	0 71
September	720	720	1.00
October	744	742	1.00
November	720	720	1.00
December	744	688	0.93
January, 1967	744	678	0.91
February	672	604	0.90
March	744	735	0.99
April	720	715	0.99
May	744	674	0.90
June	720	674	0.94
July	744	697	0.94
August	744	683	0 92
September	720	474	0.66
TOTALS	11393	10331	0 91

Table 2 Monthly Hours of Operation of the OGO-III Spacecraft

[1] From time of antenna deployment

the same duration, drift rate and spectral energy gradient as a weak burst. The major exception to this tendency appears to be that strong bursts are more likely to show clustering than are weak bursts (Maxwell, et al., 1960). For the purpose of this discussion it will be assumed that the drift rate of the burst and the form of the burst profile apply also to weaker bursts at low frequencies, although these have not been studied by the author.

The distribution of bursts as a function of relative energy output can be regarded as representative of the stronger bursts only. Finally, implications drawn from observations concerning the state of the corona are regarded as significant only in describing a corona in a highly disturbed state

3. Data Quality

When the spacecraft is near perigee, ionospheric noise over the receiver band is detected for a period of up to two hours before and after the time of perigee passage During this period only the strongest solar bursts are detectable on the data records The effect decreases rapidly as the height of perigee increases, and is of consequence in the case of OGO-III only for about six months after launch, as a result of the gradual decrease in the eccentricity of the spacecraft orbit. Table 3 shows that the number of bursts observed by the spacecraft varies directly with the amount of time spent in each radial distance range The implication is that ionospheric noise has essentially no effect on burst detection statistics; if it had, the detection

data would show a bias toward occurrence at large radial spacecraft distances.

Use of the spacecraft omnidirectional telemetry antenna in place of the high gain telemetry antenna results in considerable amounts of "bad data" These are data in which missing or incorrectly received telemetry bits distort the appearance of the experimental data to such an extent that recognition of solar events is seriously impaired Experience has shown that strong events can be detected even on distorted records, but that events of lower intensity are lost in the telemetry noise

To determine the amount of burst information lost, six data samples of 200 hours each were selected from various time periods of the sixteen months under study. The data were divided into "good" and "bad" The criterion for "good" data was that Importance 1 [2] bursts should be unambiguously visible. Importance 2 and 3 events were visible on nearly all records; the amount of data so severely distorted that a major event was undetectable was less than five percent. The percentage of good data under this standard averaged 33% and was essentially constant as a function of time The conclusion reached is that coverage of bursts with flux density $> 4\ 4 \times 10^{-17}$ watt $m^{-2}Hz^{-1}$ (the Importance 2 mean level) is 91% complete and is

---

[2] Importance ratings are qualitative estimates of the intensities of solar radio burst on the photographic data records. Table 6 gives the corresponding quantitative flux density limits.

Spacecraft Distance	No. of OGO-III Events Detected	Percentage of Events	Percentage of Time in This Part of Orbit
0 - 1 x 10^4 km	3	1.5	2.0
1 - 2	4	2.0	2.3
2 - 3	6	2.9	2.8
3 - 4	3	1.5	3.1
4 - 5	16	7.7	3.5
5 - 6	7	3.4	4.1
6 - 7	8	3.9	5.0
7 - 8	11	5 3	6.2
8 - 9	18	8.7	7.2
9 - 10	13	6.3	8.1
10 - 11	25	12 0	10 3
11 - 12	32	15.4	14.5
> 12	62	29.9	30 9

Table 3. Solar Burst Detection as a Function of Spacecraft Distance.[3]

limited only by the spacecraft time coverage. For bursts with 4 4 x 10^{-17} watt $m^{-2}Hz^{-1}$ > S_ν > 3 x 10^{-19} watt $m^{-2}Hz^{-1}$ the coverage is estimated to be (91%) (33%) = 30% complete

[3] No orbit information is available for the spacecraft at the times of ten of the solar radio bursts

4. Effective Time and Frequency Resolution

The time resolution limit for the OGO-III experiment is set by the telemetry rate and, as discussed in the instrumentation section of this paper, by the location of the data words assigned to the experiment on the spacecraft main commutator frame. The long time scale of low-frequency solar bursts and their wide bandwidths, compared to the time constants and instantaneous bandwidth of the equipment, permit some averaging of data in both frequency and time without a significant loss of information. Such averaging tends to smooth anomalous data bits due to poor data transmission, radio frequency interference, etc.

In this analysis time and frequency resolution limits are set by the method of data treatment in the second-pass program In this program the outputs from the radiometer are analyzed for twenty frequency intervals, each having a bandwidth of 100 kHz. The radiometer output voltage of any one of these intervals is then plotted as a function of time For 1 kb data, the voltages from three scans are averaged, and the time resolution is 3(1 152 sec) = 3 456 sec. Fourteen scans are averaged for 8 kb data and one hundred twelve for 64 kb data; the time resolution is 8(0 144 sec) = 2.016 sec and 112(0.018 sec) = 2.016 sec, respectively. These limits are well below the anticipated burst bandwidths of several MHz and burst durations of several minutes

B The Fast Drift Burst at Low Frequencies

1 Frequency of Occurrence

Analysis of the sixteen months of OGO-III data has resulted in detection of 218 solar radio bursts, or about one burst for each 50 hours of operation The number of bursts in each month is given in Table 4

2. Spectral Appearance of the Events

The appearance of fast drift solar spectral events at low frequencies is similar to that seen in higher-frequency observations. In the standard format, frequency is plotted vertically and increases from top to bottom and time is plotted horizontally, increasing from left to right. Figure 7 illustrates the format, in this case for data containing a powerful solar burst The time scale along the horizontal axis is in minutes, the space between each tick mark representing a one-minute interval This positive print shows enhancement as a function of increased signal to the radiometer The increased signal from about 2 to 2. 3 MHz is ambient radio frequency interference from the spacecraft The solar burst is double, presumably indicating two separate excitations of the coronal region producing the radiation. The data during this time period were taken at the 8 kb rate; because of the averaging of redundant data the appearance of 64 kb data is similar to the 8 kb data

At the 1 kb data rate the appearance of bursts on the spectral records undergoes time compression, as seen in Figure 8. On these

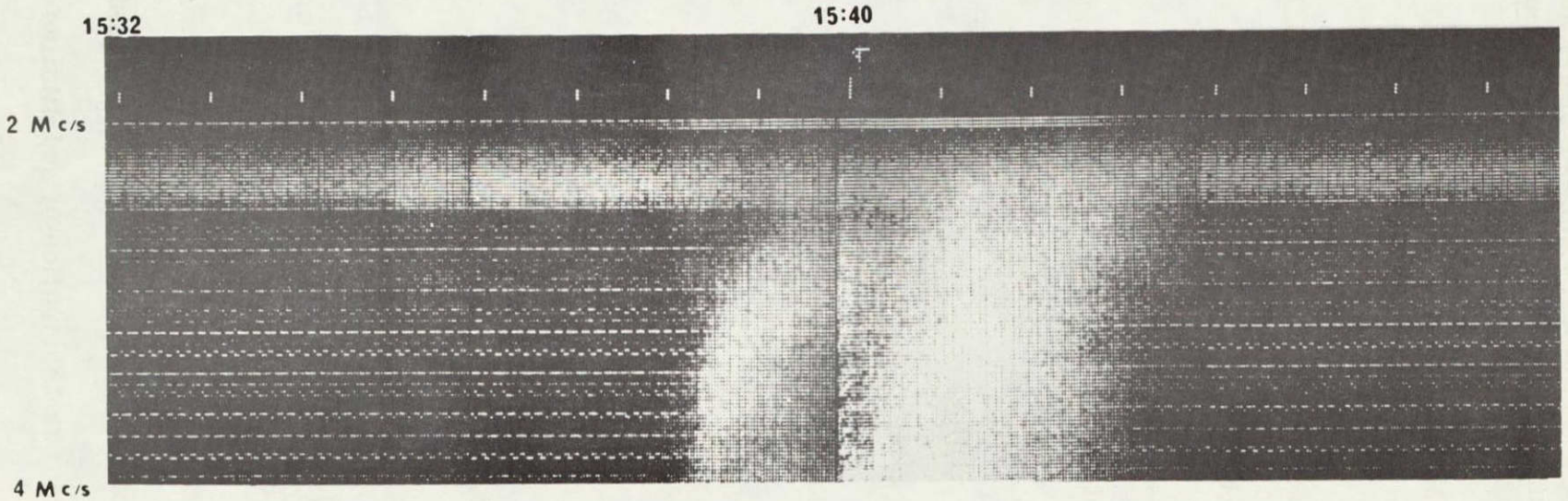

Figure 7. Dynamic Spectrogram of a Low-Frequency Solar Radio Burst. (UM/RAO Chart)

Month	Number of 4-2 MHz Solar Burst Events
June, 1966	12
July	7
August	3
September	13
October	8
November	4
December	11
January, 1967	4
February	13
March	39
April	12
May	7
June	16
July	50
August	15
September	4
	218

Table 4. Monthly Summary of Solar Burst Events Detected by OGO-III.

records the drift of the burst onset from higher to lower frequencies can be seen only with difficulty. Second-pass processing is thus absolutely necessary for the derivation of quantitative values from low data rate information.

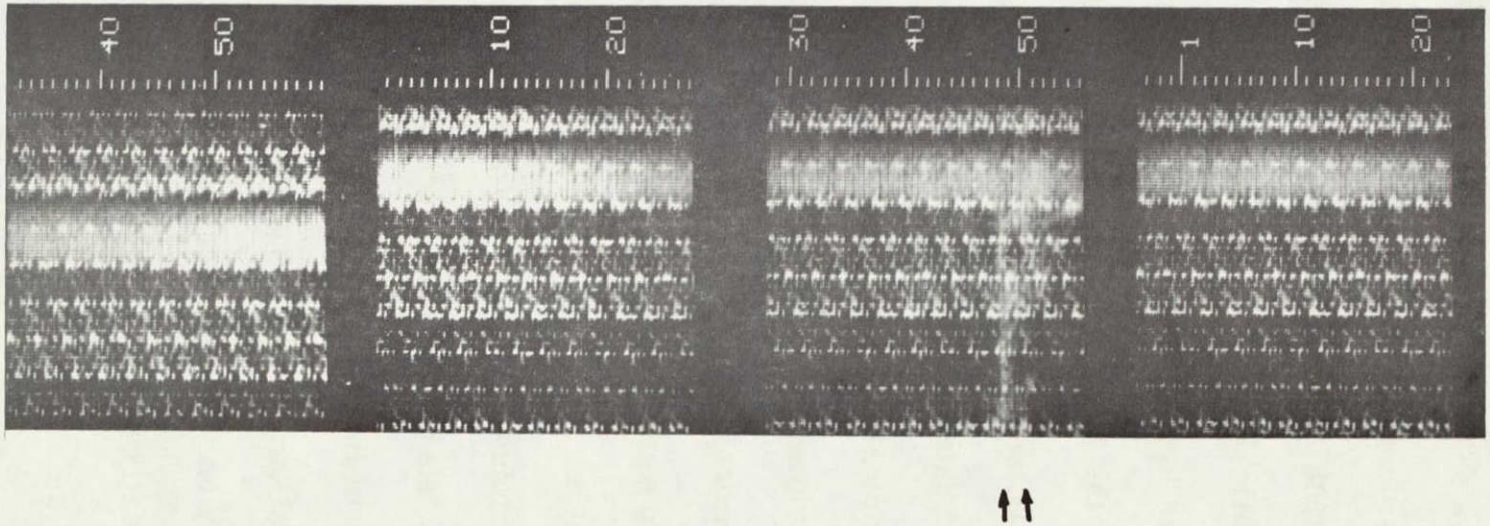

Figure 8. A Series of Solar Bursts at 1 kb Data Rate.

As has been discussed previously, the OGO-III radiometer shifted from a 4-2 MHz sweeping mode into a 4-3 MHz sweeping mode after several months of operation, due to transient pulses in the spacecraft clock. The resulting dynamic spectrograms contain two virtually identical 4-3 MHz bands, since the data time separation between bands is only one second. An example of the appearance of these data at the 1 kb rate is seen in Figure 9.

Finally, Figure 10 illustrates the appearance of strong solar bursts on bad data records. On this 1 kb data segment, the markings in the time indication portion of the record signal the absence of complete data coverage (presumably due to insufficient power radiation by the omnidirectional telemetry antenna; the spacecraft was within 1500 km of apogee). It is clear from this figure that a powerful event has taken place. It is equally clear that the characteristics of the event are completely obscured by the very high noise to signal ratio. Detailed analysis of the noise level shows that it is above the output level of most of the weak bursts detected on other data records.

Second-pass processing involves scanning the original data at one frequency only, and plotting the output voltage as a function of time on a greatly expanded time scale using the SDS 930 computer interfaced to a Calcomp 565 plotter. The result permits much more accurate quantitative measurement of parameters than can be made from the photographic method of display. An example of the plots produced by this method is shown in Figure 11.

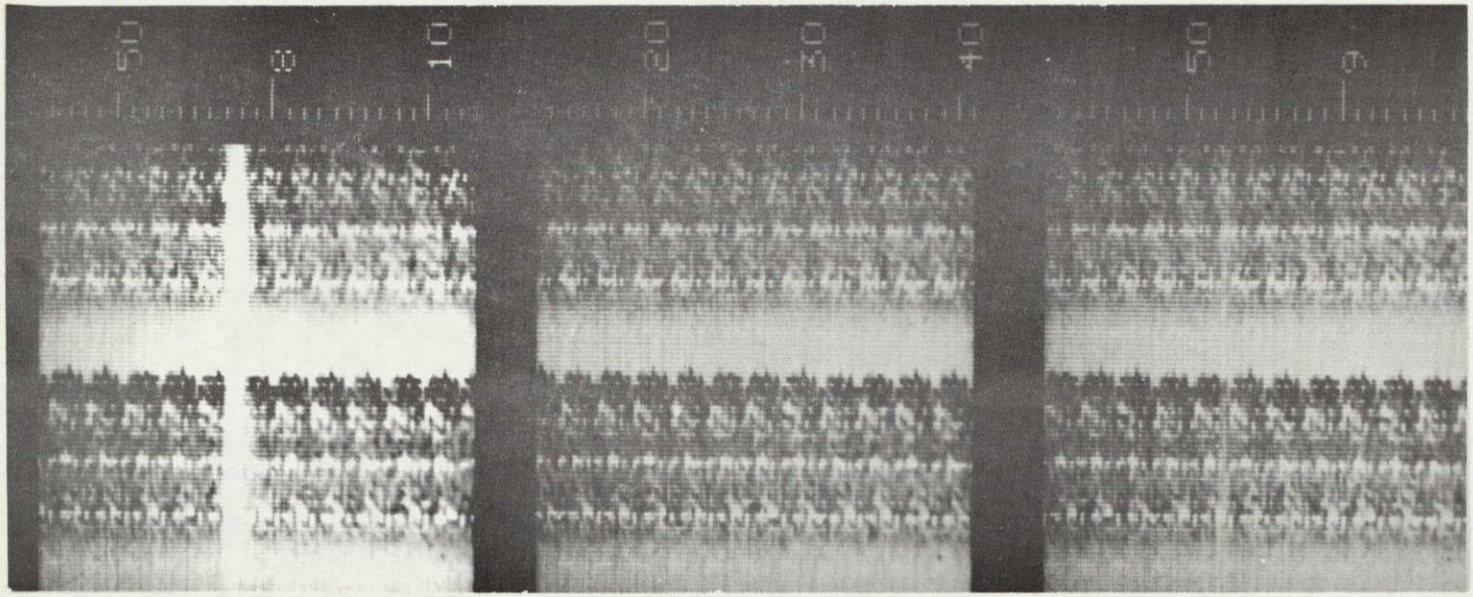

Figure 9. A Solar Burst with 4-3 MHz Band Redundancy.

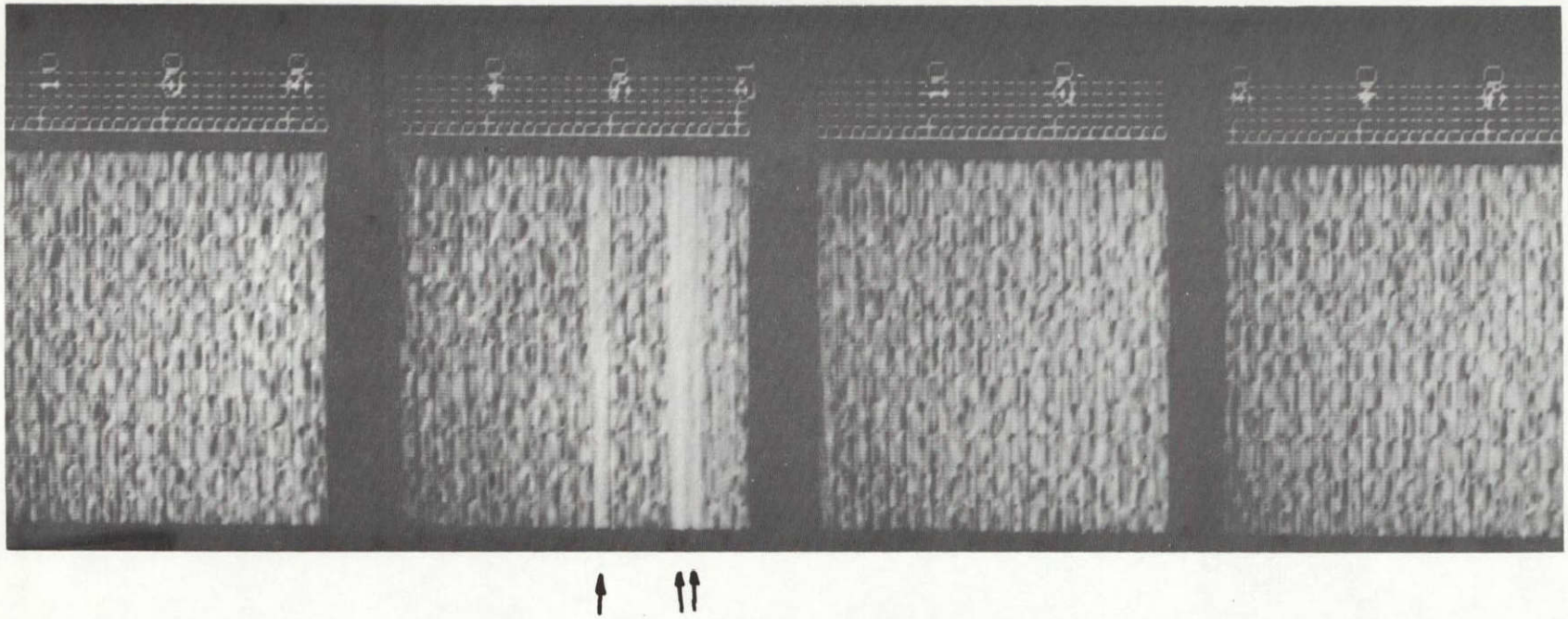

Figure 10. The Appearance of Strong Solar Radio Bursts on Bad Data Records.

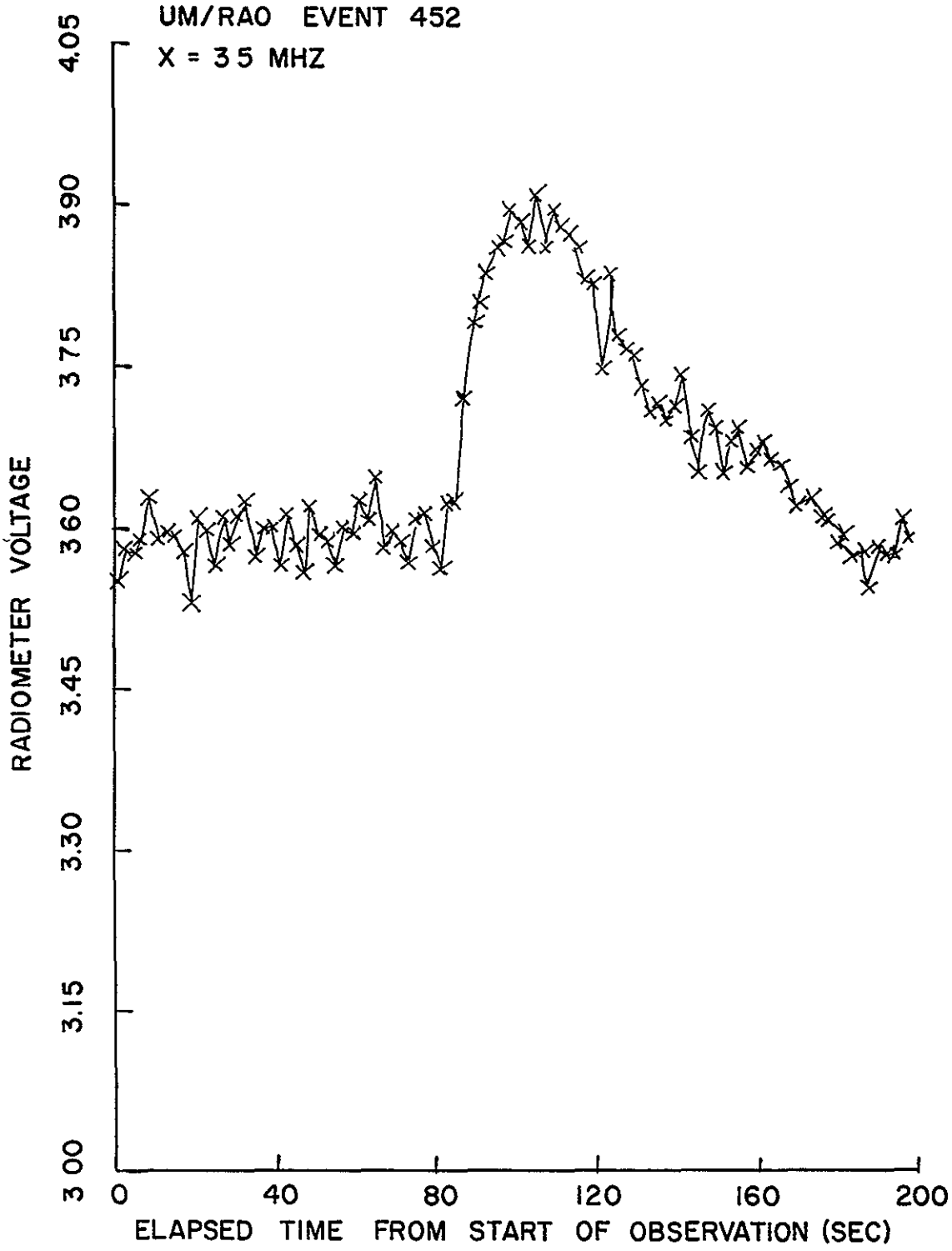

Figure 11. A Monofrequency Burst Profile Produced by Second-Pass Data Processing Techniques.

3. Drift Rates

To determine the rate of drift of the burst impulse across the 4-2 MHz frequency band, 42 burst events were investigated in detail using second-pass processing. By making a series of single-frequency plots for each event, the increase in the signal as a function of time can be followed through the OGO-III radiometer pass band. Seven of the 42 burst events investigated were multiple in nature, permitting two drift rates to be unambiguously derived Thus 49 sets of single-frequency plots are available for analysis.

The accuracy of the derived drift rates is not the same for all events, since more accurate results are obtainable for events which were observed at high telemetry rates, preferably at times of low interference To an extent, the accuracy is a function also of the signal-to-noise ratio of the burst, since a strong signal enables more precise measurement of starting times for the burst under study. Finally the profile of the burst affects the results to some degree, as a sharp rise to maximum is more easily measured than a gradual rise of the same magnitude

All drift rates were measured from the initiation time of the burst rather than from the time of maximum. The former is much easier to define on the data plots, and the flat response of the radiometer over the reception band prevents distortion of the drift rates due to the response curve

The average value for all drift rate measurements is 0.095 ± 0.010 MHz/sec; at this rate it would take 21 seconds for a burst impulse to drift across the OGO-III band from 4-2 MHz.

4. Duration of Bursts

Two distinct methods can be used to measure the durations of solar radio bursts If a very accurate instrumental calibration is available, the e-folding time of the burst can be measured Alternatively, the complete detected extent of the burst can be measured. In the second method, the assumption is made that for a high noise-to-signal ratio the e-folding level is not seen, and the measured duration is thus a lower limit to the duration Because of the calibration accuracy which has been obtained, the first method is used here

Duration measurements were made for each of the 49 burst events studied in the drift rate analysis A study of the data suggests that the 3 5 MHz durations are the least distorted by spacecraft interference; for that reason they have been subjected to a more intensive analysis and correlation than durations derived for other OGO-III frequencies

The mean values of burst duration from the time of burst maximum until decline to $\frac{1}{e}$ of the maximum level as a function of frequency are given in Table 5 The number of measurements differs with frequency as noted The small number of measurements below

3 MHz is due to the instrumental mode change early in the life of the spacecraft

Frequency	Number of Measurements	Mean Duration
4.0 MHz	42	20.9 ± 1 7 seconds
3 5	49	23.3 ± 1 4
3.0	33	21 1 ± 1 6
2 5	6	23.0 ± 2 1
2 0	4	25 6 ± 2 3

Table 5 Burst Duration as a Function of Frequency

5. Burst Harmonics

Harmonics may be expected to be seen in either of two ways on the OGO-III data. If the exciting mechanism produces measurable radiation at all frequencies in the 4-1 MHz range, both fundamental and second harmonics should be detected in the OGO-III reception band. Secondly, second harmonics of the 2-1 MHz band which are produced under conditions in which the primary radiation is absorbed will appear on the OGO-III records as single bursts, but with the characteristic drift rates and burst durations of the 2-1 MHz region from which the radiation originates

The characteristics of data in which both fundamental and second harmonic radiation are detected in the 4-2 MHz band can be

predicted through the use of the burst harmonics model developed in Chapter IV The values for the second harmonic of the 2-1 MHz emission have been derived using the Malitson-Erickson (1966) coronal density model. The results are that, in the 4-2 MHz band, the time lag between fundamental and second harmonic radiation at the same frequency should be of the order of 20 seconds, and the drift rate of the second harmonic radiation should be of the order of 0 04 MHz/sec Since typical 1/e burst durations in the OGO-III band are equal to or greater than the predicted time lag, the second harmonic must be of the same order of magnitude in terms of flux density level in order to be detected Only one fundamental-harmonic pair has been detected with certainty in the OGO-III data The burst profiles of this event at 0 5 MHz intervals are shown in Figure 12. Although the data sample is limited, such burst pairing does not appear to be common at 4-2 MHz.

In the data sample for which studies of burst durations and drift rates were possible, no evidence was found to indicate the presence of second harmonic bursts without their associated fundamentals being present

6 Energy Spectra

Detailed processing of data for 42 solar radio burst events provided flux density data for 61 individual bursts. The additional 19 data points resulted from burst clustering within the events The characteristics of low-frequency bursts are most distinct in or near

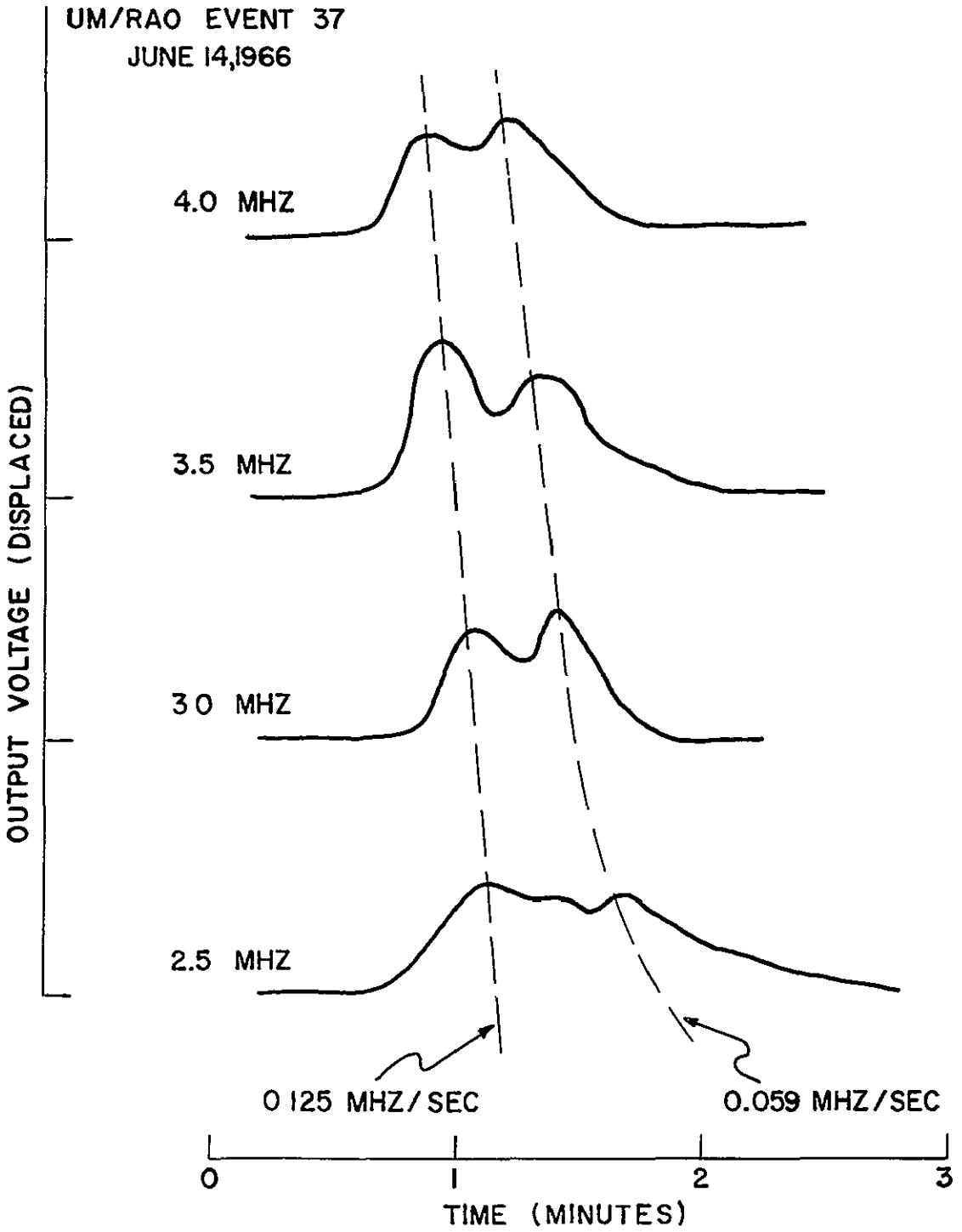

Figure 12. Low-Frequency Profiles of a Harmonic Burst

the center of the frequency band, as opposed to those precisely at the beginning or end of the frequency sweep For this reason the flux density results at 3 5 MHz have been studied in some detail These provide data both prior to and subsequent to the changeover from two to one second sweeping. The average maximum flux density and the range in maximum flux density as a function of,OGO-III burst importance is given in Table 6.[4]

OGO-III Burst Importance	Number of Events	Mean Flux Density (10^{-17} watt $m^{-2} Hz^{-1}$)	Range of Flux Density (10^{-17} watt $m^{-2} Hz^{-1}$)
4	4	74	13 to 110
3	20	16	1.8 to 63
2	26	4.4	1.6 to 23
1	11	2.8	1 0 to 6 1

Table 6 Flux Density as a Function of Burst Importance at 3. 5 MHz.

The results indicate that, in general, the qualitative ratings give an accurate picture of the relative burst importance at low frequencies. Extreme values in any one importance designation are due in most cases to bursts within a cluster of several closely-spaced bursts The relative importance of such bursts with respect to each other is extremely difficult to specify.

---

[4] Individual values for selected events are given in Appendix II.

Measurement of the area under the calibrated solar burst profile curve gives the total energy output of the burst per Hz The average value for all bursts studied is 1 87 x 10^{-15} joules m^{-2} Hz^{-1} [5] If it is assumed that the solar burst radiates into a hemisphere and that the flux density spectrum is flat over the OGO-III reception band (which is suggested by unpublished data from the Michigan experiment aboard OGO-V), the average electromagnetic energy loss in the 4-2 MHz passband is

$$E_{Total} = (E_{4\text{-}2\ MHz},\ joule\ m^{-2}\ Hz^{-1})\ (A_{Hem}\ ,\ m^2)\ (\Delta B_{OGO\text{-}III},\ Hz)$$

$$= (1\ 87 \times 10^{-15})\ (1\ 41 \times 10^{23})\ (2 \times 10^{6})$$

$$= 5\ 28 \times 10^{14}\ joules$$

This figure is the energy equivalent of 8 2 x 10^{31} 40-keV electrons The estimates of Van Allen and Krimigis (1965) of the number of fast electrons escaping from the sun and of the number required to produce an X-ray event indicate that this 4-2 MHz electromagnetic energy loss is approximately equivalent to the average escaped electron energy loss and that these energy losses comprise 0.01 to 0 1 of the total energy involved in a major X-ray event

---

[5] Individual values are listed in Appendix II

7. Clustering of Low-Frequency Bursts

The tendency for fast drift solar radio bursts at meter wavelengths to occur in groups of from two to ten within a few seconds is well known and well observed. Such bursts are distinguished from harmonic bursts by their similar properties; their drift rates, durations, and in many cases their intensities are so similar as to be indistinguishable. This clustering characteristic is present also on OGO-III low-frequency records. An example is shown in Figure 13. The bursts occur with a sixty-second separation at the start of the record. A change in synchronization occurs immediately following the bursts due to a spurious timing pulse received by the radiometer. The drift rates and burst durations derived from Calcomp plots agree closely. In all, 21 burst events observed by OGO-III can be readily identified as clustered bursts; this is about 9% of all bursts observed. The figure could well be much higher if greater time resolution were available, since most of the burst events plotted suggested the presence of more than one peak in the intensity profile.

An analysis of the qualitative importance rating of the clustered events confirms, for low frequencies, the finding that the stronger burst events tend to be clustered more often than do the weaker events. The mean importance rating for OGO-III clustered bursts events is 2.65 compared with 1.89 for all OGO-III events.

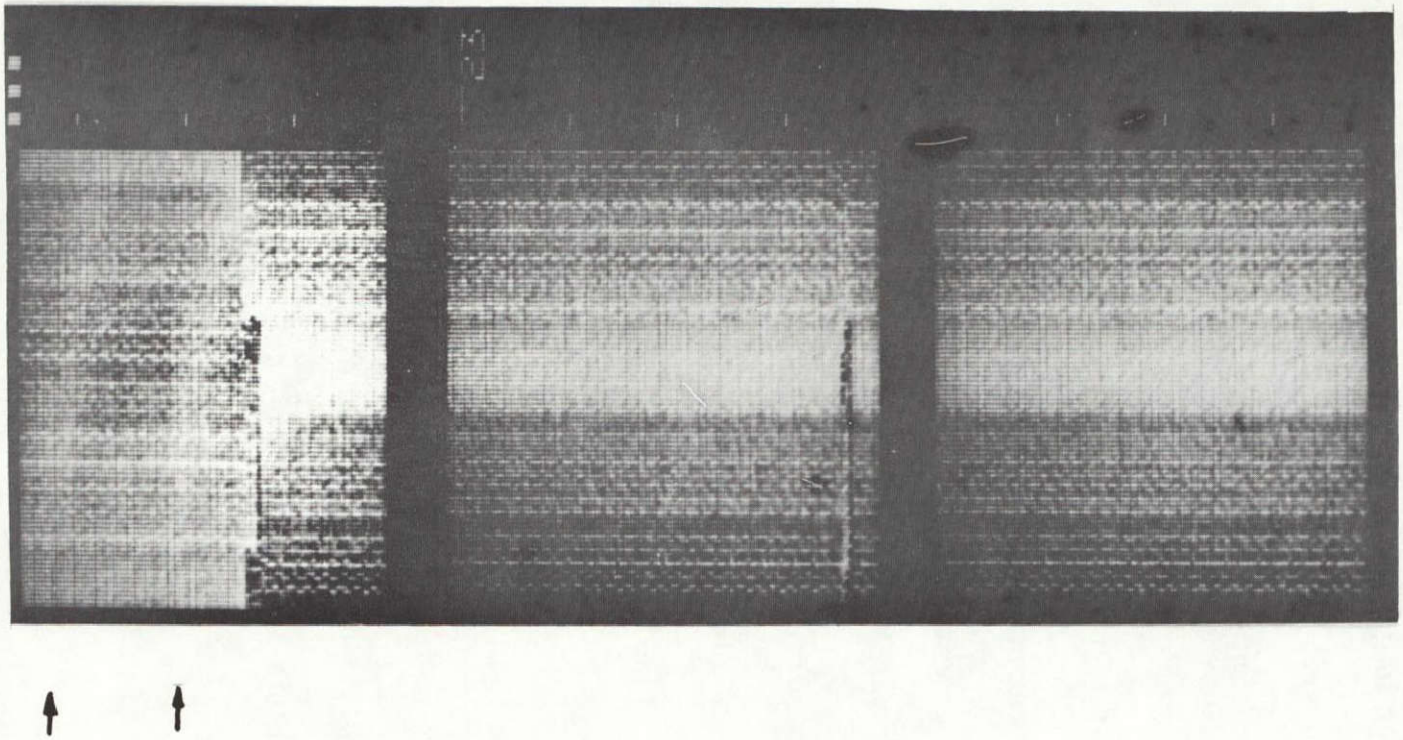

Figure 13. Low-Frequency Clustered Solar Radio Bursts.

8. Associated Type V Bursts

If Type V radiation is to be visible on low-frequency records, it must be strong enough to be distinguished at the threshold level of the instrument, and it must last significantly longer than the associated fast drift burst. At ground-based frequencies the duration of Type V radiation is typically one to two minutes (Warwick, 1967), which is of the same order of magnitude as fast drift burst durations at low frequencies.

Despite the difficulties implied by the factors mentioned above, it has been possible to detect low-frequency Type V radiation for a limited number of events. Perhaps the most graphic of these is shown in Figure 8; here the duration of the Type V radiation increases toward lower frequencies and appears to be about six minutes at 2.5 MHz. Another example is shown in Figure 14. The radiometer was operating in the one-second sweep mode during this event. The burst duration is of the order of four minutes and appears to decrease with frequency. Only two other events have unambiguous Type V radiation following the fast drift burst. For the four events the mean duration of the Type V radiation is approximately five minutes.

For many of the clustered bursts observed by OGO-III it is a moot point as to whether Type V radiation is present or not. For such events a series of bursts of weak intensity may easily be mistaken for broadband continuum. An example of such an event is that shown in Figure 10. Even when plotted with high time resolution it

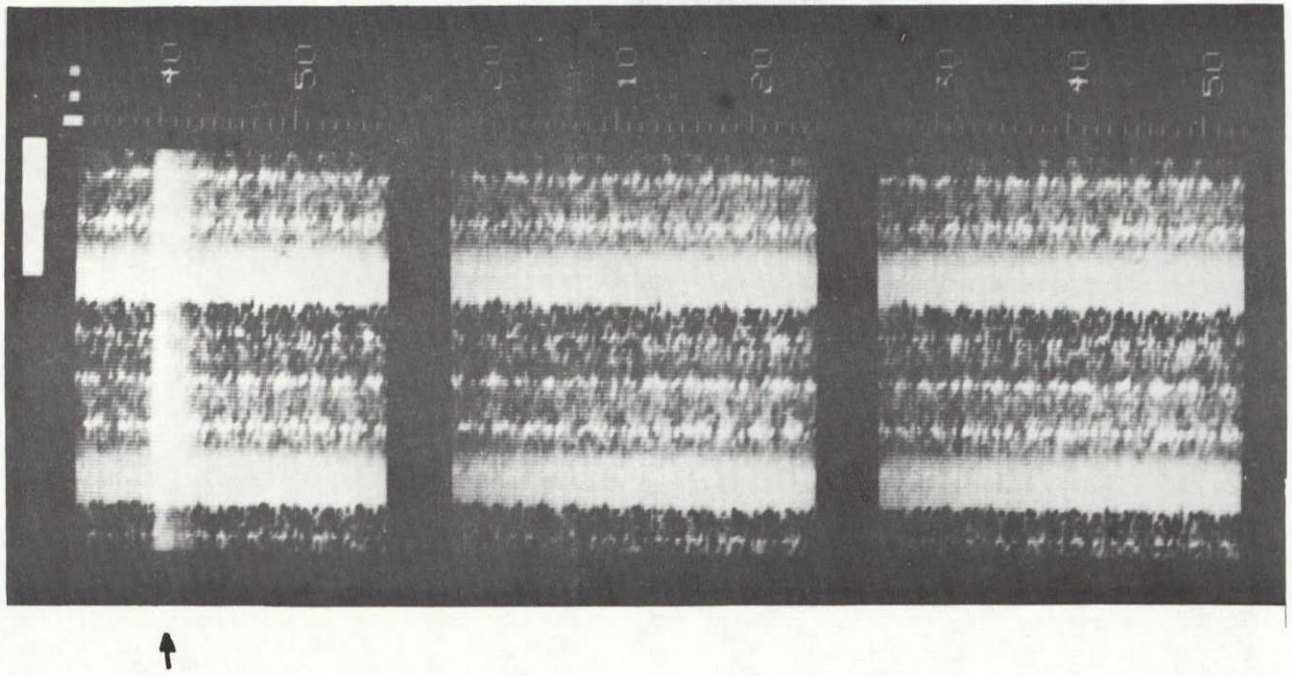

Figure 14. The Appearance of Type V Radiation on Low-Frequency Data Records.

is impossible to specify the characteristics of the enhancement following the fast drift event

The conclusion drawn from the above is that Type V radiation has been unambiguously detected at low frequencies, but not in sufficient quantity to specify its characteristics It is worth noting that the percentage of definitely identified Type III/V burst events is 4/218 = 1.8%. This is close to the 2% figure given by Thompson and Maxwell (1962) for higher-frequency observations.

9 Monofrequency Burst Profiles

A great deal of information can be obtained from analyses of solar radio burst profiles. The method of profile measurement used is illustrated in Figure 15. The burst duration at a designated level with respect to peak flux density is given by B, while burst duration with respect to the base level is given by D. The durations from peak flux density to the point of burst termination for the reference levels are specified by A and C. The total shape of the curve may be specified by measuring A and B for several different levels with respect to the peak flux density

The relationship between the rise time and decay time of the bursts may be specified by the ratios A/B and C/D. The determination of the levels with respect to the peak flux density depends directly on the calibration. The A/B ratio is thus calibration-dependent. The C/D ratio, conversely, is independent of the calibration but might not

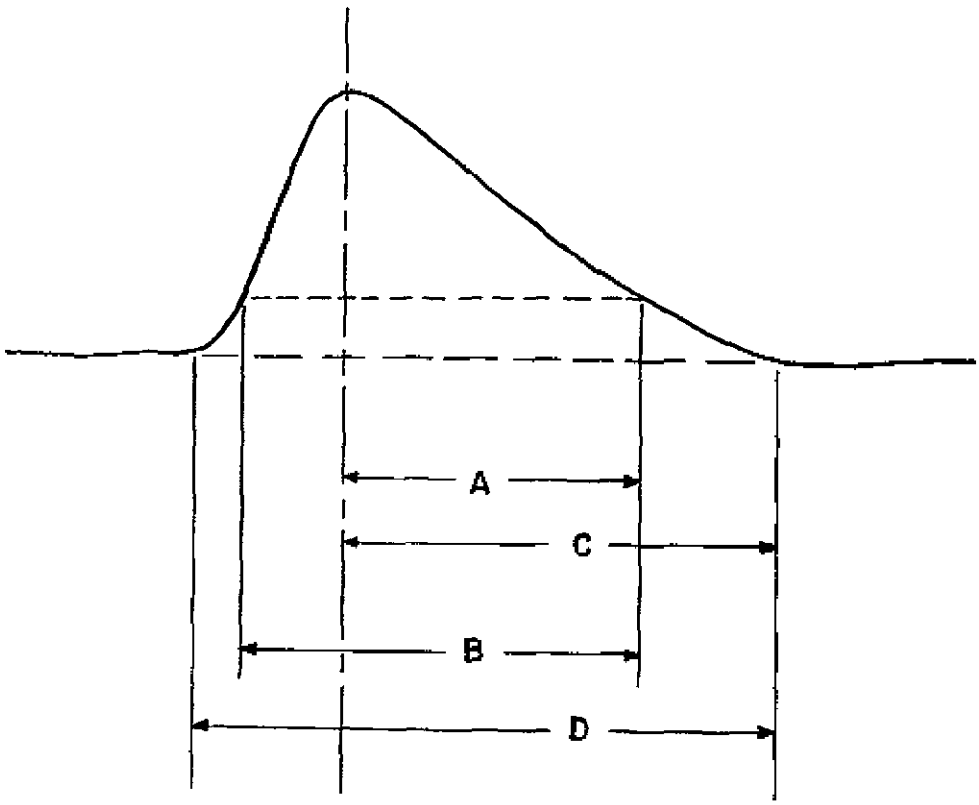

Figure 15 Definition of Measured Burst Profile Parameters

be an accurate reflection of the burst profile. A profile in which both the rise and fall slopes are essentially constant, however, should give the same value for each ratio. Table 7 lists the measured values at 3.5 MHz for the bursts on which detailed measurements are possible for measurements at the 0.9, 0.8, 0.6 and 1/e levels. The average values for the ratios are nearly the same: $(A/B)_{\frac{1}{e}\,ave} = 0.64$, $(C/D)_{ave} = 0.62$.

Although there is a moderate amount of variation among the burst profiles, it is accurate to say that the idealized profile depicted in Figure 15 resembles closely the appearance of the great majority of low-frequency bursts which have been studied. In some instances, particularly when the peak flux density is very high, the leading slope of the profile is much more gradual, and the burst becomes nearly symmetric about its peak. Profiles for which the leading slope is markedly more gradual than the trailing slope have not been observed, nor have profiles which include a flat or nearly flat "plateau" at the peak flux density. In nearly every case the maximum is sharp and well-defined.

10. Reverse Drift Bursts

Reverse drift bursts are those in which the sense of the frequency drift is from lower to higher frequencies, rather than conversely. In the frequency range 500-7 MHz these are generally seen as a "turning-over" of a standard fast drift burst; the total event is called a "U-burst", after its appearance on solar spectral records

UM/RAO Event Number	$A_{0.9}$ (sec)	$B_{0.9}$ (sec)	$A_{0.8}$ (sec)	$B_{0.8}$ (sec)	$A_{0.6}$ (sec)	$B_{0.6}$ (sec)	$A_{1/e}$ (sec)	$B_{1/e}$ (sec)	$A/B_{1/e}$	C (sec)	D (sec)	C/D
2	2.2	3.0	2.7	4.0	6.4	11.4	9.5	16.5	0.58	30	54	0.56
4	2.2	4.4	5.0	9.1	10.1	16.5	14.5	23.0	0.63	23	37	0.62
37	6.1	10.0	8.0	12.5	12.9	20.1	18.9	28.1	0.68	35	55	0.64
59a	5.5	11.0	8.1	16.3	14.3	31.4	23.1	46.8	0.49	71	125	0.57
59b	8.1	16.2	17.5	29.5	29.1	44.8	43.0	65.1	0.66	91	124	0.73
66	5.0	10.1	8.5	17.1	12.3	23.5	15.4	27.9	0.56	44	68	0.65
80	6.5	9.5	11.5	15.5	18.5	23.0	28.0	33.1	0.85	27	83	0.33
104a	8.0	11.5	9.5	14.5	13.2	20.6	17.4	26.7	0.65	19	40	0.48
104b	8.3	13.2	12.5	18.5	20.5	30.1	32.1	45.0	0.71	32	120	0.27
155	4.4	10.9	6.0	14.5	9.5	20.9	16.2	30.4	0.53	x	x	x
159	6.1	13.0	8.5	17.5	11.5	23.5	17.2	33.1	0.52	47	80	0.59
160a	6.5	13.1	7.5	16.5	10.2	22.4	12.0	28.2	0.43	17	41	0.41

Table 7. Solar Burst Profile Parameters

UM/RAO Event Number	$A_{0.9}$ (sec)	$B_{0.9}$ (sec)	$A_{0.8}$ (sec)	$B_{0.8}$ (sec)	$A_{0.6}$ (sec)	$B_{0.6}$ (sec)	$A_{1/e}$ (sec)	$B_{1/e}$ (sec)	$A/B_{1/e}$	C (sec)	D (sec)	C/D
160b	8.2	14.3	11.2	19.2	13.5	23.9	15.7	27.8	0.57	27	45	0.51
209	4.5	10.0	9.1	19.1	13.1	27.2	18.5	37.8	0.49	35	68	0.51
217	4.1	9.3	6.0	13.5	8.9	19.5	17.1	31.2	0.55	27	50	0.54
328	3.1	5.0	4.2	6.5	6.5	10.5	8.0	14.1	0.57	x	x	x
329a	4.5	6.5	6.1	8.5	7.1	11.5	7.9	14.0	0.57	23	43	0.54
329b	11.5	23.8	18.5	37.5	31.0	61.0	64.0	105.0	0.61	x	x	x
452	6.5	10.2	10.9	16.1	16.9	25.3	28.9	41.2	0.71	x	x	x
454	5.0	7.5	7.3	11.2	12.5	19.5	16.4	25.6	0.64	62	83	0.75
461a	6.1	9.5	8.5	13.0	17.5	26.4	24.1	35.3	0.69	75	103	0.73
461b	4.9	8.1	7.5	11.9	16.5	25.5	16.4	25.2	0.64	54	72	0.75
474	6.5	9.5	7.5	12.1	10.9	16.5	17.0	27.8	0.71	x	x	x
477	9.2	16.5	12.9	24.3	19.1	37.0	27.9	51.1	0.55	x	x	x
479	29.1	40.5	40.5	55.0	53.2	71.4	65.0	88.0	0.74	116	173	0.67

Table 7 (Cont.)

UM/RAO Event Number	$A_{0.9}$ (sec)	$B_{0.9}$ (sec)	$A_{0.8}$ (sec)	$B_{0.8}$ (sec)	$A_{0.6}$ (sec)	$B_{0.6}$ (sec)	$A_{1/e}$ (sec)	$B_{1/e}$ (sec)	$A/B_{1/e}$	C (sec)	D (sec)	C/D
481	3.0	5.2	4.5	7.5	7.5	12.5	10 1	17 2	0.59	x	x	x
488	5.5	11.5	9.5	19.1	13.5	25.5	19.2	34.4	0.56	x	x	x
501	8.2	13.5	13.8	23.2	22.5	37.5	32.8	55.0	0.60	118	179	0.66
503	3.5	6.5	4.5	8.5	5.5	10.5	7 1	14.1	0.50	36	83	0.43
504	5.5	9.5	8.5	13 0	16 5	22.5	25.0	32.1	0 78	99	140	0.71
514	9 5	15 5	15.1	24 2	23.8	36 5	34 0	50.0	0.68	117	146	0 80
560	3.5	7 5	6.2	12 5	7.5	17.2	10 0	21 8	0.45	41	63	0 65
614	4 1	7.0	5 5	10.5	7.2	13.5	10.1	19.0	0 53	31	50	0 62
676	7 5	10 5	12 1	16.5	16 5	22 5	22.8	30.7	0.74	x	x	x
678	5.9	9.8	10 5	15 1	18 0	23 4	27,1	32.0	0.84	82	98	0 84
680	4 5	7.5	5 9	10.0	8.0	13 5	10 2	18 3	0 44	x	x	x
683	4 0	7.5	5.5	9 7	8 9	15 1	15.1	23.0	0 65	x	x	x
684	5 0	10 5	7.2	13 3	11 5	17.9	14 9	21 8	0.68	45	69	0.65

Table 7. (Cont.)

UM/RAO Event Number	$A_{0.9}$ (sec)	$B_{0.9}$ (sec)	$A_{0.8}$ (sec)	$B_{0.8}$ (sec)	$A_{0.6}$ (sec)	$B_{0.6}$ (sec)	$A_{1/e}$ (sec)	$B_{1/e}$ (sec)	$A/B_{1/e}$	C (sec)	D (sec)	C/D
686	3.5	7.0	6.0	11.0	10.5	16.5	17.0	25.0	0.68	103	103	0.76
687	5.1	7.5	7.2	10.5	14.5	20.5	29.0	38.5	0.76	115	157	0.73
692	4.4	7.6	6.0	10.5	11.0	18.5	20.0	30.0	0.67	x	x	x
695	5.2	8.5	5.8	10.2	10.2	16.8	13.2	23.3	0.57	52	76	0.68
1101	6.5	10.1	11.0	19.0	21.0	34.3	40.1	53.0	0.75	119	153	0.78
1151	5.4	8.2	8.1	12.8	9.5	21.1	14.2	29.5	0.48	x	x	x

Table 7. (Cont.)

One such reverse-drift burst has been observed by OGO-III. The event took place at 1525 - 1531 UT on September 19, 1966, and is illustrated in Figure 16. The detail of the burst which is visible on the original negative record is diagrammed below the illustration. The rate of drift of the reverse-drift burst is about half that of the preceding fast drift burst, and the intensity is much greater. A fast drift burst was seen at higher frequencies just preceding the OGO-III event illustrated, but no reverse-drift high-frequency event was detected.

C. The Slow Drift Burst at Low Frequencies

1 Anticipated Characteristics

The characteristics of Type II (slow drift) bursts at higher frequencies have been discussed by Wild, Smerd, and Weiss (1963), Kundu (1965), and others, and can be described concisely as follows:

The Type II bursts are much less frequent than fast drift bursts, occurring three or four times per month near sunspot maximum. Their energy spectrum is similar to that of fast drift bursts. The drift rate is very much slower, suggesting a velocity for the exciting mechanism of about 1000 km/sec. Type II bursts have been observed at frequencies as low as 5 MHz (Suzuki, Attwood, and Sheridan, 1964) Harmonic bursts are common, and are easily distinguished due to the slow drift rates involved. At 4-2 MHz the expected energy from Type II bursts is comparable with that of fast

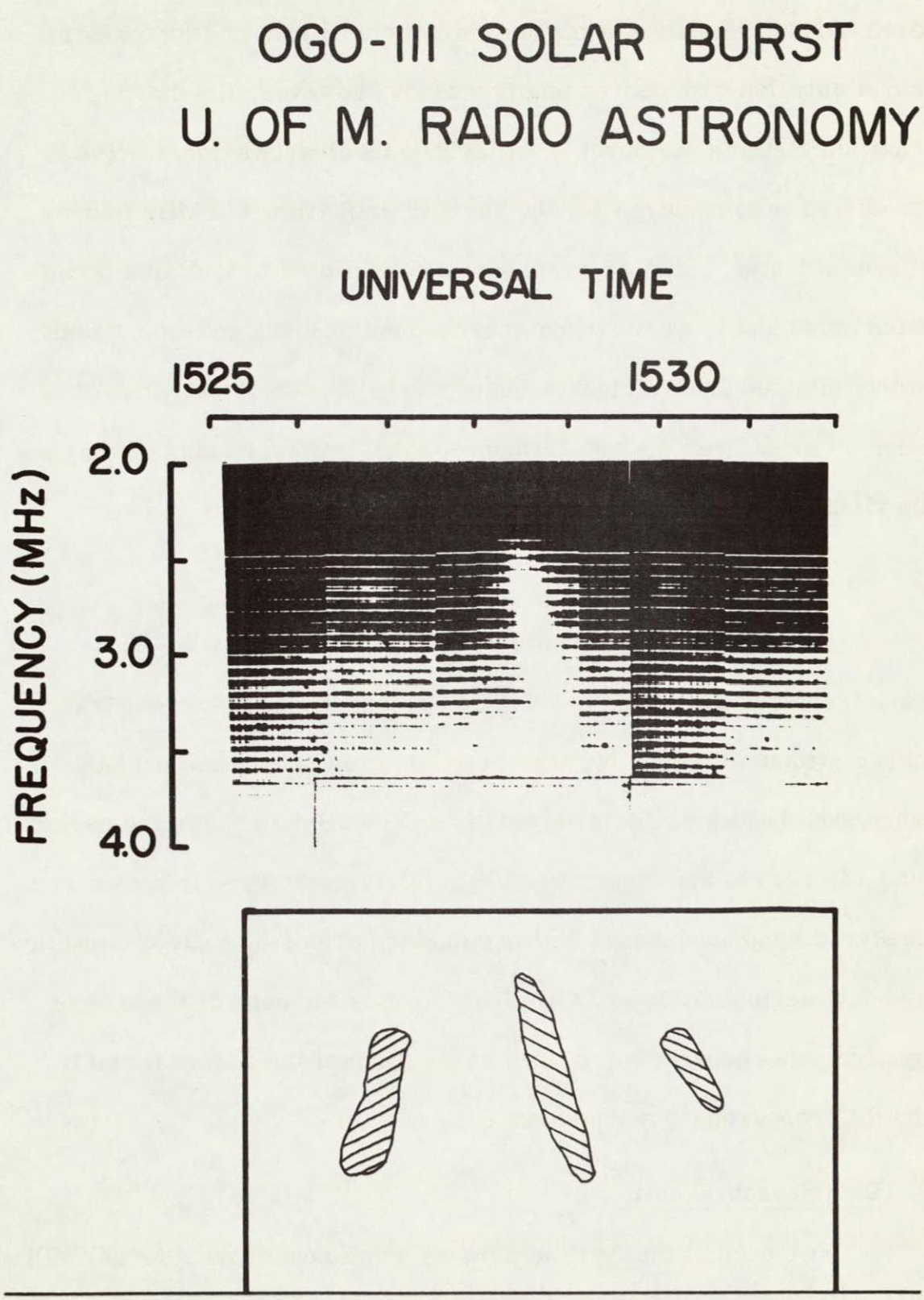

Figure 16. The Appearance of a Reverse Drift Burst on Low-Frequency Data Records.

drift bursts. Because of the decrease in drift rate and increase in burst duration with decreasing frequency, however, the drifting characteristic of the burst is unlikely to be clearly evident. The predicted time required for the burst to drift from 4-2 MHz is over eleven minutes. Such an event would be expected to look like broad-band noise and to show strong enhancement at low frequencies some thirty minutes after a high-frequency Type II event. The drift of such an event over the low-frequency band, however, may or may not be visible.

2. Data Search Procedure

In addition to the normal scanning of all data by the first-pass technique discussed previously, ground-based solar spectral observations of Type II bursts were used to indicate time periods when such bursts could be expected on OGO-III data. For the period June 13, 1966 to September 30, 1967, thirty-eight Type II bursts were observed by ground-based stations during periods of solar observation and data accumulation by OGO-III. The data for each of these time periods was rechecked to permit correlation of the observations in the different frequency regions.

3. Data Search Results

For each of the 38 time periods mentioned above, the OGO-III data were examined and, in two cases, plotted by second-pass processing techniques. Marginal evidence for a Type II burst was seen in one case; no evidence exists for a Type II burst in 37 cases.

It cannot be argued that the failure to detect Type II bursts at low frequencies is due to a lack of sufficient sensitivity. Type II bursts are typically preceded by fast drift bursts; 21 of the 38 bursts discussed here had this feature. In 11 cases, these fast drift bursts were observed by OGO-III (Table 8).

	Importance 1	Importance 2	Importance 3
Observed by OGO-III	0	1	10
Not Observed by OGO-III	3	5	2

Table 8. Correlation of Fast Drift Bursts Observed by OGO-III with TypeIII Bursts Observed from Ground Based Stations

Since the sensitivity limit of OGO-III is between the Importance 2 and 3 levels of ground-based observations, it is clear that during the burst periods in question, the experiment was operating normally and was capable of detecting fast drift burst radiation of Importance 2+.

The case for which marginal evidence of a low-frequency Type II burst is present may be documented as follows. At 1656. 2 UT on 4 February 1967, a fast drift burst was detected by the University of Colorado over the band of 41-18 MHz, and rated as Importance 3. OGO-III detected this burst at 1657. 2; this burst was also rated as Importance 3. A Type II burst, also of Importance 3, then followed at the higher frequencies, lasting from 1707. 8 to 1728 0 Very minor enhancement of the low-frequency band was seen from 1708 to 1712,

and from 1723 to 1730 The first enhancement cannot readily be explained. Interpretation of the second enhancement as Type II radiation requires the assumption of a doubling of the exciting mechanism velocity, since the anticipated lag time is 35 minutes. Also required is an explanation for the decrease in importance from 3 in the 48-41 MHz band to 1- in the 4-2 MHz band

The conclusion reached from the data survey is that Type II bursts are not present at 4-2 MHz at the radiated energy levels detectable by the OGO-III instrument package.

D. Solar Noise Storms at Low Frequencies

1. Noise Storm Characteristics

Solar noise storms consist of background continuum with superimposed bursts of short duration and fine structure (these are designated "Type I" bursts) The continuum intensity appears to exhibit, on the average, a maximum in the frequency range 250-150 MHz, but has been detected at frequencies as high as 2000 MHz (Suzuki, Attwood, and Sheridan, 1964) and perhaps as low as 1.5 MHz (Hartz, 1964). The bursts occur within a narrower range, generally from 350-50 MHz (Fokker, 1965).

Narrow band studies of Type I bursts (Elgaroy, 1961, 1965, 1967, de Groot and Van Nieuwkoop, 1968) have revealed a considerable degree of complexity. Most of the bursts have bandwidths of a few MHz, durations of a few tenths of a second, and a stable center

frequency. Bursts with frequency drift, generally about an order of magnitude smaller than that for fast drift bursts but sometimes of comparable drift rate, have been detected on some occasions.

Continuum radiation is sometimes observed following a Type II burst. Bursts of a "blobby" appearance are often seen within this continuum (Warwick, 1965) These burst/continuum events are known as Type IV solar radio bursts. Such bursts are commonly observed as low as 10 MHz by ground-based monitoring stations

2. Predicted Low-Frequency Characteristics

The limited observations made to date indicate that continuum radiation is to be expected in the 4-2 MHz band Hartz (1964) provides possible evidence for continuum at 1.5 MHz Although sometimes quite strong, this radiation is in general not as strong as burst radiation

The presence of Type I bursts at low frequencies does not seem likely, as no confirmed observations below 50 MHz are extant As with bursts of other types, it might be expected that, if Type I radiation is present at low frequencies, the duration would be considerably increased over that measured at high frequencies.

Type IV bursts, particularly the short-duration intense "blobs", are fairly likely to be present at low frequencies These events are seen periodically at slightly higher frequencies, with typical durations of a minute or so at 15 MHz.

3 Low-Frequency Observations

In attempting to detect Types I and/or IV bursts at low frequencies, it is natural to seek a correlation with events observed by ground-based stations at somewhat higher frequencies For OGO-III the situation is complicated by the high noise environment of the spacecraft. From a study of continuum radiation at higher frequencies it seems unlikely that moderate broadband noise can be detected by the experiment

Three events have been observed which may be provisionally classed as "blobby" bursts. All are narrow band in character, of the order of 1 MHz These events may be briefly described as follows:

Event 167: (9/16/66) This is a three-part event, the first two parts of which form the reverse-drift burst previously discussed. The third part is similar to what Elgaroy (1961) calls a I(s) burst, except that its duration is of the order of one minute and bandwidth somewhat greater than 0. 5 MHz It is interesting and perhaps significant that Elgarõy (1961, Figure V-7, p. 159) also classes as a Type I burst a forward-reverse drift pair strikingly similar to the first two parts of Event 167

Ground-based observations detected an impulsive burst coincident with the first part of Event 167. The

only other coincident ground-based event was Type I radiation from well before to well after the OGO-III event A Type II burst seen nine minutes later at 320-16 MHz was not detected by OGO-III.

Event 472· (3/24/67) This event consists of two blobs with bandwidths of about 1 MHz each and durations of about ten minutes each. No drift is apparent in the blobs, which are separated by about fifteen minutes in time. Two Importance 1 fast drift bursts observed by ground-based equipment at 41-26 MHz during the time period of the first blob were not detected by OGO-III. A gradual rise and fall was seen at 4995 MHz during the initial time period of the second blob.

Event 752: (8/4/67) This event consists of one blob with a duration of approximately 0 6 minutes and a bandwidth of > 0 7 MHz (OGO-III records show only the 4. 0-3 3 MHz portion of the burst bandwidth). No drift is apparent. Coincident ground-based observations show no events except a weak fast drift burst preceding the blob by six minutes (average time delay for a fast drift burst from ground-based detection to OGO-III detection is of the order of one minute).

In addition to the above, UM/RAO Event 754 shows enhancement lasting approximately fifteen minutes over the 4.0-3.2 band. No drift is evident. The intensity of the event indicates a classification as Importance 1 No solar burst activity is reported from the Culgoora, Australia station, the only ground-based radio spectrometer in operation at the time. No spacecraft commands were sent during the period, nor is there any indication of interference

The conclusion reached from the above considerations is that low-frequency observation of noise storm radiation can be termed conditional at best. If solar noise has been observed, it is more likely to have been of Type IV than of Type I Note, however, the observation of Elgarôy (1967) that Type I bandwidth decreases with decreasing frequency, a result not inconsistent with the data discussed here

CHAPTER IV

THE SOLAR CORONA AND ITS BURST PHENOMENA

A. The Nature of the Coronal Plasma

1. The Current State of Knowledge

Dramatic advances in the availability of information concerning the physical parameters of the solar corona have been made during the past two decades. Newkirk (1967) has pointed out that these are due largely to the advent of new techniques and new instrumentation. Much of the new instrumentation has been carried above the earth's atmosphere by spacecraft, thus permitting coronal studies over a very wide frequency range

The current state of knowledge of the coronal plasma has been the subject of recent reviews by Billings (1966) and Newkirk (1967). Both authors emphasize the scarcity of firm determinations of the physical parameters, particularly at coronal heights above approximately two solar radii (as measured from the center of the sun). Since the properties of the corona at much greater radial distances are of interest here, this chapter will discuss the present status of information on the "far" corona, which is arbitrarily defined as that portion of the corona beyond three solar radii This cutoff is chosen because it is generally considered to represent the outer limit of ground-based solar observations, except during eclipse.

2. Density Structure

The density structure of the corona has been subject to particularly active investigation during the past few years. The primary methods used have been coronal photometry, radio burst measurements, radio source occultations, and direct sampling by spacecraft. Theoretical models of the density structure of the solar wind have also been developed and compared with observational results.

Essentially all of the determinations of density structure inside two solar radii have been made by the method of coronal photometry (van de Hulst, 1950). The method involves sensitive polarimetry, and rests upon the assumption that the K corona (the true continuum corona) produces all the measured polarized radiation, and that the radiation of the F corona (the Fraunhofer corona, due to scattering by interplanetary dust) is both unpolarized and spherically symmetric. This assumption is untenable past 6 $R_\odot$ at which point the method is no longer valid (Billings, 1966). The combined results obtained by various investigators (Pottasch, 1960; von Klüber, 1958; Newkirk, 1961, Ney, et al., 1961; Gillett, Stein, and Ney, 1964) define a model which might be called the "average equatorial coronal density structure". Although such a model is of considerable value to discussions of normal coronal properties, it nonetheless overlooks the substantial variations in coronal density with solar latitude, solar cycle, and distinctive coronal features.

The electron densities at distances from 10 $R_\odot$ to 80 $R_\odot$ are currently obtained by observation of the occultation of discrete radio sources by the solar corona As the sources pass near the sun their observed radiation patterns are broadened by scattering and refraction of the radio emission by the solar wind electrons. The theory of the method has been given by Erickson (1964). Although the results are qualitatively reasonable, the densities appear to be as much as 10% in error in some regions (Newkirk, 1967). Closer to the sun than approximately 10 $R_\odot$, the electron density is too great to permit occultation measurements.

Space probes have made direct measurements of solar wind electron densities. In all cases these have been at solar distances $R \geq 100\ R_\odot$, and do not apply to the region of interest in this discussion.

In addition to the methods discussed above, coronal densities may be deduced from interferometric solar radio burst data which produce values for the spatial velocity of the burst exciter as a function of frequency, thus providing a density model. The assumption of emission at local plasma frequencies is necessary to this approach. The validity of the assumption is reviewed later in this chapter. Malitson and Erickson (1966) have shown that these measurements imply a density which is about ten times that derived by van de Hulst (1950) for the maximum corona, for distances as great as 10 $R_\odot$. Observations of high-density coronal streamers (Schmidt, 1953; Newkirk, 1961) agree with the Malitson-Erickson model, suggesting

that radio bursts originate preferentially along the dense axes of active region streamers. The sole experimental analysis of the density structure for $R > 4\ R_{\odot}$ has been done by Hartz (1964). He assumed Malitson-Erickson densities of ten times the van de Hulst maximum for the region $3 > R/R_{\odot} > 15$. This model is shown in Figure 17 for the region $1 > R/R_{\odot} > 15$, together with the corresponding models for the "quiet corona" from Whang, Liu, and Chang (1967) and Noble and Scarf (1963) These models are supported by interferometric radio burst observations, and give similar density profiles except for small differences very near the solar surface

3 Temperature Structure

The inner corona maintains a temperature that is approximately $1.5 \times 10^6\ ^{o}K$ (Newkirk, 1967) Over active regions this value may increase to $2 \times 10^6\ ^{o}K$ or greater (Billings, 1966). At increased radial distances from the chromosphere/coronal interface the temperature will decrease, the gradient being determined by the energy supply from the interface, losses due to thermal conduction, and the escape of material into the solar wind. Since evidence indicates that radio bursts occur principally within coronal streamers (the properties of which must be determined largely by the underlying active regions), it is the temperature structure of streamers beyond three solar radii which is of interest.

Temperatures above active regions are determined from solar radio bursts using the method developed by Boischot, Lee and

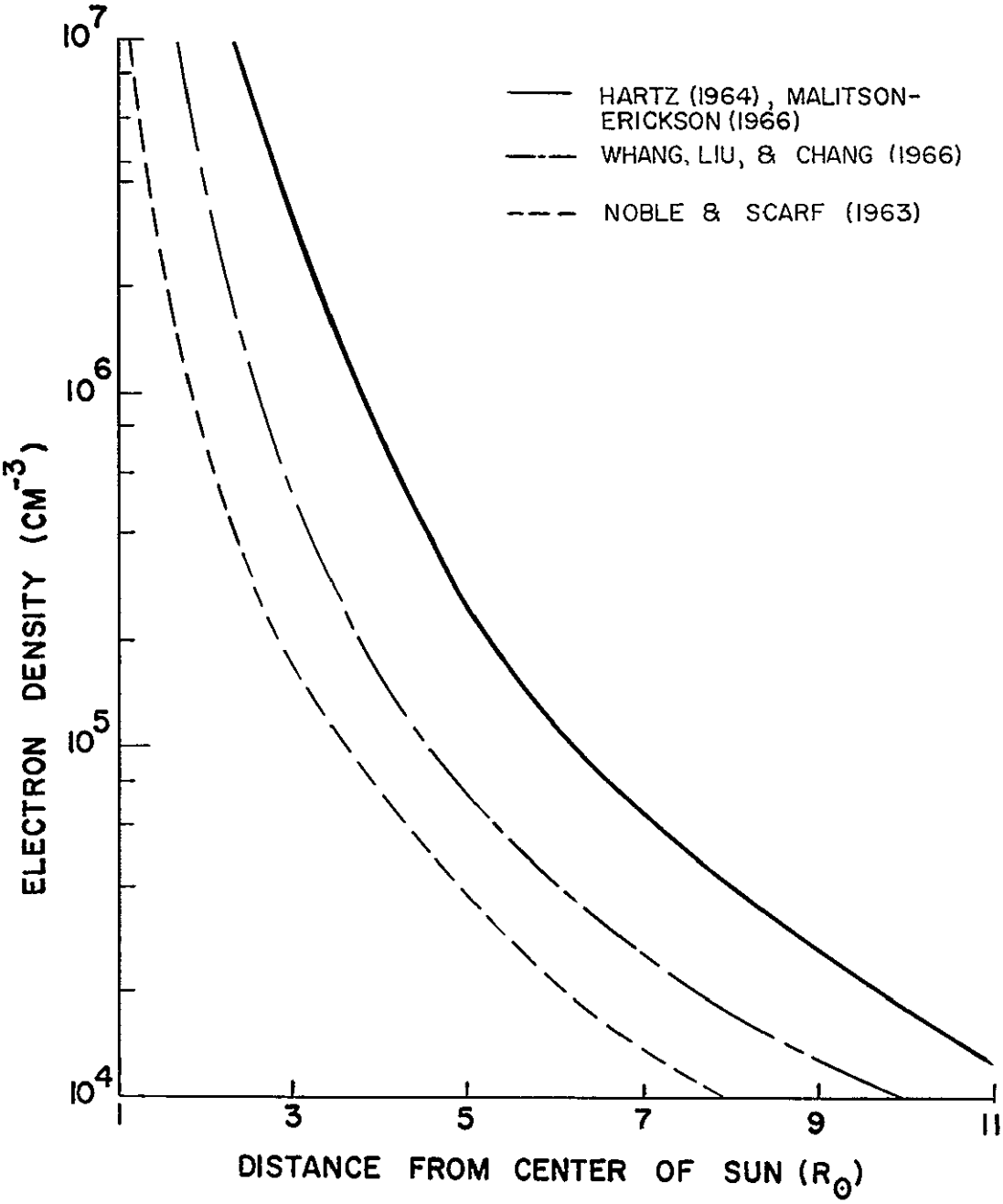

Figure 17 Electron Density Models of the Corona

Warwick (1960). The theory states that, under the assumption that the plasma oscillations are damped only by collisions, the electron temperature is related to the frequency of emission and to the e-folding time of the burst (the time in which the amplitude decreases to 1/e of its maximum value) by

$$T_e = 0\ 65 \times 10^{-4} f^{4/3} \Delta t^{2/3} . \qquad \text{(IV-1)}$$

A number of coronal temperatures for low frequency radiation have been computed through application of this equation (Hartz, 1964; Boischot, 1967; Slysh, 1967) The results are plotted in Figure 18 along with those resulting from the Whang, Liu, and Chang and Noble and Scarf models discussed previously. A model by Hartz and Warwick (1966), based on Hartz's observations, is also shown. It is apparent that the observed temperature gradient is much steeper than that predicted by the models Newkirk (1967) has considered whether the observations can be made consistent with theory He notes that the assumption of a density model is a necessary first step in the temperature determination, and gives evidence for a substantial increase in the ratio of the density of streamers over the background density at large radial distances Measurements of these densities are extremely difficult to make, but the work of Sandlin, Kooman, and Tousey (1968) does not seem to support such an increase.

It appears safe to conclude that the temperature profile of a dense coronal streamer is even less well-defined than is the density

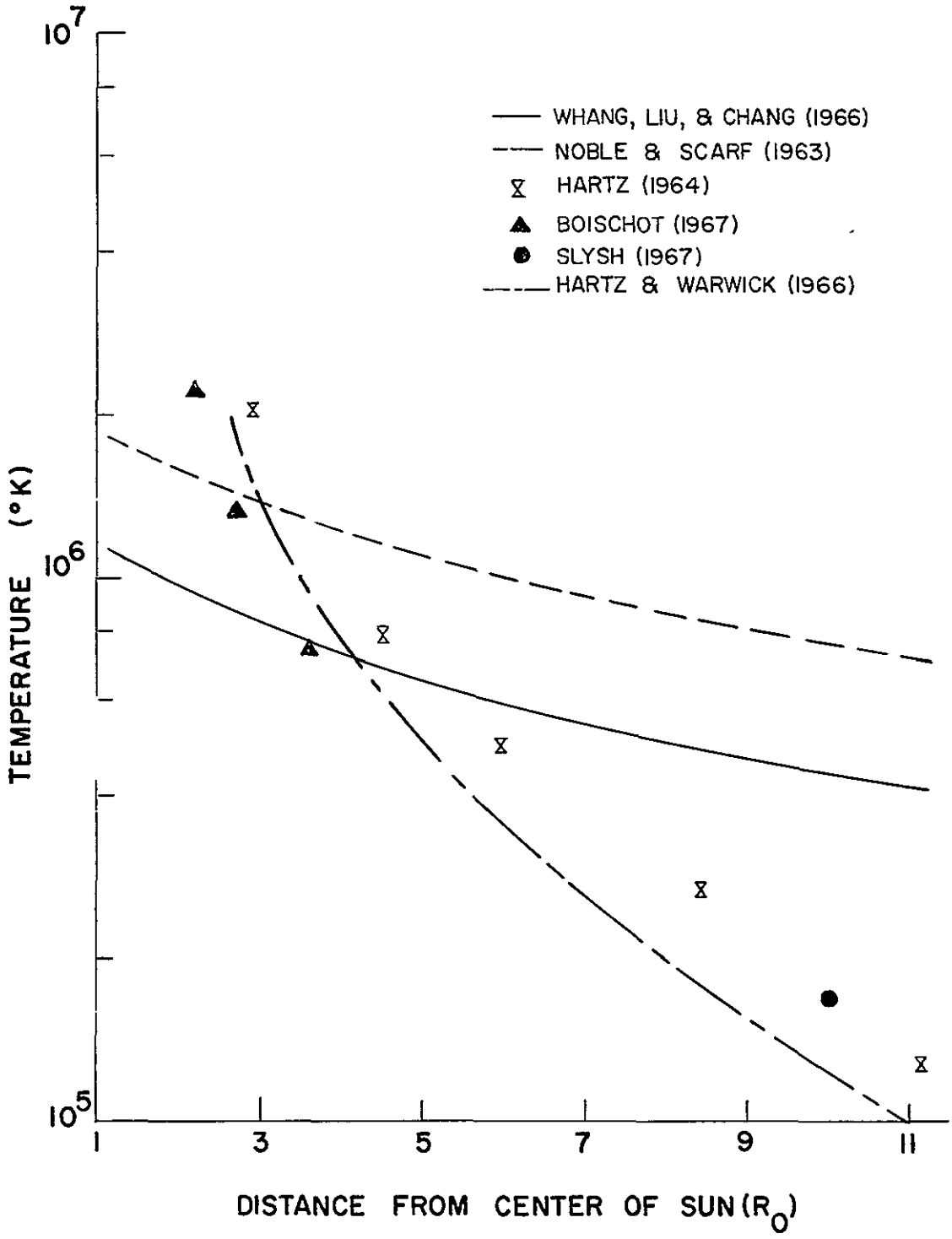

Figure 18. Temperature Models of the Corona

profile. It is not really surprising that this should be so. A cursory glance at solar eclipse photographs will show a wide variation in coronal streamer densities. When this variation is combined with the uncertainties involving the change in coronal density over the solar cycle and as a function of latitude, and the fact that various observers have observed different active regions, it is perhaps realistic to be satisfied with observationally-based models which vary in electron density and electron temperature by factors of three.

4. The Structure of Coronal Streamers

Because solar radio burst observations have suggested that the bursts originate within coronal streamers, it is appropriate to describe briefly the current state of knowledge regarding streamer structure and dynamics. These characteristics have recently been summarized in a dissertation by Bohlin (1968), on which much of this discussion is based.

The morphology of coronal streamers is very poorly known. Because of their small radiated flux levels in comparison with that of the solar disk, they have been detected only during solar eclipses or by rocket or balloon flights of coronagraphs (Newkirk and Bohlin, 1965; Sandlin, Koomen, and Tousey, 1968) The short time scale of such observations is a significant handicap to the development of a consistent picture of the history of a streamer. Bohlin's (1968) approach was to identify a streamer on a balloon photograph with a

ground based coronameter feature, and to assume that further existence of that coronameter feature implied continued existence of the streamer itself. In this way he derived a lifetime which can at least be regarded as an upper limit for the streamer duration. The one streamer which could be well studied had a lifetime of 4-1/2 solar rotations. Eight other streamers for which incomplete data were available had an average lower limit lifetime of 1 4 solar rotations.

Several streamer density models have been proposed, based largely on analyses of eclipse photographs Comparison of the results of Schmidt (1953), Michard (1954), Saito (1959) and Bohlin (1968) shows differences of as much as a factor of ten at distances greater than 2 $R_\odot$ Since different streamers were analyzed in each case, a difference in density structure from one streamer to another is implied. A potential further complication for the density determination is that the three-dimensional density distribution of a given streamer is not known; such lack of knowledge directly affects the density determination. Bohlin (1968) has derived a three-dimensional density distribution for a model streamer In his model a radially-dependent core density $N_o(r)$ decreases as a gaussian in directions perpendicular to the core line The 1/e-density dimensions of the model streamer at r_o = 1-1/4 $R_\odot$ are $\sim 25^o$ in latitude by $\sim 40^o$ in longitude This result may well have little application at 5 $R_\odot$, however

The evolutionary development of a streamer is not known, but Newkirk (1967) has hypothesized that the streamer begins as an

enhancement overlying an active region, later developing an extended appearance. Still later the magnetic field, which has acted as a channel for electron streams and for the solar wind, decays, and the extended portion of the streamer slowly merges into the background corona. In this picture an enhancement in the lower corona would exist at least as long as the associated streamer, and almost certainly longer than the radio burst lifetime of the streamer.

The limited information available suggests that a coronal streamer of substantial radial extent (i.e., more than 1 $R_\odot$ above the solar surface) is generally associated with a combination of an active plage region and a prominence. Bohlin (1968) has suggested that the existence of the prominence indicates the presence of the necessary magnetic field configuration, while the active plage region supplies the enhanced source of plasma needed for the eventual growth of the streamer.

5. Kinematic Structure

A dynamic corona has been implied by knowledge of solar rotation, and confirmed by observations of the solar wind It is probable that most coronal structures, certainly including streamers, owe their form to the interaction of the solar wind and the underlying magnetic fields (Newkirk, 1967) In studying solar radio bursts, however, a principal question is whether the normal kinematic structure of the corona is significant when compared with the velocities

involved in burst mechanisms. Relevant measurements place the solar wind velocity at approximately 500 km/sec (Neugebauer and Snyder, 1966), the velocity of slow-drift (Type II) radio burst exciting burst particles at approximately 1000 km/sec (Kundu, 1965) and the fast-drift (Type III) radio burst exciting particles at 0.1 - 0.6 c (Malville, 1961). Thus the dynamic structure of the corona may possibly affect conclusions about slow-drift bursts, but will not be a factor in the study of fast-drift bursts.

6 Magneto-Ionic Structure

It is difficult to establish the presence of magnetic fields in the corona and more difficult to map their structure. Billings (1966) has observed that many measurements indicate the existence of such fields, but the magnitude of the fields is quite uncertain. Takakura (1964) has given arguments from radio measurements for fields of the order of ten gauss at plasma frequency levels of 50 MHz (2.2 R_O) Boischot and Clavelier (1967) have derived a field of 0.5 gauss at a distance of one solar radius above the photosphere These appear to be the only determinations of coronal magnetic fields to date.

B. Solar Particle Bursts

1. Observations of Particle Burst Events

The existence of streams of particles emanating from the photosphere or chromosphere and passing through the corona is crucial to the generally accepted theories of solar fast-drift radio

burst production Evidence for particle emission has been suggested for many years by the magnetic storms in the earth's atmosphere following large solar flares. Confirmatory evidence for solar particle emission has been obtained with rockets and spacecraft.

Equipment capable of detecting solar particle emission at moderate or high energies has been flown on a number of different spacecraft, but only within the past few years have experimenters been able to measure the characteristics of the particles. The standard equipment configuration for this work has been a battery of Geiger-Muller tubes with different threshold levels, sometimes combined with ion chambers or scintillation counters. Such experiments have now been discussed for Mariner IV by Van Allen and Krimigis (1965), for IMP I and IMP III by Anderson and Lin (1966), for IMP I, II, III, Mariner IV and Explorer 33 by Lin and Anderson (1967), and for IMP III, Explorer 33 and OGO-III by Lin, Kahler and Roelof (1968). Lin and Anderson (1967) have given a summary of solar electron events for 1964, 1965 and 1966; during this period 34 such events were observed by one or more of the spacecraft. In no case have the observations been made at distances greater than 60,000 miles from the earth. It appears safe to assume that particles observed near the earth have passed through the far corona. Their characteristics are thus of significance for the study of radio bursts originating from regions through which the particles passed.

Detection of energetic electrons from the sun is much more frequent than that of protons The low masses of the electrons make it much easier to accelerate them to the typical speeds of several tenths of the speed of light inferred for radio burst exciters by observations These facts suggest that radio bursts from the outer corona are directly related to the propagation of energetic electrons Such a relationship will be assumed throughout this paper

2 Characteristics of Particle Burst Events

The basic quantity measured by particle detection experiments is the number of particles within a certain stated energy range, per steradian cm^2 second If the instrument acceptance angle is well known, a spacecraft moving across the line of particle travel can also measure the lateral spread of the propagating particles Other spatial characteristics of the particles can be deduced if an event is observed by a number of spacecraft having substantially different orientations with respect to the earth-sun line

The electron energy threshold level for all experiments of this type has been 40 keV This is precisely the energy range of interest for solar burst studies, since the velocity of a 40 keV electron is 0 28 c Mariner IV observations suggest that the spectrum falls steeply with increasing energy (Van Allen and Krimigis, 1965) The range of peak intensities measured to date is very wide Values for 34 electron events observed during 1964-1966 range from 10 to 5700

electrons per sr-cm^2-sec (Lin and Anderson, 1967). As is the case with many solar phenomena, the correlation of electron fluxes with flare importance is only suggestive. Correlations attempted with solar burst or X-ray burst data are also inconclusive. The agreement with radio burst data tend to be good at high electron flux levels and poor at low flux levels. It is tempting to suggest that a certain threshold number of electrons is required for the initiation of coronal plasma waves which are of sufficient amplitude to produce radio emission

3. The Observational Model for Electron Bursts

As observations of energetic electrons increase in number, it is becoming possible to describe not only the characteristics of the electrons themselves, but also the extent of their spatial distribution and their relationships to the conditions of the interplanetary medium It appears that a high electron flux is observed only when a field line of the interplanetary magnetic field is connected to a point on the sun near the occurrence of a flare. This creates the conditions necessary for rapid motion of the electrons away from the point of injection. The electrons spiral out along the magnetic field line, incidentally exciting plasma oscillations as they move Since coronal streamers are thought to form around magnetic field lines, the electron densities derived from solar radio bursts are representative of coronal streamer densities.

A final parameter, that of the total electron emission from observed events, has been derived from the diffusion model of Krimigis (1965) by Van Allen and Krimigis (1965). From their observations, they estimate the total emission as 10^{33}-10^{34} electrons sr^{-} It appears reasonable to take these values as order-of-magnitude estimates for the number of electrons $>$ 40 keV emitted during a particle burst event.

C Fast Drift Solar Radio Bursts

1. Introduction

Fast drift solar radio bursts comprise by far the most common type of solar radio activity at meter and decameter wavelengths. First observed and described by Wild (1950) at 120-70 MHz, they are now being studied in detail at frequencies less than 10 MHz. Such observations have been reported by Sheridan and Attwood (1962), Hartz (1964), Boischot (1967), Slysh (1967), Suzuki, Attwood and Sheridan (1964), Malitson, et al. (1968), and Haddock and Graedel (1968) The burst frequencies studied extend to 100 KHz and possibly to 30 KHz. Ground-based observations are limited by the ionospheric cutoff frequency, which at times may extend to 4 MHz but is generally in the range of 10-7 MHz The published data on observations below the ionospheric limit have been acquired from spacecraft-borne instrumentation aboard Alouette I (Hartz, 1964), Venus II (Slysh, 1967), and ATS II (Stone et al., 1967; Malitson, Alexander, and Stone, 1968);

none of these experiments has observed enough burst events to make a definitive study of burst characteristics at low frequencies.

It has been established in Chapter III that fast drift bursts the only radio events observed often enough and identified with sufficient certainty to merit discussion here. For these reasons a discussion of the characteristics of solar radio bursts other than fast drift bursts and the associated Type V bursts is omitted, except for brief descriptions relevant to the data search described in Chapter III

Observations of solar radio bursts are typically made either with fixed-frequency receivers, or with radio spectrometers. The latter are essentially narrow band tunable radiometers whose reception band is repeatedly swept across the frequency range of interest at a rapid rate Fixed-frequency receivers are much easier to use and to calibrate, but fail to give as comprehensive a picture of solar radio events as that provided by the radio spectrometer.

The characteristics of fast drift solar radio bursts have been summarized by Wild, Smerd, and Weiss (1963) and by Kundu (1965) This discussion will concern the characteristics of fast drift bursts for frequencies less than 10 MHz Higher frequency results will be mentioned only if germane to low frequency work.

Many of the coronal parameters computed from observations depend on two critical factors: the electron density model used, and the assumptions made concerning the damping of the plasma oscillations

producing the radio event Since results depend so heavily on these assumptions, it is important to separate observational data from derived data and to treat each separately whenever possible.

2 Frequency Drift

Fast drift bursts, as their name implies, show a rapid downward drift with time in the frequency of maximum intensity The drift rate decreases with frequency, in the approximate relationship (Wild, 1950)

$$-\frac{df}{dt} = \frac{f}{4\ 5} \text{ MHz sec}^{-1} . \qquad \text{(IV-2)}$$

The sole reported drift rate at low frequencies is by Boischot (1967) over the range 40-4 MHz His mean drift rate at 4 MHz, based on only three bursts, is 0. 125 MHz/sec It should be noted that the drift rate is one burst parameter which is not model-dependent.

3. Energy Spectrum

The radiated energy flux density spectrum of the typical fast drift burst shows a logarithmic decrease as the frequency increases (Wild, 1950). Measurements of the low-frequency energy spectrum over a wide frequency range have not been made, but much information regarding the flux densities of bursts may be derived from values reported in the ESSA Solar Data Bulletins, and other similar sources.

4 Burst Duration

The profile of a fast drift burst typically shows a steep rise to the maximum level, followed by a quasi-exponential decay. At successively lower frequencies this profile retains the above characteristics, but becomes progressively broader and smoother. Although durations of a few seconds describe bursts at several tens of MHz and above, the duration of lower frequency bursts may be a minute or more

The measured duration of a solar burst is dependent on the sensitivity of the equipment being used With instruments which record the quiet sun level above the system noise level, the derived values may be considered satisfactory If this sensitivity is not reached, the derived values may be regarded only as lower limits (Hughes and Harkness, 1963) Most writers have not stated this limitation explicitly but it is certainly implied, particularly for observations made from spacecraft. This problem will be discussed in more detail in Chapter V.

5 Harmonic Frequency Emission

It is not unusual for fast drift bursts to show two components, one of which duplicates the features of the other but at about twice the frequency (Wild, Murray, and Rowe, 1954) The effect is much more

recognizable in slow drift burst events; in fast drift bursts the rapid frequency drift combined with a fairly broad bandwidth tends to merge the fundamental and second harmonics This merging effect is more noticeable at lower frequencies because of the increase in burst duration Since the harmonic radiation reflects the conditions existing in the region of the fundamental it is possible, at least in principle, to separate fundamentals from harmonics by a study of the properties of individual bursts

Figure 19 illustrates the sequence involved in the production of burst radiation The plasma frequency level for a particular frequency is defined as the coronal radial distance for which the electron density is appropriate to the frequency in question [see equation (V-2), p. 107]. The interval between time increments is given by the linear distance between the plasma frequency levels divided by the velocity of the electron stream exciting the burst The former changes with frequency due to the decrease of the density gradient in the outer corona

Figure 19 shows the burst development for observation with a sweep frequency receiver in the 200-150 MHz band. At time t_1 the electron stream arrives at the 200 MHz level, exciting fundamental radiation at 200 MHz and second harmonic radiation at 400 MHz. (The bandwidth of the radiation is assumed to be small compared to the bandwidth of the receiver. This assumption is supported by observational arguments discussed in Chapter V I) The electron stream

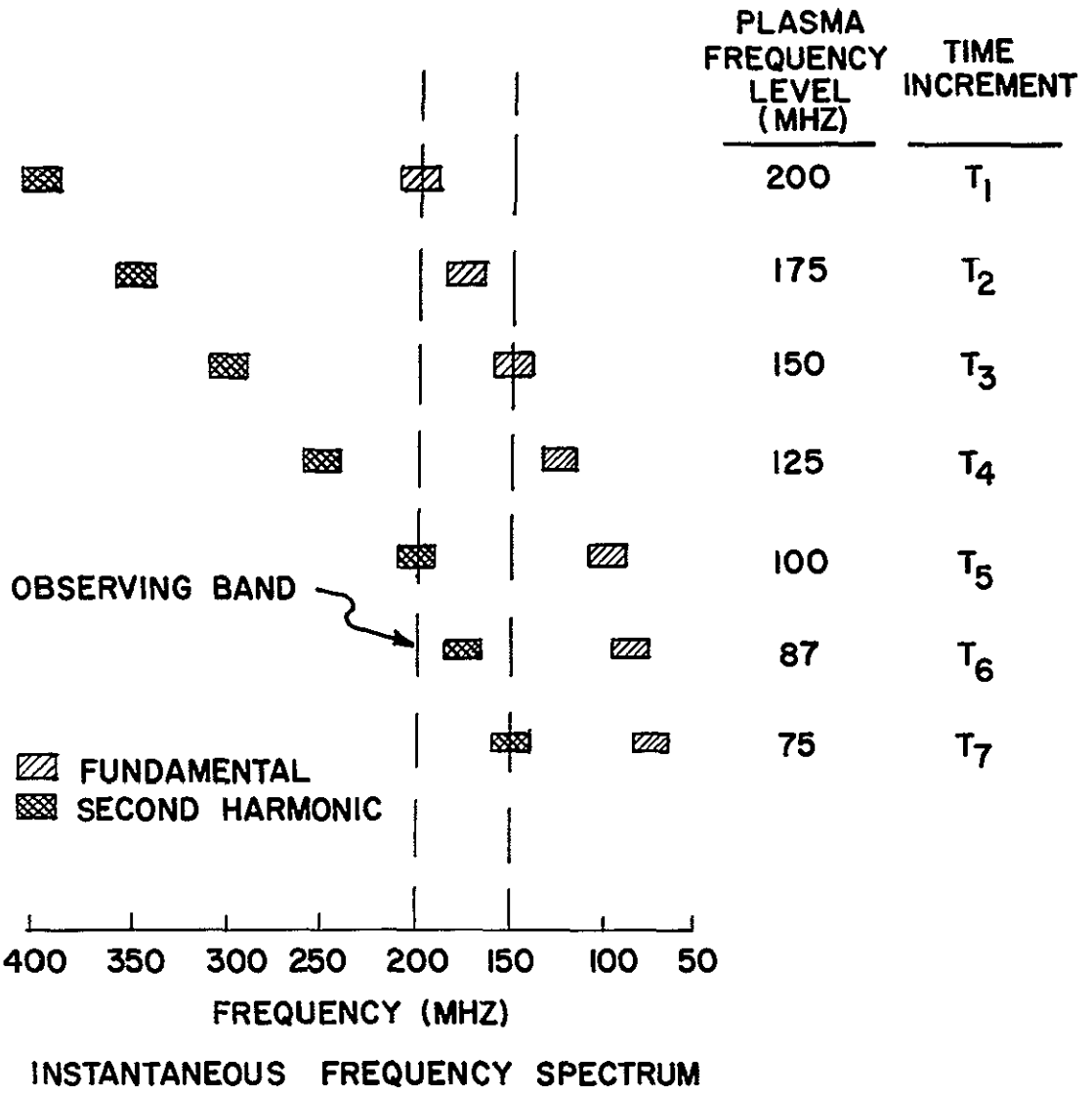

Figure 19 Observation of Fundamental and Second Harmonic Radiation From a Fast Drift Solar Radio Burst

travels to the 175 MHz and 150 MHz levels, the enhanced radiation at these frequencies is observed The drift rate of the observed impulse is

$$DR = \frac{(200-150)\ \text{MHz}}{(t_3-t_1)\ \text{sec}}$$

and the burst duration depends upon how rapidly the radiation process is damped.

The electron stream continues its motion, arriving at the 100 MHz level At this point a second burst begins in the 200-150 MHz band, as a result of the second harmonic of the 100 MHz radiation Harmonic radiation from the 100-75 MHz levels completes this burst sequence in the 200-150 MHz observing band. The drift rate of the latter burst in the observing band is

$$DR = \frac{(200-150)\ \text{MHz}}{(t_7-t_5)\ \text{sec}} \ .$$

The difference in drift rates between the two bursts depends on the difference between (t_3-t_1) and (t_7-t_5) At the frequencies discussed here these differences are small, but they become increasingly larger at lower frequencies This suggests that harmonic radiation should be easier to detect at low frequencies than at higher frequencies At lower frequencies, however, the burst mechanism is damped much more slowly [see equation (IV-1)] If the damping time for the fundamental 200-150 MHz burst illustrated is comparable with or greater than (t_5-t_1) the harmonic burst may be difficult to

distinguish from the fundamental. A further complication is that the second harmonic may become increasingly weaker than the fundamental at lower frequencies (Wild, Sheridan, and Neylan, 1959; Shain and Higgins, 1959). The detection of harmonic bursts is worth investigating, however, since successful detection doubles the frequency range of radiation, and hence the coronal distance range, which can be studied

6 Clustering

Fast drift bursts exhibit a strong tendency to occur in groups, sometimes with as many as ten in a group. Generally the bursts within a group tend to have similar characteristics. Often the bursts are quasi-regularly spaced in time (Wild, Smerd, and Weiss, 1963). Illustrative examples of this clustering indicate that the individual bursts within a group are often barely resolved at 50 MHz. With the longer duration of bursts at lower frequencies and the smearing due to harmonics, we would expect to observe much less of a clustering tendency on low-frequency records

Two distinct characteristics of clustered bursts have been suggested by solar radio spectral observations. First, the individual bursts within a cluster seem to be of similar spectral appearance and almost identical source position (Wild, Sheridan, and Neylan, 1959), indicating that the cluster constitutes a single event. Second, Maxwell, Howard, and Garmire (1960) have found that the intensity of the

individual bursts in a group appears to increase with the number of bursts comprising the group

7 Type V Solar Radio Events

About ten percent of all fast drift bursts are followed by broadband continuum radiation which is strongest at low frequencies and may last for one to three minutes at a few tens of MHz (Kundu, 1965). The properties of initial position, variation of position with frequency, and polarization for the Type V event are often similar to those of the associated fast drift burst (Wild, Smerd, and Weiss, 1963) It appears, therefore, that a direct cause-and-effect relationship exists between the fast drift and type V bursts Warwick (1967) has recently proposed that Type V bursts are merely bursts emanating from regions which have been heated by the exciters of previous fast drift bursts. This model appears to explain many of the properties of the Type V burst; the extended duration results from the local temperature increase. [Note the temperature dependence of equation (IV-1)] The model implies that Type V radiation would be likely to occur following a long series of intense fast drift bursts; this implication has not been verified observationally An argument against the model is that it predicts harmonics similar to those produced by a fast drift burst These have not been observed in Type V radiation (Kundu, 1965). In addition, recent solar interferometry (Kai, et al , 1968) suggests that a position shift between associated fast drift and Type V bursts may commonly occur.

The intensity of Type V radiation at low frequencies indicates that it should appear when observations are made at frequencies substantially lower than 10 MHz. The problems of increased duration, however, may be expected to make Type V radiation difficult to separate from other forms of broadband solar radio noise

8. Correlation With Optical Flares

Attempts to correlate fast drift bursts with other solar phenomena have been made ever since the first detection of the radio bursts. The association of bursts with optical flares has proved to be productive. A strong positive correlation exists, although the numerical figures which are derived vary according to the completeness and consistency of the flare list used, and with the association criterion selected. A noninterferometric study of such an association, furthermore, must assume that a radio burst occurring within the limits of the association criterion (for example, within $\pm$ 1 minute of a flare period) is associated with the flare detected within that period. This assumption overlooks the possibility that some other occurrence, such as a subflare below the detection limit, is the true radio burst-associated event. Interferometric observations by Erickson (1962) at 26 MHz, however, indicate that the assumed association is generally confirmed

Perhaps the most careful study of the flare/burst correlation has been that of Malville (1961, 1962a) Using a consistent flare list of which 93% were subflares, he found that 76% of the bursts within

the range 580-25 MHz occurred within ± 1 minute of the flare period and that most of these begin within ± 1 minute of the flash phase. The implication is that the stage of most rapid growth of the instability is the stage during which acceleration of electrons to very high energies takes place

9 Positional Measurements

Interferometric observations of solar radio bursts (Wild, Sheridan, and Neylan, 1959) indicate that burst events successively lower in frequency occur progressively further out in the corona. Warwick (1965) has confirmed this effect for frequencies as low as 12 5 MHz, and finds in addition that at a given frequency the bursts in some cases vary in position by as much as a solar radius The results are consistent with emission taking place at or near the local plasma frequency, and with temporal variations in the coronal density structure.

Measurements of the relative position of fundamental and second harmonic radiation have not fitted so neatly into the theoretical picture At a fixed frequency the anticipated result is that harmonic emission would originate at greater radial distances than would the fundamental, and at a later time. Observations by Smerd, Wild, and Sheridan (1962), however, indicate that the position of the second harmonic is often inside that of the fundamental. Although difficulties of

identification are present, the effect seems to be real. Efforts to explain the observations theoretically have not been particularly convincing.

CHAPTER V

THEORETICAL STUDIES OF FAST DRIFT SOLAR RADIO BURSTS

A Introduction

Detailed theoretical studies of solar radio bursts have been done only within the last ten years. Although considerable progress has been made, many aspects of the creation and propagation of the burst radiation are still poorly understood

In this paper only the low-frequency segment of the radio burst spectrum is considered The restriction of the discussion to this spectral region permits certain simplifying assumptions to be made; it also introduces some uncertainties. These assumptions and uncertainties will be pointed out as they arise, and their implications concerning the solar corona will be discussed

Metric and decametric solar radio bursts exhibit a specific set of characteristics which must follow naturally from any comprehensive theory These characteristics may be summarized as follows:

(1) The velocity of an exciting disturbance is in the vicinity of 0 15 c - 0 6 c and appears to be nearly constant over path lengths of several solar radii (Wild, 1950).

(ii) The duration of a burst increases with decreasing frequency, from a fraction of a second at several hundred MHz to a minute or more at a few MHz (Kundu, 1965).

(iii) Bursts show a strong tendency to cluster in groups of from two to ten Frequently the most intense events are those which exhibit clustering (Wild, Smerd, and Weiss, 1963)

(iv) The profile of a burst (i. e , the variation of flux density with time at a given frequency) shows a fairly rapid rise to maximum and a slower quasi-exponential decay (Wild, 1950)

(v) The second harmonic of a burst is commonly seen, generally at radiated flux levels comparable with the fundamental (Wild, Murray, and Rowe, 1954).

(vi) Interferometry has demonstrated that bursts may occur at a substantial distance (one solar radius or more) above the photospheric surface of the sun (Wild, Sheridan, and Neylan, 1959).

(vii) The available evidence indicates that the disturbance creating a burst travels outward from the sun along the axis of a coronal streamer (Newkirk, 1967)

This chapter will deal with the development of solar radio bursts in one observed frequency band. The aim is to compare the theoretical burst profiles with those observed by the OGO-III experiment. In this initial treatment the complicating factors of burst multiplicity, harmonics, and profile changes as a function of frequency are not considered An extension of this approach to explain fully all the observational characteristics listed above is obviously desirable. Such an extension is outside the scope of this paper, however, and in most cases beyond the firm knowledge of coronal properties and plasma physics theory

B. The Injection of Electrons Into The Corona

1 The Basis of Solar Burst Theory

A prerequisite to the emission of fast drift solar burst radiation from the corona is excitation of the coronal plasma Two mechanisms for excitation have been proposed. In the electron stream mechanism, a packet of electrons is injected into the corona at speeds of several tenths of the speed of light. These electrons then produce plasma oscillations (Wild, Smerd, and Weiss, 1963) The second method uses magneto-hydrodynamic (MHD) waves to initiate the plasma oscillations (Zirin, 1966).

The electron stream theory is subject to several constraints. Large numbers of electrons must be propagated to excite plasma oscillations to the degree deduced from the observed radiation.

In addition, the velocity distribution of the electrons must be such as to explain the observed burst profile. Finally, the stream must be guided radially outward from the point of injection.

The theory of excitation by MHD waves is also restrictive. The most stringent requirement is that of maintaining the balance between the magnetic field pressure and the local gas pressure over large radial distances (Malville, 1961). This is particularly true when the constant velocity of a burst impulse is considered Such a velocity requires that B^2/ρ be unchanged over the total path length of the wave The unlikelihood of such a balance in view of the coronal magnetic fields inferred from observations has led to the rejection of MHD waves as a general burst exciting mechanism (Warwick, 1967).

2. Observational Properties of Injected Electrons

Since it is generally assumed that fast electrons are the effective burst exciters, it is desirable to specify the properties of these electrons. The basic information desired is the method of producing the electron packets, the number of electrons produced, the time scale for their production, the distribution of the electrons in velocity space and the guiding of the electrons. It should be noted that the electron production mechanism is not critical to the discussion if the other parameters can be determined

Evidence for the existence of high energy solar electrons has been presented in Chapter IV. It does not appear that the observations which have been made to date are capable of providing definitive

information on the electron velocity distribution. The figure for the total number of electrons seems to be better defined. The evidence of Van Allen and Krimigis (1965) and Takakura (1967) indicates that a packet of 10^{33} electrons is a typical figure for an electron burst event. The resolution of solar radio telescopes is too low to measure accurately the coronal volume from which the emission comes. Thus the spatial dispersion of the fast electrons in the corona is an open question

3 Methods of Electron Injection

A theory of electron injection must satisfy several requirements The physical conditions invoked must be common enough to be reproduced by the solar plasma several tens of times a day (this is the observed frequency of solar radio bursts during the active part of the solar cycle). Production of clustered bursts requires injection of up to a dozen similar electron packets within a period of several seconds, each packet containing on the order of 10^{33} electrons. The injection mechanism must not produce a large optical flux, since many radio bursts coincide with no observable optical phenomena.

Several processes have been proposed for electron injection. These have been briefly summarized by Takakura (1967) It is unclear whether any of the processes could be effective on the sun. Because of this uncertainty, the properties of the injected electrons must be regarded as unknown

Although the form of the velocity distribution is not known, it seems reasonable to expect it to be approximated by one of two models. The first is a damped Maxwellian distribution, while the second is a Gaussian distribution of undefined spread. The first model describes the injection of a group of electrons whose velocity distribution follows a very high temperature Maxwellian curve. The second model describes injection of a group of electrons with a very restricted range of high velocities In both cases the maximum of the distribution must be centered at or near a velocity V_o which is typical of the velocity of radio burst exciters The distribution of the injected electrons must be superimposed upon the local Maxwellian distribution existing in the emission region under study. At 5.5 $R_\odot$ the temperature[6] can be taken as 7×10^5 ^oK (Whang, Liu, and Chang, 1966) The resulting Maxwellian distribution and the two injected electron distributions being considered are shown in Figures 20 and 21 for $V_o = 0.25$ c. These distributions will be used as a basis for the discussion of the conversion of the electron energies into plasma waves and subsequently into electromagnetic radiation

C. Production of Plasma Waves

The high temperatures and low densities present in the corona combine to create a state of very high ionization As a result of the

---

[6] In this paper "temperature" will be used specifically to designate the electron kinetic temperature.

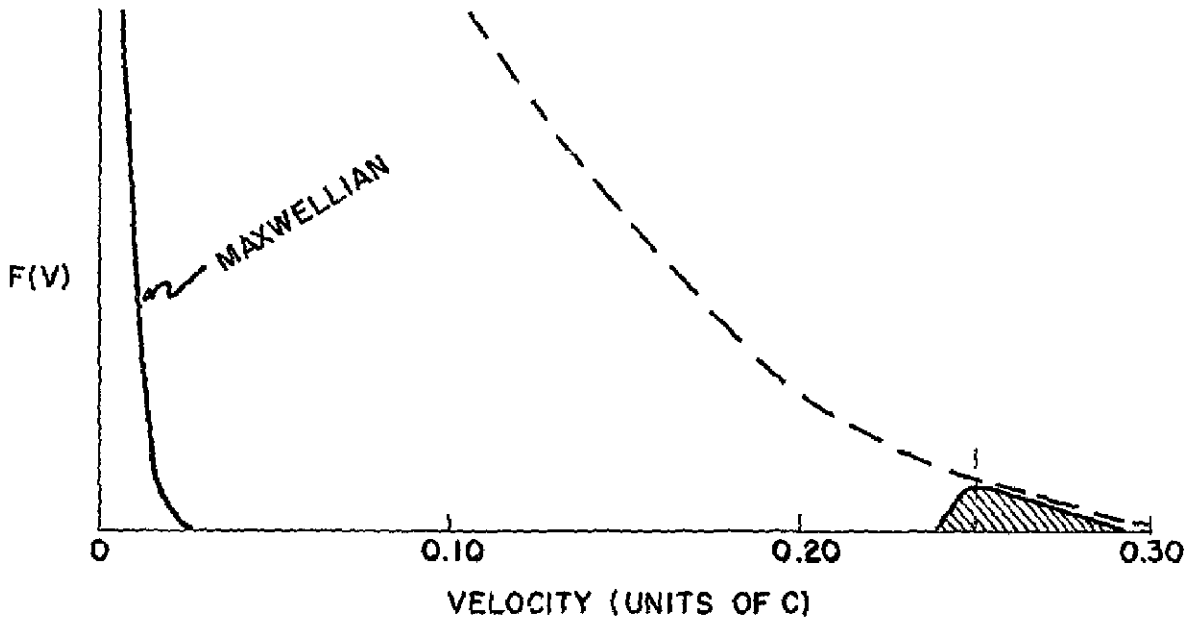

Figure 20 Velocity Distribution of Electrons in a Coronal Emitting Region I. The solid curve shows the local distribution for $T = 7 \times 10^5$ °K, and the hatched part shows a damped Maxwellian hump of fast electrons at 0. 25 c

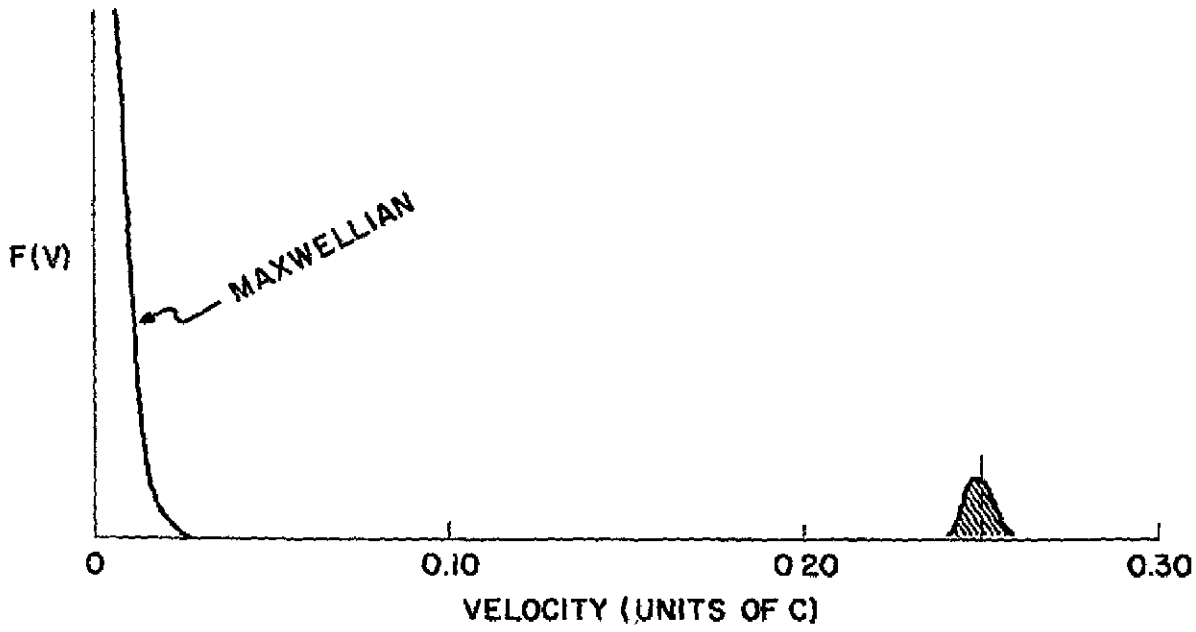

Figure 21 Velocity Distribution of Electrons in a Coronal Emitting Region II. The solid curve shows the local distribution for $T = 7 \times 10^5\ ^{\circ}K$, and the hatched part shows a gaussian distribution of fast electrons at 0 25 c.

electrical interactions between the ions and electrons, the highly ionized gas demonstrates ordered behavior in a variety of forms. These are essentially the result of the tendency of the plasma to remain force-free and electrically neutral (Bohm and Gross, 1949a) The introduction of an electric field will cause the plasma to respond in fixed modes which are dictated by its electrical properties. For the general case in which a magnetic field is present, plasma wave growth encounters a resonance at the upper hybrid frequency (see, for example, Bekefi, 1966), defined by

$$\omega_o = \sqrt{\omega_p^2 + \omega_b^2} \qquad \text{(V-1)}$$

where $\omega_1 = 2\pi f_1$ f_p and f_b are the electron plasma frequency and the gyro frequency, respectively, defined by

$$f_p = \sqrt{\frac{N_e e^2}{m\epsilon_o}} = 0.00898\sqrt{N_e}\ \text{MHz} \qquad \text{(V-2)}$$

and

$$f_b = \frac{eH}{m} = 2.799H\ \text{MHz}, \qquad \text{(V-3)}$$

where e, m = electron charge and mass

N_e = electron density, cm^{-3}

H = magnetic field strength, gauss

ϵ_o = permittivity of free space

The limited experimental data on magnetic field strengths in the far corona has been discussed in Chapter IV. In addition, Billings (1965) has used IMP-1 data to substantiate an r^{-2} decrease of the general solar magnetic field. Such a decrease results in a field strength of the order of 0.1 gauss at 5 5 $R_\odot$. Reference to equation (V-1) shows that the resulting gyro frequency is negligible compared with the plasma frequency, and that the equation reduces to

$$[\omega_o = \omega_p]_{H \approx 0} . \qquad (V-4)$$

The analysis presented here will assume the validity of equation (V-4) in the vicinity of 5 5 $R_\odot$, although it must be pointed out that if the field strength in coronal streamers at these distances is actually of the order of one gauss or higher, a more general development is required The expanded development is certainly necessary in the inner corona, where sunspot magnetic fields of several thousand gauss are not uncommon.

The introduction of an electric field into an equilibrium plasma may be accomplished by the injection of a stream of electrons. The resulting plasma waves may grow or they may be damped, depending on the physical conditions of the plasma and on the properties of the injected electrons. In the absence of a magnetic field, the plasma waves are damped by particle collisions and by a collisionless process known as Landau damping The latter has not been conclusively explained, but it involves energy interchange between the wave and

the background plasma Landau damping affects the amplitude of the electric field carried by the electrons as

$$\frac{dE}{dt} \propto - \frac{df(V)}{dV} \quad , \qquad (V-5)$$

where the derivative is taken at the point $V=V_{phase}$ for the plasma wave (see, for example, Montgomery and Tidman, 1964) The energy interchange acts primarily at the expense of the lower velocity electrons in the stream Malville (1961) has pointed out that the result of this effect is to set a lower limit to the propagation velocity of suprathermal electrons through the coronal plasma. This lower limit is between 0 1 c and 0 2 c, depending on the local coronal temperature; these figures are supported by observations of the motion of disturbances through the corona

The theory of collisional damping of plasma waves has been developed by Bohm and Gross (1949b) One of the results is that the time interval for the wave amplitude to fall to 1/e of its initial intensity is the mean time between particle collisions. The collision frequency φ is given by Jaeger and Westfold (1950) as

$$\varphi(T) \approx 42\, N_e\, T^{-3/2} \text{ sec}^{-1} \qquad (V-6)$$

Inverting and rearranging this equation, together with the use of equation (V-2), gives the relationship between plasma frequency, temperature and e-folding time which has been presented previously as equation (IV-1), p. 78.

Reference to equation (V-5) will show that if the derivative is positive rather than negative the wave will gain energy from the particles rather than lose energy through Landau damping. Injection of electrons with a velocity distribution satisfying this condition will result in rapid, unstable growth of the plasma wave. This mechanism is known as two-stream instability and has frequently been invoked to explain the observed magnitude of solar burst radiation (Malville, 1961; Kundu, 1965 and others) Whether two-stream instability is of consequence is an open question, since Sturrock (1964) has argued that such an instability would be damped out in an extremely short distance. In any case, the presence or absence of plasma waves in a medium does not depend on the presence or absence of instabilities

D. The Production of Electromagnetic Radiation

The production of electromagnetic radiation by fast electron streams under the conditions where there is no refractive index resonance and where the ratio of the gyro frequency to the plasma frequency is much less than unity requires the conversion of plasma wave energy into electromagnetic wave energy To conform with observational evidence, this conversion should produce resonance peaks at the local plasma frequency and at twice the local plasma frequency, and essentially no radiation at other points of the electromagnetic spectrum

Two mechanisms for energy conversion of this sort have been proposed The first mechanism (Ginzburg and Zheleznıakov, 1958, 1959a) utilizes scattering from electron density clumps to produce emission at the plasma frequency The second mechanism (Tidman and Dupree, 1965, and Bekefi, 1966) invokes enhanced bremsstrahlung as the plasma frequency mechanism' Both produce the second harmonic by a process known as combination scattering in which two plasma waves collide, producing radiation at the sum of the frequencies of the two waves

In this paper the normalized profiles of the bursts rather than their absolute emission levels will be examined It is therefore not necessary to consider any constant coefficients in the theoretical intensity equations such as the plasma wave to electromagnetic wave coupling efficiency The primary way in which the variable parameters enter the intensity equations is through the value of the velocities in the suprathermal electron stream. The manner in which the velocity function is used in the coupling models from which computations are made is described later in this chapter

E Predicted Radio Burst Profiles at 3. 5 MHz

1 The Form of the Observed Radiation

Prediction of the form of the solar burst profiles which are observed must be based on the somewhat scanty information discussed thus far. Two points are particularly relevant The first is that all

theoretical work to date indicates the very high probability of radiation at the local plasma frequency (and at twice that frequency) for bursts originating in the far corona. The second is that the mechanisms invoked require a stream of suprathermal electrons with a velocity distribution similar to one of those shown in Figures 20 and 21 In the idealized case, a packet of appropriate suprathermal electrons would propagate through a region small enough so that the temperature and density may be regarded as constant, instantaneously exciting radiation with a fixed spectrum. This radiation would be detected by a receiver of very narrow bandwidth, tuned sharply to the plasma frequency of the region The flux density of the radiation would decline as the plasma waves were damped, in accordance with the precisely known ambient temperature of the region.

In practice, the situation is quite different for several reasons First, there is a substantial spatial diffusion of the suprathermal electrons, particularly in the far corona This will be demonstrated by a rise to maximum which is not the delta-function type previously described Second, since the electron density gradient is very small, reception of radiation from a region of considerable spatial extent is implied In addition, the emission, while peaked at the plasma frequency, has a finite bandwidth Finally, the values of the coronal temperatures are not well determined and in any case the value selected will be at best an average over the extended emission region.

While recognizing the problems listed above, it is nevertheless of interest to examine closely the total process with the aim of producing quantitative predictions of solar radio emission. This is done on the following pages

2. Mathematical Model for Solar Burst Emission

The factors which have been discussed this far suggest the general form of the relationship for the observed flux density as a function of frequency and time. In the most general case this proportionality may be written, for frequency f_c and a receiver with passband Δf, as

$$S(t) \propto \int_{\tau=0}^{\tau=t} \{ \int_{f=f_c-\frac{1}{2}\Delta f}^{f=f_c+\frac{1}{2}\Delta f} [\int_{V=-\infty}^{V=+\infty} S[f, F(V)] \, T[F(V)] \, dV] \, df \} \, N(\tau) \, e^{-\varphi(T)[t-\tau]} \, d\tau \qquad (V-7)$$

where the terms are defined as follows:

$S(t)$ = observed flux density as a function of time at a given frequency f_c for a receiver with passband Δf.

$S[f, F(V)]$ = instantaneous plasma wave energy spectrum as a function of frequency and of the velocity distribution of the suprathermal electrons.

$T[F(V)]$ = transfer function specifying the efficiency of conversion of plasma wave energy to electromagnetic energy, as a function of the suprathermal electron velocity distribution.

$N(\gamma)$ = number of suprathermal electrons injected per unit time through a unit cross-sectional area of the plasma level under study. This parameter, together with the plasma emission spectrum, specifies the volume of the emitting region.

$e^{-\varphi(T)[t-\tau]}$ = the collisional damping factor for the plasma waves The use of the damping factor in this way implies that no other damping mechanism is significant, and hence is restricitve in application. The collisional frequency φ is dependent on the ambient electron temperature and hence on the coronal temperature model.

The proportionality sign is used because numerical coefficients have not been included, and since it is the intent of this paper to normalize all theoretical profiles to facilitate comparison.

It is pertinent to discuss the manner in which the variable quantities prescribing the solar radio emission enter into equation (V-7). The bandwidth of the receiver is of consequence only for the limits of the frequency integration. The integration over time is

necessary because electron injection into the plasma occurs over a finite period of time and because the emission originates in regions in which the plasma electron density, temperature, etc are not the same. The result is that the traveling electron stream successively excites regions with different properties Time t = 0 specifies the time of initial electron injection into a region in which S [f, F(V)] has a non-negligible value within the frequency interval $f_c \pm 1/2\ \Delta f$ of the receiver. The integration over the electron velocity spectrum includes both the local plasma electrons and those of the suprathermal electron stream

The four factors of equation (V-7) are all model dependent. $N[V, \tau]$ is prescribed by both the theories of initial electron acceleration and of damping and spatial dispersion from the point of origin to where the electron density is appropriate for emission in the frequency band of the receiver The emission spectrum and the transfer function as a function of suprathermal electron velocity are given by theories which predict the characteristics of electromagnetic wave emission from a plasma into which a beam of suprathermal electrons is injected Finally, the damping factor is dependent on the invoked damping mechanism, and on the value chosen for the ambient coronal temperature.

3. Electron Injection Model

An accurate specification of the parameter $N(\tau)$ requires detailed knowledge of the process of electron injection at the base of

the corona and of the changes in the velocity and space distributions of the electrons as a result of their passage along a designated coronal path. The injection process is unknown, as is the time scale of the electron injection. It is obvious, however, that a packet of electrons with a significant velocity dispersion will develop a spatial dispersion which will increase with time. In such a dispersion the higher energy electrons will be at the leading edge of its spatial extent, with successively lower energy electrons in the spatial regions closer to the source. In addition, the spatial extent of the electrons may be limited at the low-energy end by Landau damping and by collisional damping, primarily at the expense of the low-energy electrons.

The parameter required from an electron injection model is the number of suprathermal electrons which enter a specified volume of coronal plasma at the 3.5 MHz level (i.e., the surface of constant $R/R_\odot$ for which $f_p = 3.5$ MHz), as a function of velocity and time. Weiss and Wild (1964) have studied the propagation of electrons injected along a magnetically neutral plane near the chromosphere/corona interface. Their model utilizes a magnetic field with vertical field gradient $\exp(-5R/R_\odot)$ and isotropic injection over the vertical hemisphere at $R/R_\odot = 1$. Several distributions of electron velocity and injection time are proposed. The resulting electron flow for a quasi-Maxwellian velocity injection [$F(V) = \exp\{-168\,(0.44V - 1/6)^2\}$, where V is in units of solar radii per second] appears to meet the general requirements which have been specified in this paper. Their

model is therefore chosen as a trial electron injection model for low-frequency burst profile computations performed here. Predicted distributions are given for coronal heights which correspond "approximately" to the 50 MHz and 20 MHz surfaces Because of the uncertainties involved, both of these distributions are used for the computations described herein, as are two distributions developed by the author of this paper These distributions $N(\gamma)$ are shown in Figure 22, with the maximum normalized in each case The total electron population of the volume of plasma in question is the sum of $N(\gamma)$ and the local Maxwellian distribution. In the figure, (A) represents an extrapolation of the Weiss-Wild 20 MHz model to the approximate region of the 3.5 MHz surface Distributions (B) and (C) are the Weiss-Wild models for the 50 MHz and 20 Mhz surfaces, respectively Distribution (D) has been developed for this paper to study the effect produced by a much shorter injection time scale than those predicted by the other distributions These distribution functions are designated hereafter as G1, WW1, WW2, and G2. The injected electrons which are represented are suprathermal; an ambient Maxwellian distribution of electrons is also present in the region of plasma under consideration

Figure 22 Temporal Electron Distributions for Different Electron Injection Models.

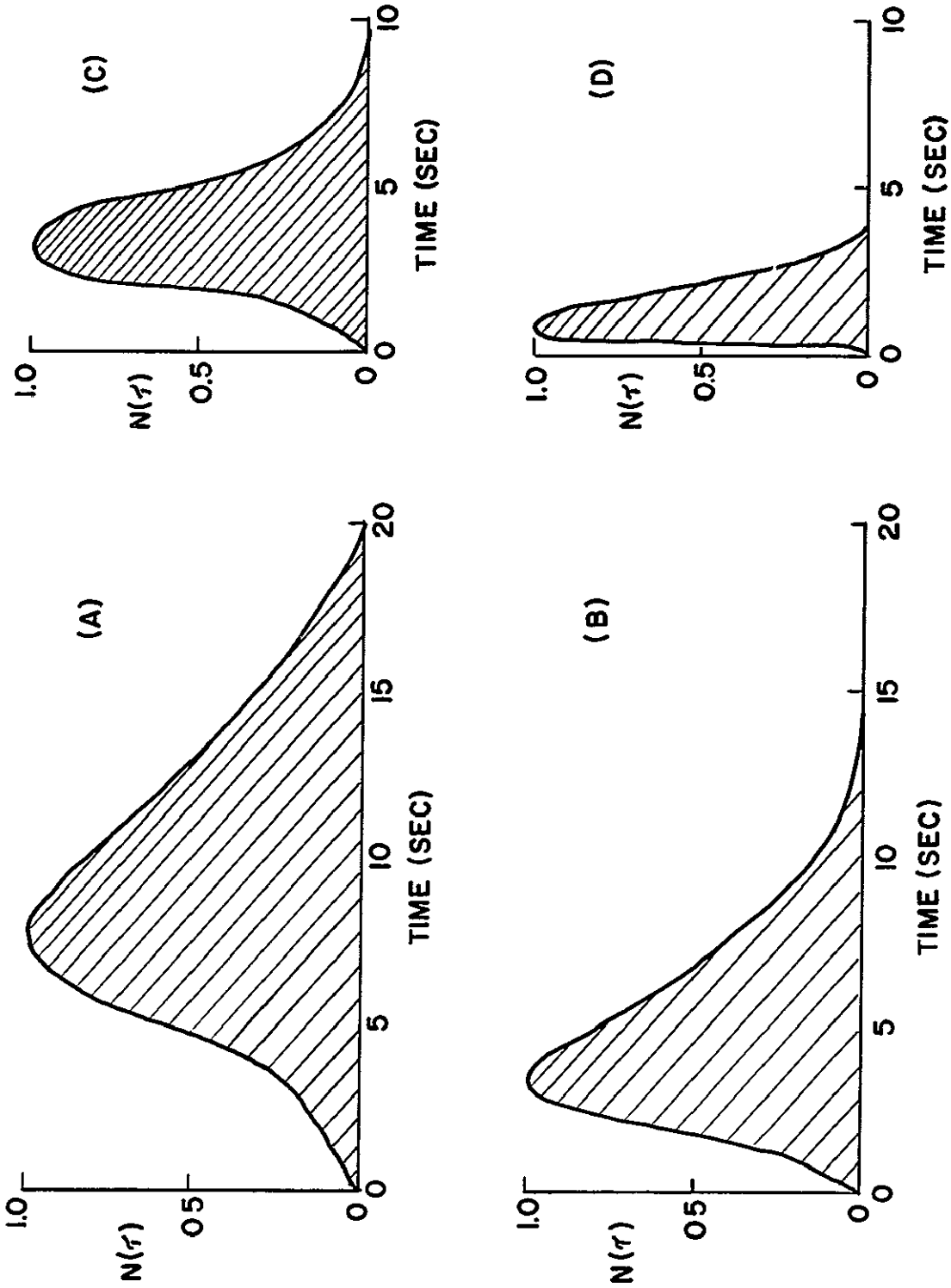

4 Plasma Wave Emission Spectrum

No theoretical studies have produced accurate spectral predictions, although recent progress suggests that such predictions may soon be made Enhanced radiation at f_p and $2f_p$ is commonly observed, although the enhancement mechanism is at issue For purposes of discussion some of the features of the methods proposed can be used to predict the observed spectrum In particular, Tidman and Dupree (1965) have shown that suprathermal electrons can produce enhanced emission at f_p and $2f_p$ if they are in the high energy tail of the ambient Maxwellian distribution of velocities. This condition is satisfied for all electrons which have not been damped in the inner corona The strength of emission, however, is subject to the following proportionality·

$$T[F(V)] \propto V_s^{-1} \exp V_s^2$$

where

$$V_s = \frac{kT_s}{m}$$

and the T_s refers to the kinetic temperature of the suprathermal electron stream

The second plasma wave emission model which is considered is that of Ginzberg and Zheleznıakov (1958, 1959a, b) Their treatment predicts that

$$T[F(V)] \propto V_s^9 .$$

In view of the considerable uncertainty about the generally accepted coupling mechanisms, burst profile computation is also performed in this paper using an emission intensity model similar to that suggested by Weiss and Wild (1964). In this model the emission intensity is proportional to the suprathermal velocity as

$$T[F(V)] \propto \exp V_s$$

The great differences between these predictions should make it possible to use the electron injection spectrum to produce at least a qualitative statement of the agreement between theory and observation. Consider the observed radiation for two time periods of a radio burst The emission of radiation in the first period is caused by suprathermal electrons of velocity $V_s = 0\ 32\ c$ and that in the second period by electrons of velocity $V_s = 0.16\ c$ The difference in observed intensity predicted by Tidman and Dupree's theory is

$$\frac{T[F(V)](0\ 32\ c)}{T[F(V)](0\ 16\ c)} = \frac{\exp(0\ 32\ c)^2\ (0.16\ c)}{\exp(0\ 16\ c)^2\ (0\ 32\ c)} \approx 10$$

while the difference predicted by Ginzberg and Zheleznıakov is

$$\frac{T[F(V)](0\ 32\ c)}{T[F(V)](0.16\ c)} = \frac{(0\ 32\ c)^9}{(0\ 16\ c)^9} \approx 500$$

and that of Weiss and Wild is

$$\frac{T[F(V)](0.32\ c)}{T[F(V)](0.16\ c)} = \frac{\exp(0\ 32\ c)}{\exp(0.16\ c)} \approx 1\ 1\ .$$

The three coupling models between plasma waves generated by the suprathermal electron stream and the resulting electromagnetic radiation will be designated henceforth as TD (Tidman-Dupree), GZ (Ginzberg-Zhelezniakov), and WW (Weiss-Wild)

The bandwidth and shape of the emission peak at f_p are also of substantial interest The ambient parameters of the coronal plasma are so poorly known, however, that, except for a prediction of a "sharp" peak, no spectral information can be obtained from any of the coupling models. The emission peak bandwidth is therefore essentially a free parameter This bandwidth is one of those quantities which has been varied within reasonable limits to predict the emission profiles

5. Collisional Damping of Plasma Waves

It has been previously noted that plasma waves are collisionally damped as $\exp[-\varphi(T)t]$ where $\varphi(T)$ is given by equation (V-6) In order to include damping in the burst profile model it is necessary to adopt provisionally a model for the coronal temperature gradient as a function of distance For the purpose of comparison with observations, three temperature models will be used. One is the model of Whang, Liu, and Chang (1966), based on a theoretical solar wind study The other two result from comparisons of burst observations with assumed

coronal density models; they are those of Hartz (1964) and Hartz and Warwick (1966). The collisional frequencies given by the three models at the 3 5 MHz level are listed in Table 9 These models are referred to hereafter as W, H, and HW, respectively.

Model	Temperature at 5 5 $R_\odot$	$\varphi(T)$	$e^{-[\varphi(T)t]}$
Whang, Liu, and Change (1966)	7×10^5 °K	0.010	$e^{-0\ 010t}$
Hartz (1964)	6×10^5 °K	0 013	$e^{-0\ 013t}$
Hartz and Warwick (1966)	4×10^5 °K	0 021	$e^{-0.021t}$

Table 9 Coronal Collisional Frequencies at 3 5 MHz for Three Coronal Temperature Models

6 Theoretical Solar Burst Profiles

The computation of theoretical burst profiles follows directly from equation (V-7), with the factors of the equation being specified from the models described on the previous pages The OGO-III pass-band is restricted to a very small range of frequencies This suggests that predicted profiles at the extremes of the frequency range will differ very little For this reason, the profiles computed here are restricted to f = 3 5 MHz

The practical consequence of the gradual temperature gradient in the far corona is that collisional damping is essentially uniform over large coronal path lengths To simplify computation the damping parameter $\varphi(T)$ may be regarded as a constant for a low-frequency

burst at 3.5 MHz. This assumption implies that the principal contribution to the flux density at one frequency is produced in a region in which the electron temperature is essentially constant. The data averaging process in the OGO-III analysis produces burst profiles for a bandwidth of $\Delta f = 100$ kHz For this reason, the computations here are restricted to the receiver frequency band $f = 3.5 \pm 0.05$ MHz.

A final assumption is that emission at the plasma frequency takes the following form:

$$S\{f, F(V)\} = 1 \text{ for } f_p - \frac{1}{2}\Delta f_p \leq f \leq f_p + \frac{1}{2}\Delta f_p$$

$$= 0 \text{ elsewhere} \qquad \text{(V-8)}$$

where Δf_p is the bandwidth of the emission centered on the plasma frequency. This assumption is plausible in view of the plasma wave spectral intensity profiles computed by Tidman and Dupree (1965) and the identification of the emission as a sharp resonance phenomenon

It is now possible to integrate equation (V-7), using the discussion above to specify the factors contained within the equation.

The numerical integration is performed by choosing an electron injection model for $N(\tau)$, using one of the three wave-coupling transfer functions $T[F(V)]$, selecting a collisional frequency by choosing one of the three coronal models, and designating emission bandwidth for the solar radio burst by equation (V-8) It is assumed that the higher velocity electrons are moving at 0.25 c (Stone, et al., 1967)

The schematic development of a solar radio burst is illustrated in Figure 23 for an emission bandwidth of 2 MHz. The receiver passband is assumed to be very narrow compared to the emission bandwidth; for OGO-III the receiver passband is 20 kHz The solar burst profile resulting from this development will be designated Burst Model Number 1 Its model characteristics, along with those of other burst models to be discussed, are listed in Table 10 At time $t = 0$ the leading edge of the suprathermal electron packet arrives at the f_p = 4 5 MHz level, producing the emission shown (The electromagnetic emission is taken to be essentially simultaneous with the passage of the suprathermal electrons) As the electron packet continues through the coronal plasma radiation with the emission spectra shown in Figure 23 is successively excited at higher coronal levels In the actual case, of course, a continuous series of emission spectra is produced, rather than just the five spectra shown here

Emission from any one coronal level as a function of time depends on the temporal electron injection spectrum and on the damping of the plasma oscillations. This model uses the WW1 injection spectrum, which has a duration of about 13 seconds (Figure 22b). When this spectrum is convolved with the collisional damping factor, the result is the solar burst profile at one coronal level. For Model 1 these profiles are shown as the smaller curves in Figure 24 Superposition of each profile contributing to the radiation in the receiver

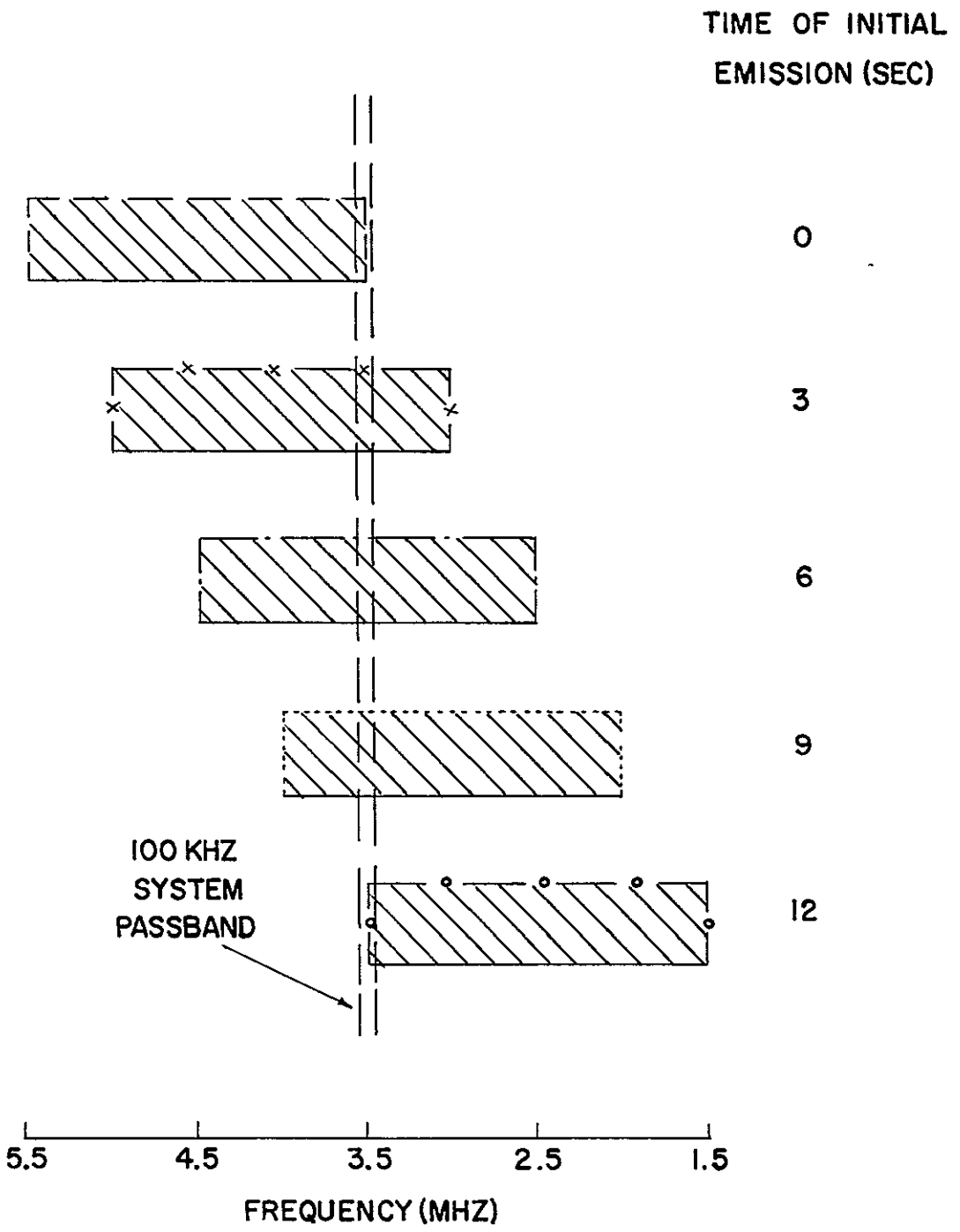

Figure 23 Schematic Development of a Low-Frequency Solar Radio Burst.

Burst Model Number	Electron Injection Model					Wave Coupling Model			Coronal Temperature Model			Emission Bandwidth kHz
	WW1	WW2	G1	G2	G3	TD	GZ	WW	HW	H	W	
1	x					x			x	(Varying with R/R_O)		2000
2	x					x			x			200
3	x					x			x			400
5	x					x			x	x		800
6	x					x					x	400
7	x							x	x			400
8	x						x		x			400
9		x				x			x			400
10			x			x			x			400
11				x		x			x			400
12					x	x			x			400

Table 10. Specification of Variables For Theoretical Solar Radio Burst Profile Computations.

passband produces the total burst profile, which is the solid curve in Figure 24

The minor variations in the individual burst profiles in Figure 24 are due to the slightly different damping constant extant in the coronal levels from which the emission originates. In the remaining burst models described in this chapter, the temperature variation has been neglected. That this is justified in light of observations is shown in Chapter VI

With the schematic picture of solar radio burst production at hand, it is of interest to investigate the effect of varying each of the available parameters. Figure 25 shows the result of increasing the bandwidth of the emission centered on the plasma frequency. The temperature model, wave-coupling model and electron injection model are the same for all three profiles. It is readily apparent that increasing the bandwidth modifies the slope of the rising portion of the profile but has little effect on the declining portion This is because the rising portion is sensitive to the electron travel time through the region of emission. As the emission bandwidth is increased the emission region is enlarged, hence travel time increases and the leading edge of the burst profile is modified. The declining portion of the profile is controlled largely by collisional damping and thus shows little change as a function of bandwidth; note that this would not be the case if significantly different temperatures were involved

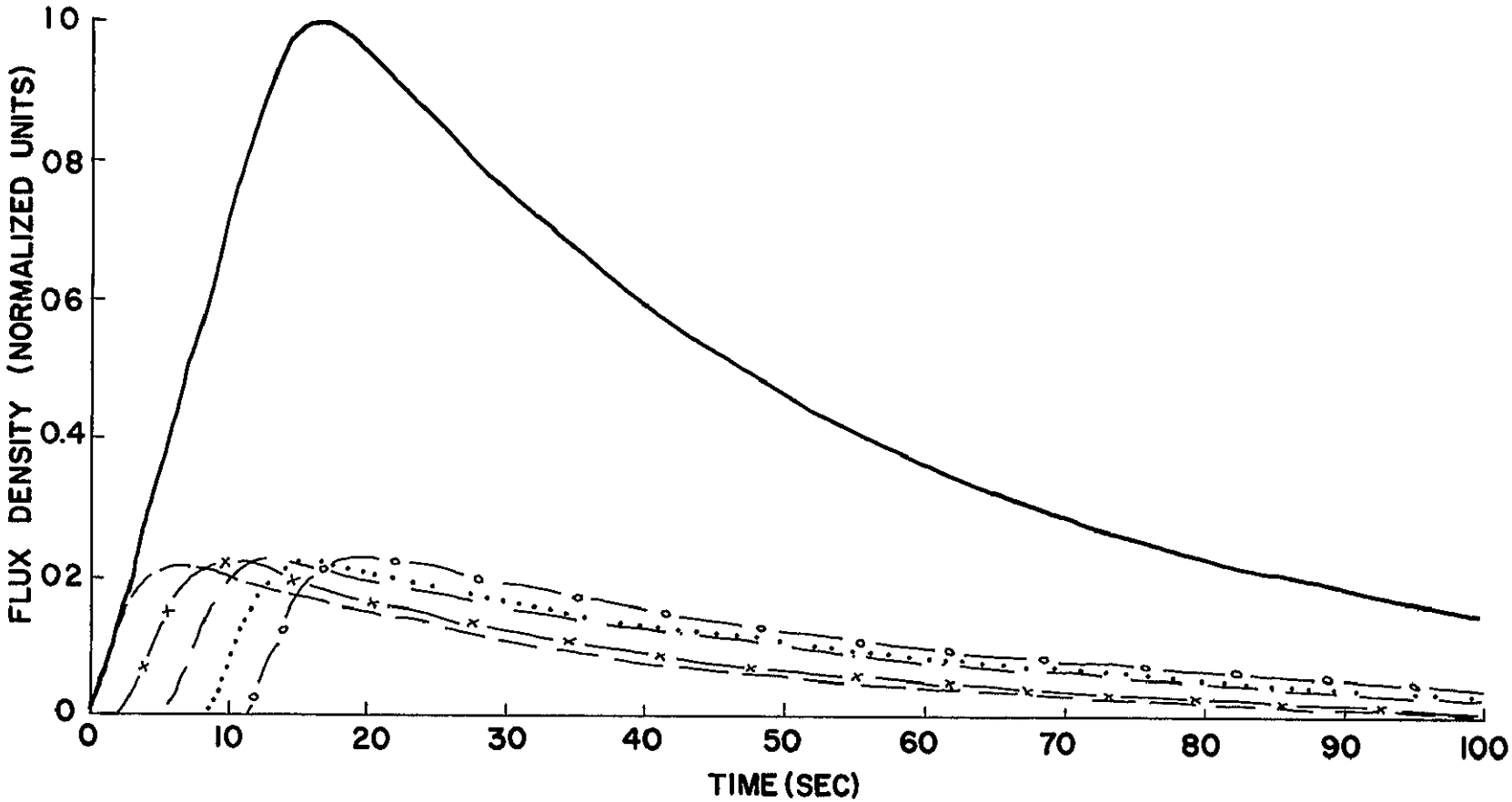

Figure 24. Schematic Development of a Solar Radio Burst Profile.

Figure 25. Theoretical Radio Burst Profiles for Different Emission Bandwidth About f_p

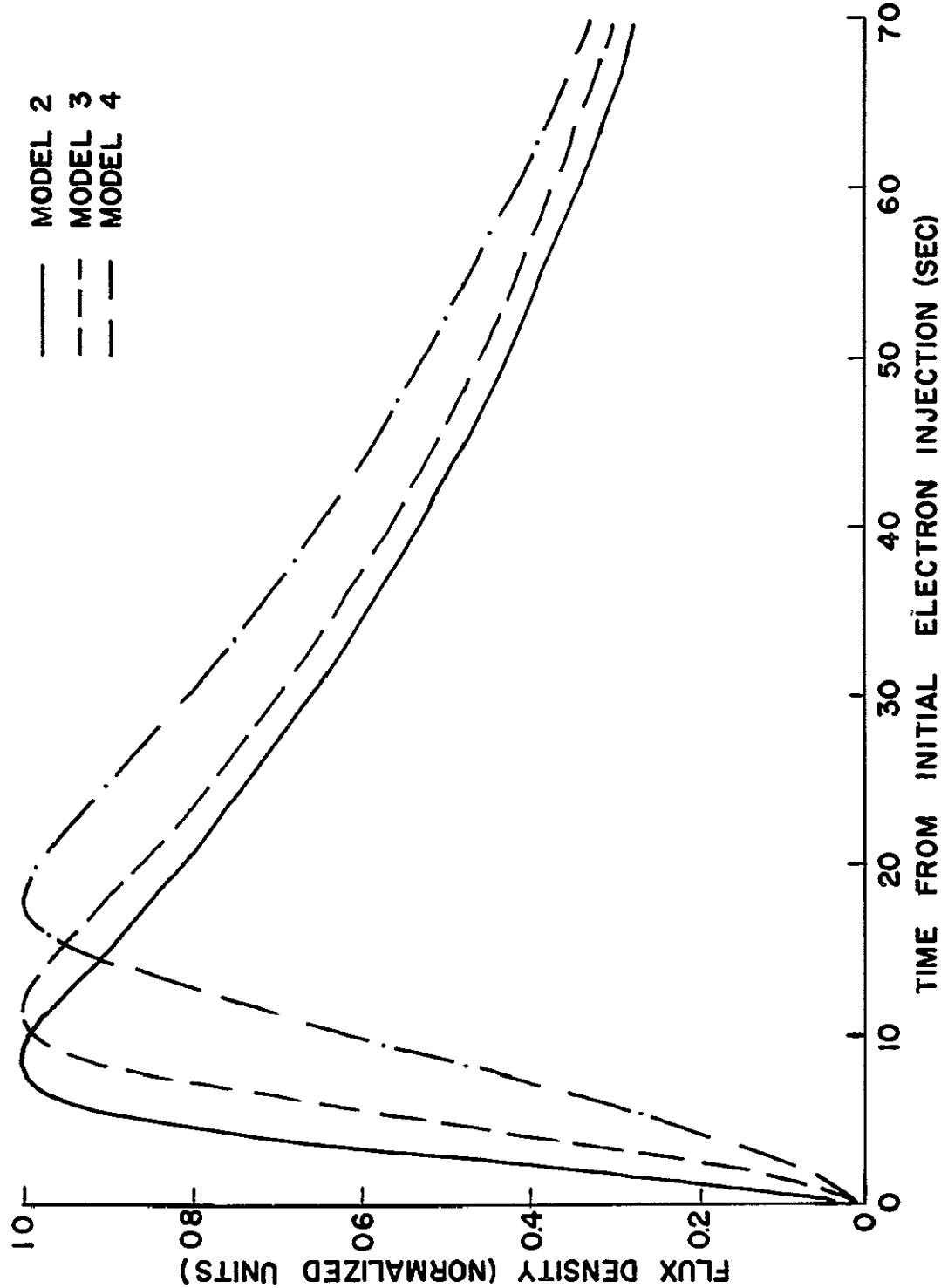

Figure 26 demonstrates the solar burst profiles resulting when different coronal temperature models are invoked. As anticipated, a marked difference is present among the resulting profiles, particularly in the declining portions of the curves

More surprising is the comparison among the profiles resulting from the various wave-coupling models These are shown in Figure 27, and are seen to resemble each other very closely, despite the very great difference in emission intensity dependence as a function of suprathermal electron velocity predicted by the different models. It must be pointed out here that this comparison is between normalized profiles The method of profile computation used does not provide absolute flux density values; such values would be strongly model dependent Without information concerning the electron flux in the high-energy stream, however, no absolute emission predictions can be made The relevant comparison of theory with observation is thus the normalized variation of flux density with time.

Figure 28 shows the effect produced on the burst profile by varying the time scale of the electron injection The result is that increasing the injection time scale broadens the peak of the curve without having much effect on the declining slope The change produced on the rising slope is insignificant compared to that produced by changes in bandwidth The shape of the injection function N(t) also has an effect on the burst profile In Figure 29, (a) is a reproduction of Figure 22 (a), and (b) shows N(t) for distribution G3.

Figure 26. Theoretical Radio Burst Profiles for Different Coronal Temperature Models

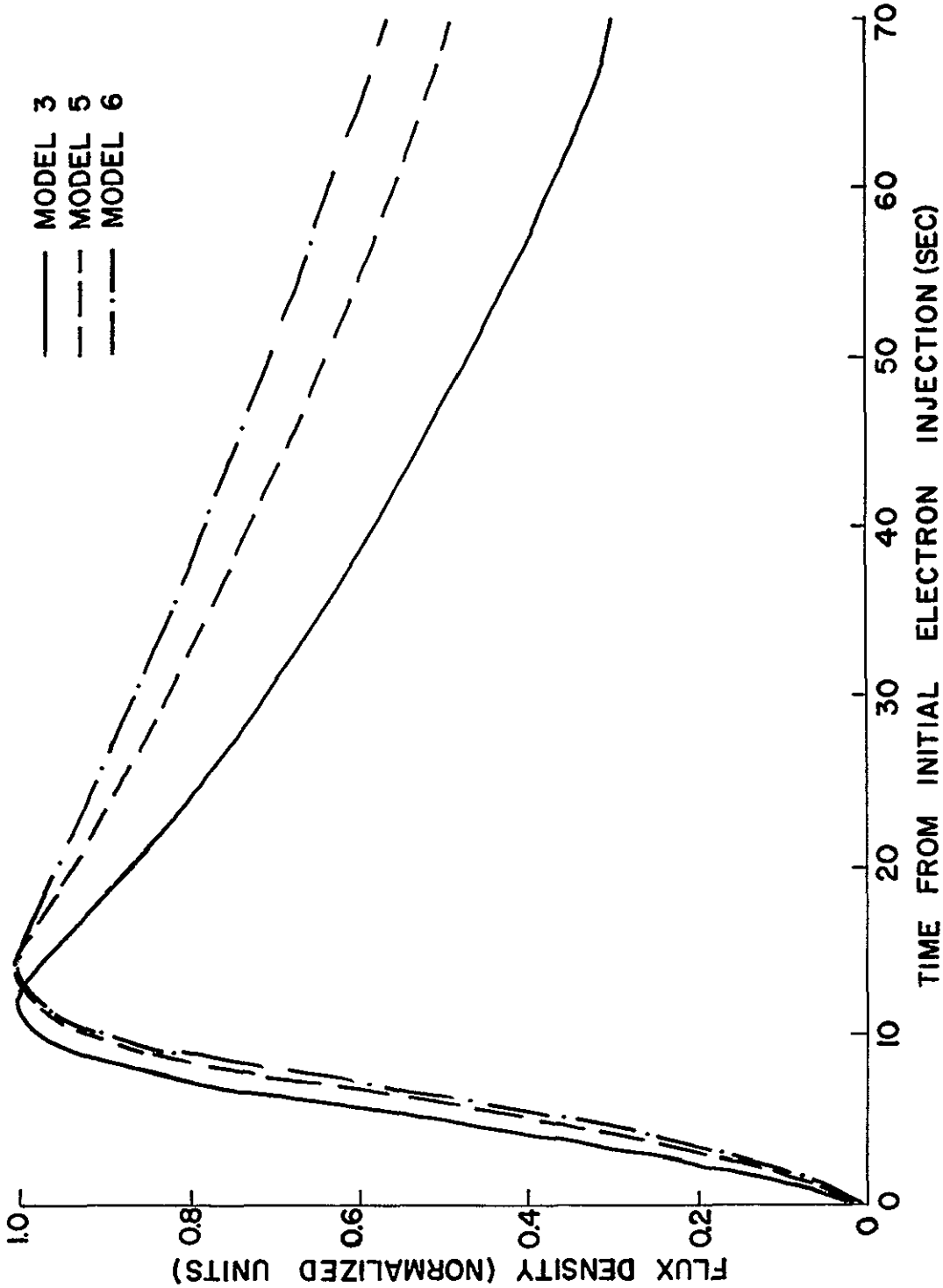

Figure 27 Theoretical Radio Burst Profiles for Different Plasma-EM Wave Coupling Models

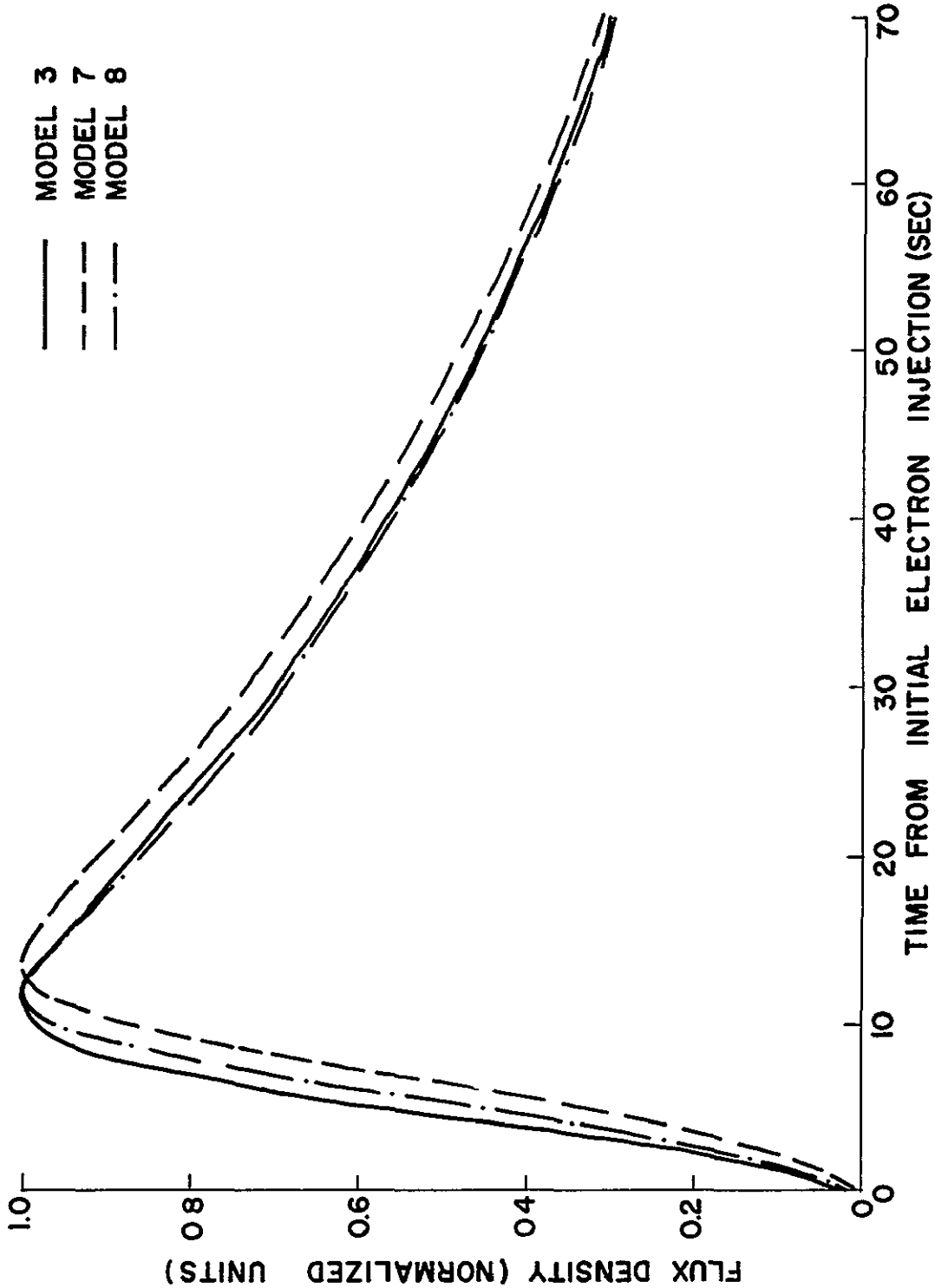

Figure 28. Theoretical Radio Burst Profiles for Different Electron Injection Models.

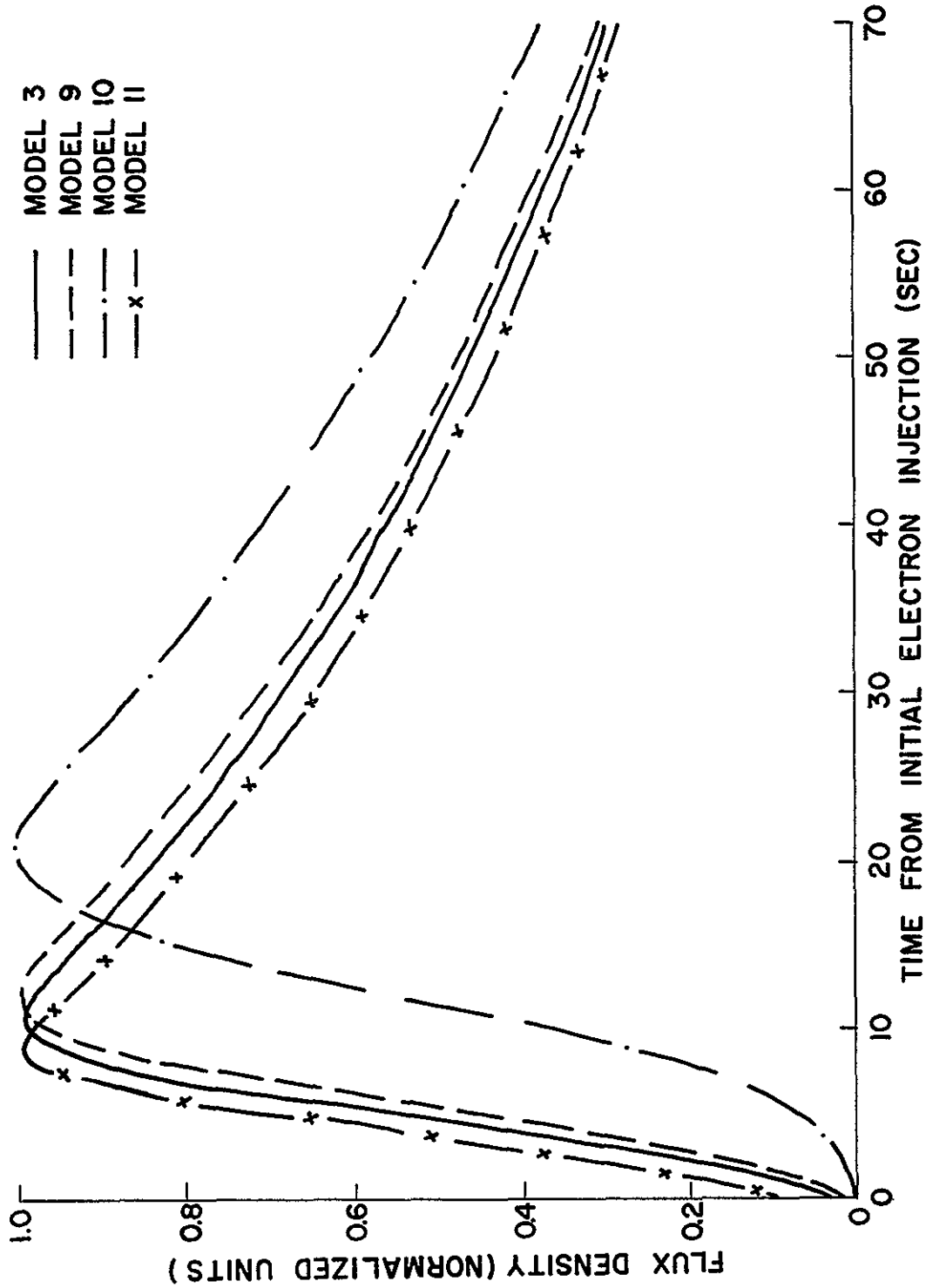

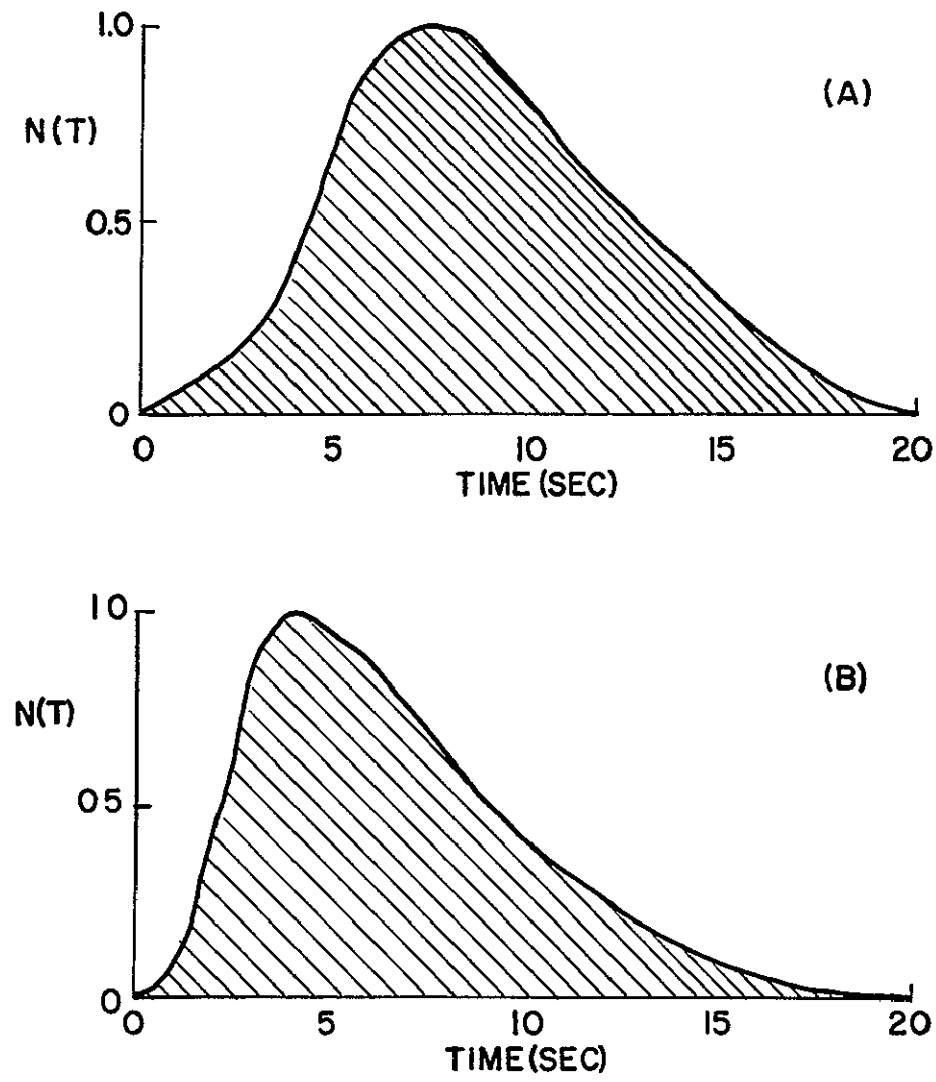

Figure 29 Temporal Electron Distributions with Different Shape but of Equal Duration

This distribution has the same time duration as G1, but has its maximum at a time similar to the WW models. The resulting burst profiles are shown in Figure 30 It is seen that changing the shape of the injection spectrum changes the rise time to maximum, but has only a small effect on the burst profile.

The computed parameters for the twelve solar burst profiles depicted in this chapter are listed in Table 11 These figures may be used as starting points in the task of fitting the theory developed here to the observational data from OGO-III

To summarize, even though all points of a solar burst profile are determined to some extent by each of the variables of equation (V-7), the dependence of the profile on each individual variable changes throughout the curve, as follows:

(i) The leading edge of the profile is strongly dependent on the bandwidth of the emission centered on the plasma frequency To a lesser extent, it is dependent on the time span of the electron injection.

(ii) The change of curvature in the profile in the vicinity of the maximum point is strongly controlled by the time span of the electron injection

(iii) The trailing edge of the profile is strongly controlled by the coronal temperature in the emitting region.

Figure 30 Theoretical Radio Burst Profiles for Differently Shaped Electron Injection Models.

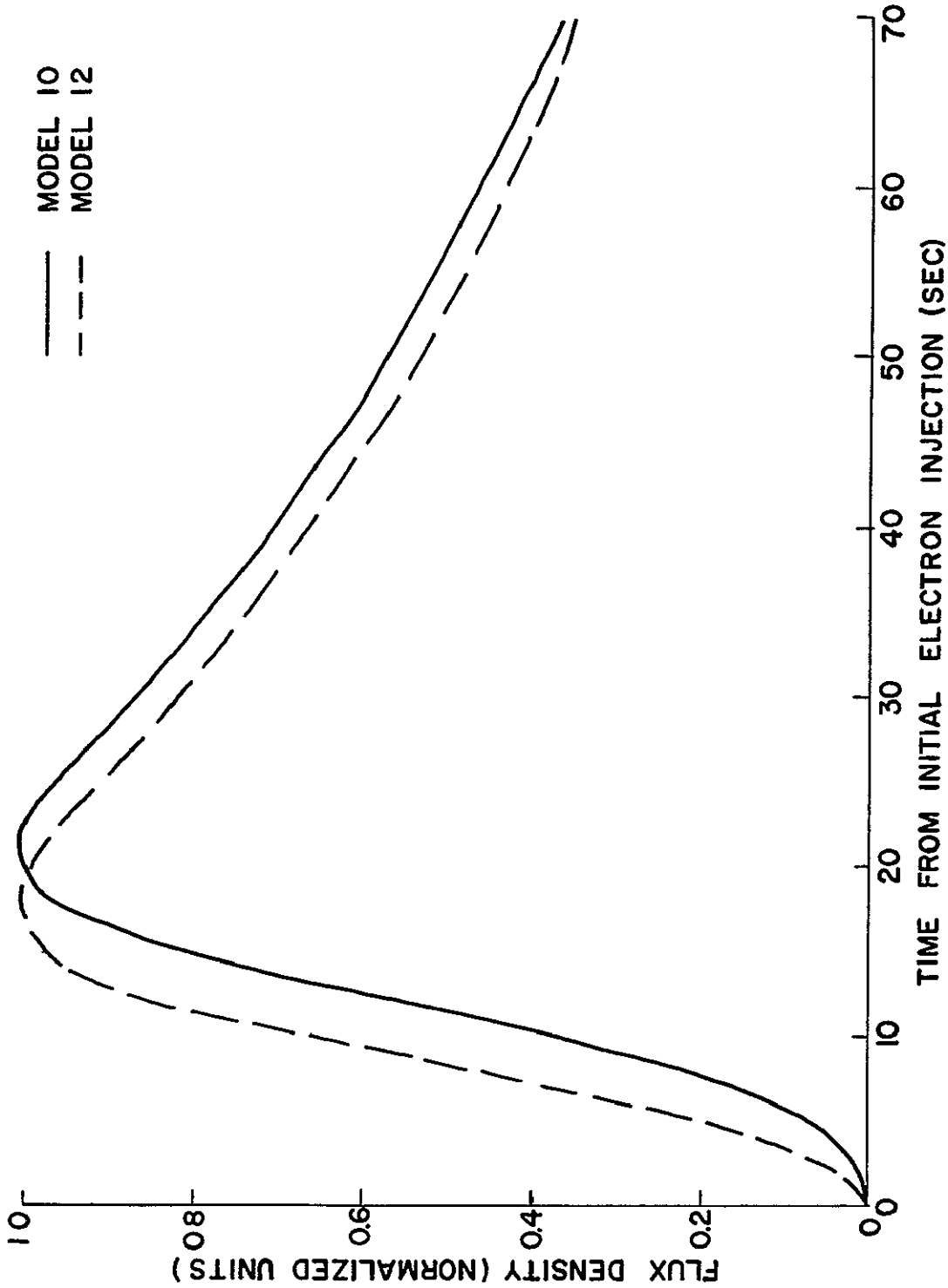

Burst Model Number	Rise Time to Maximum (sec)	e-folding Time (sec)	$(A/B)_{1/e}$ [7]
1	17.0	55 5	0.79
2	8.8	60 0	0.89
3	11.4	61.5	0.87
4	18 0	62 8	0 81
5	14 0	89.4	0 90
6	14.2	100 1	0.91
7	13.9	62.4	0.86
8	11 8	60 5	0 87
9	12 1	61 2	0.88
10	20 8	61.1	0.82
11	9 0	58 4	0 88
12	18 0	61.0	0 82

Table 11 Theoretical Solar Radio Burst Profile Parameters

[7] These parameters are defined by Figure 15.

(iv) The wave coupling model involved has very little effect on the solar radio burst profile.

A final remark is in order concerning the comparison. If several radio bursts are seen within a fairly short time period (of the order of a few hours) and are determined to have originated in the same coronal streamer, no significant temperature change is likely to have taken place and the same coronal temperature model should hold for all the bursts The method of coupling the electron stream into electromagnetic radiation must be the same for all the bursts, as must the form of the emitted spectrum It appears reasonable, therefore, to attribute differences between the observed profiles to differences in the velocity and time injection of the suprathermal electrons In this way it may be possible to deduce the properties of the electron streams from the observed solar radio burst profiles.

CHAPTER VI

DISCUSSION OF RESULTS

A. Correlation With Radio Spectral Observations

1 Event Correlation

The reception pattern for the OGO-III antenna closely approximates that of a Hertzian dipole, rather than being directional In order to establish whether or not a signal enhancement was truly solar in origin it was advisable, particularly in initial data evaluation, to correlate tentative low-frequency burst events with higher frequency events observed by ground-based stations. The ground-based instruments have the advantages that their antenna patterns are centered on the solar disk and are at least moderately sharp, and that their equipment response can be actively monitored.

Since the OGO-III radiometer is a sweep frequency instrument, it was anticipated that the correlation of OGO-III events with ground-based sweep frequency radio events would produce a high incidence of coincident burst detection The correlation is, in fact, very good. Of the 164 OGO-III events for which concurrent ground-based observations were made, 157 were confirmed as being of solar origin, a correlation of 95 8% The seven unconfirmed events all occurred between 0000 and 0700 U T., during which time only the Culgoora radio spectrometer was in operation. It seems likely, therefore, that

event correlation is limited by either incomplete event reporting or the Culgoora station's having a lower sensitivity than other observatories operating radio spectrometers

An alternative correlation approach is to analyze the number of events for which the OGO-III experiment confirms a burst detected by ground-based equipment In order to perform this correlation, all Importance 3 fast drift bursts observed by the University of Colorado radio spectrometer at 41-7 6 MHz were listed OGO-III data for concurrent periods was then examined Of 399 UC events, only 82 were detected by OGO-III. This apparently results from the very high radio noise environment of the spacecraft, although it could also be caused by a great number of solar radio bursts having a low-frequency cutoff in the vicinity of 5 MHz Such a limit has been suggested by low-frequency ground-based observation, (see, for example, the burst events illustrated by Sheridan and Attwood, 1962) The high inverse correlation, however, suggests that all radio bursts which are strong emitters in the 4-2 MHz band are also strong emitters in the 50-5 MHz band commonly observed by ground-based stations

2. Relative Importance Ratings

A comparison of the qualitative importance ratings assigned to coincident bursts by high- and low-frequency observers makes it easier to understand the event occurrence correlations described above.

For comparative purposes the ratings of the University of Colorado radio spectrometer are used here The importance ratings assigned to the bursts observed with this instrument are (Solar Geo Data, 1968):

Imp. 1 : $5 - 20 \times 10^{-22}$ watt $m^{-2} Hz^{-1}$

Imp 2 . $20 - 80 \times 10^{-22}$ watt $m^{-2} Hz^{-1}$

Imp 3 : $>80 \times 10^{-22}$ watt $m^{-2} Hz^{-1}$

It has been stated in Chapter IV that typical OGO-III burst flux levels are 10^{-16} watts $m^{-2} Hz^{-1}$ Reports of radio burst events in the 120-70 MHz band indicate typical fluxes of 10^{-18} watt $m^{-2} Hz^{-1}$ (Wild, 1950) It is thus anticipated that the strong bursts detected by OGO-III will all receive high importance ratings by the University of Colorado in the 41-7 MHz band. Table 12 shows that this is indeed the case Of the 148 coincident events, 102 are rated Importance 3 by the University of Colorado The solar bursts reported monthly by Colorado are almost equally divided among the three importance categories The facts confirm the expectation that OGO-III detected only major events, and explain the failure of the OGO-III experiment to detect more than about 20% of the Colorado events Any statistical comparisons of these low-frequency results with those at higher frequencies must thus take into account the fact that OGO-III events are restricted to those of substantial flux density

To estimate whether the flux densities measured by OGO-III are consistent with those obtained at other frequencies, Wild's (1950) flux

University of Colorado Importance Rating (41-7 MHz)	OGO-III Importance Rating (4-2 MHz)		
	1	2	≥3
1	8	6	4
2	10	10	8
3	37	39	26

Table 12 Comparison of OGO-III and University of Colorado Importance Ratings for Solar Radio Bursts.

density values at 120-70 MHz may be used Over his limited frequency range, the average flux density as a function of frequency followed the proportionality $S_\nu \propto f^{-3.5}$ Figure 31 shows two of his data points and the position of the proportionality law which he derived, on a flux density-frequency graph Also shown in the average flux density measured by OGO-III for fast drift bursts at 3 5 MHz, together with the measured range of OGO-III flux densities The results indicate that Wild's proportionality is not valid at very low frequencies

B Correlation With Solar X-Ray Observations

Both thermal and nonthermal fluxes of solar X-rays are commonly seen The nonthermal bursts show a very high correlation with centimeter wave solar radio bursts (Kundu, 1963), but only about a 10% correlation with fast drift bursts in the 500-10 MHz range (de Jager, 1965) The accepted interpretation of these results has been outlined by Kundu (1965) and Goldberg (1967). Kundu's statement is as follows:

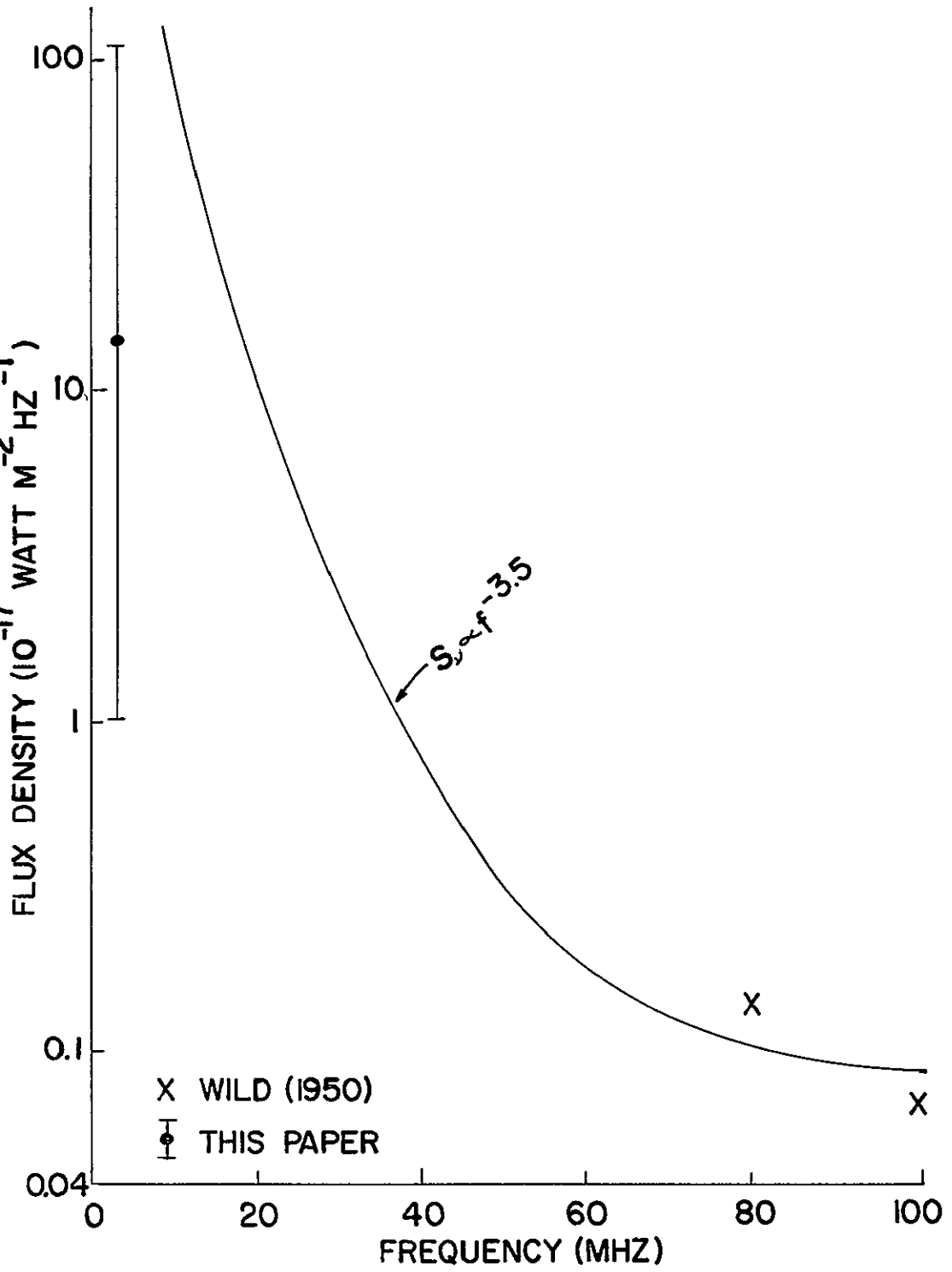

Figure 31 Average Solar Radio Burst Flux Density as a Function of Frequency

It appears that the energetic electrons (accelerated in the flare region) produce centimeter-wave bursts by synchrotron radiation and flow into the lower chromosphere, where they produce high-energy X-ray bursts through collision with neutral hydrogen atoms (nonthermal bremsstrahlung) On the other hand, there are evidences that at least some of the centimeter-wavelength bursts, particularly those unaccompanied by meter-wavelength bursts, and those associated low energy X-ray bursts may be due to thermal bremsstrahlung The occasional occurrence of meter-wave Type III bursts at higher altitudes in the corona in association with high energy X-ray bursts is probably due to the fact that some of the electrons produced during the flare are accelerated upwards, possibly as a consequence of an irregular flare structure, and move through the corona without being "braked". The "unbraked" electrons may excite Type III bursts at higher levels in the corona, but they do not seem to play any significant role in the production of high energy X-rays

OGO-III solar radio bursts have been correlated with solar X-ray events detected by ionization chambers aboard OGO III (Arnoldy, Kane, and Winckler, 1967, 1968a, 1968b) and OSO-III, in the latter case with unpublished data made available by Dr R G. Teske. The OSO-III detector was used for the more detailed of the two investigations The results, which are summarized in Table 13, give a computed 4-2 MHz radio burst/X-ray event association of 60 per cent, a figure of the same order of magnitude, but somewhat

4-2 MHz events with concurrent OSO-III observation.	70
4-2 MHz events with an X-ray event in progress within $\pm$ 5 minutes of the 4-2 MHz event:	42
4-2 MHz events with no X-ray event in progress within $\pm$ 5 minutes of the 4-2 MHz event:	28

Table 13. Correlation of Solar X-ray Bursts with 4-2 MHz Solar Radio Bursts.

lower than, that derived for the association of low-frequency radio bursts with optical flares Teske (private communication) suggests that such a result is simply a manifestation of the high degree of correlation between X-ray events and optical flares.

A precise specification of the relationship between X-ray events and low-frequency radio bursts cannot be derived from the data available here It is possible that no unique relationship exists, and that the observed characteristics of the two types of events are controlled by the instantaneous magnetic field structure in the chromosphere at the moment of instability

C Correlation With Solar Flare Observations

1 Event Correlation

The association of a solar radio burst originating at four or five solar radii with a particular center of activity at the solar photosphere is not always an unambiguous process The basic assumption involved in the association is that the same instability which produces the suprathermal stream of electrons responsible for the radio burst is also the cause of the increase in Hα intensity occurring during a solar flare If this assumption is used as a starting point for the correlation, it then becomes necessary to place limits on the time interval between the two events In this study a 4-2 MHz radio burst was considered to be associated with a solar flare if the burst began

within ± 5 minutes of the observed flare duration. This criterion is not extremely restrictive, and its use may be expected to produce a certain number of chance associations. Nevertheless, the results which have resulted appear to justify such a choice as opposed to one in which the association requirement is more stringent

Using the criterion specified above, the solar radio burst events were checked against the Worldwide List of Flares and Subflares, World Data Center B, France, kindly made available by Dr. H. D. Prince Since no attempt was made to judge the reliability of the flare data the correlation may be regarded as an upper limit in terms of reported flares and subflares Of the 218 OGO-III events detected during the period under study, 166 were found to be "associated", according to the above definition, with a reported flare or subflare Four events occurred when no optical flare patrol observations were made The resulting correlation is thus 78%.

In order to relate the optical features of the sun to solar radio burst characteristics, the properties of the flares associated with the solar bursts were studied. Table 14 shows the number of flares and subflares in each importance classification which were found to have such an association It is immediately apparent that flares associated with solar radio bursts are not necessarily major ones. Such a result has been suggested by the burst/flare correlation work of Giovanelli (1959) The importance distribution, in fact, closely approximates the distribution of all reported optical flares (Smith and Smith, 1963)

Subflare reporting is much too heterogeneous to allow such a comparison, but it is significant that two thirds of all low-frequency solar bursts observed are associated with subflares.

Importance	Bright	Normal	Faint	Total[8]
S	17	73	21	111
1	16	18	2	36
2	6	4	0	10
3	2	0	0	2

Table 14 Distribution of Importance Ratings for Optical Flares Associated with 4-2 MHz Solar Radio Bursts.

Another approach to the correlation of optical and radio data is to compare the relative importance levels of associated events. Such a comparison is made in Table 15. No significant trend is apparent, although there is some evidence that a major optical flare is more likely to produce a major radio event than is a minor flare

Analysis of the heliographic distribution of flares associated with solar radio bursts shows that the associated flares are well distributed over the disk No evidence exists to indicate that radio bursts originating from any particular position on the apparent solar disk, either East or West, are less likely to be observed by OGO-III.

[8] Seven flares were associated with two radio bursts

Importance (4-2 MHz)	Optical Flare Importance									No Associated Flare
	Sf	Sn	Sb	1f	1n	1b	2n	2b	3b	
1	13	31	6	2	4	5	3	0	0	18
2	7	19	7	0	9	5	1	1	2	20
3	1	22	3	0	3	6	0	3	0	10
4	0	1	1	0	2	0	0	2	0	0

Table 15 The Correlation of 4-2 MHz Event Importance Ratings with Importance Ratings for Associated Optical Flares [9]

The significant results of this study of the relationship of low-frequency bursts and optical flares are that the correlation appears to be considerably above 50 per cent, that it is only moderately dependent on flare importance, and that association with subflares accounts for a majority of all associations which have resulted

2 Time Association With Flare Maximum

Previous studies of the association of solar radio bursts with optical flares have indicated that fast drift radio bursts tend to precede the maximum phase of the flares, and to be approximately coincident with the flash phase (Malville, 1962a) In order to examine the flare-burst time relationship for low-frequency solar bursts, the time

[9] Seven flares were associated with two radio bursts; the bursts are thus considered to be a single event and appear in this table only once, under the higher importance rating Four bursts occurred during gaps in optical flare patrolling and are not included in the totals given here

intervals between reported flare maxima and radio burst start times are plotted in the form of a histogram in Figure 32, both for all associated flares and for only those of Importance 1 or greater. The figure clearly demonstrates a tendency for a low-frequency radio burst to begin prior to the maximum of its associated flare. It is of interest that radio bursts associated with the more major flares are more likely to precede the reported flare maximum than are those which are subflare-associated Such an effect would not have been noted had more restrictive limits, such as $\pm$ 5 minutes from reported flare maximum, been placed on the association. The average time difference between the start of a radio burst and the maximum of the associated subflare is 1 9 minutes For flares $\geq$ Importance 1, this figure is 3. 9 minutes The time required for an electron stream moving at 0 25 c to travel from the photosphere to the vicinity of 5 $R_{\odot}$ (the 4 MHz plasma frequency level) is approximately 38 seconds. It thus appears that the electron stream responsible for a solar radio burst at 4-2 MHz is emitted from the point of instability approximately 2-1/2 minutes prior to the time of maximum H_{α} intensity of the associated subflare For flares of Importance 1 or greater, this time interval is approximately 4-1/2 minutes These results are entirely consistent with radio burst production occurring during the period of strong pre-maximum growth of the optical flare

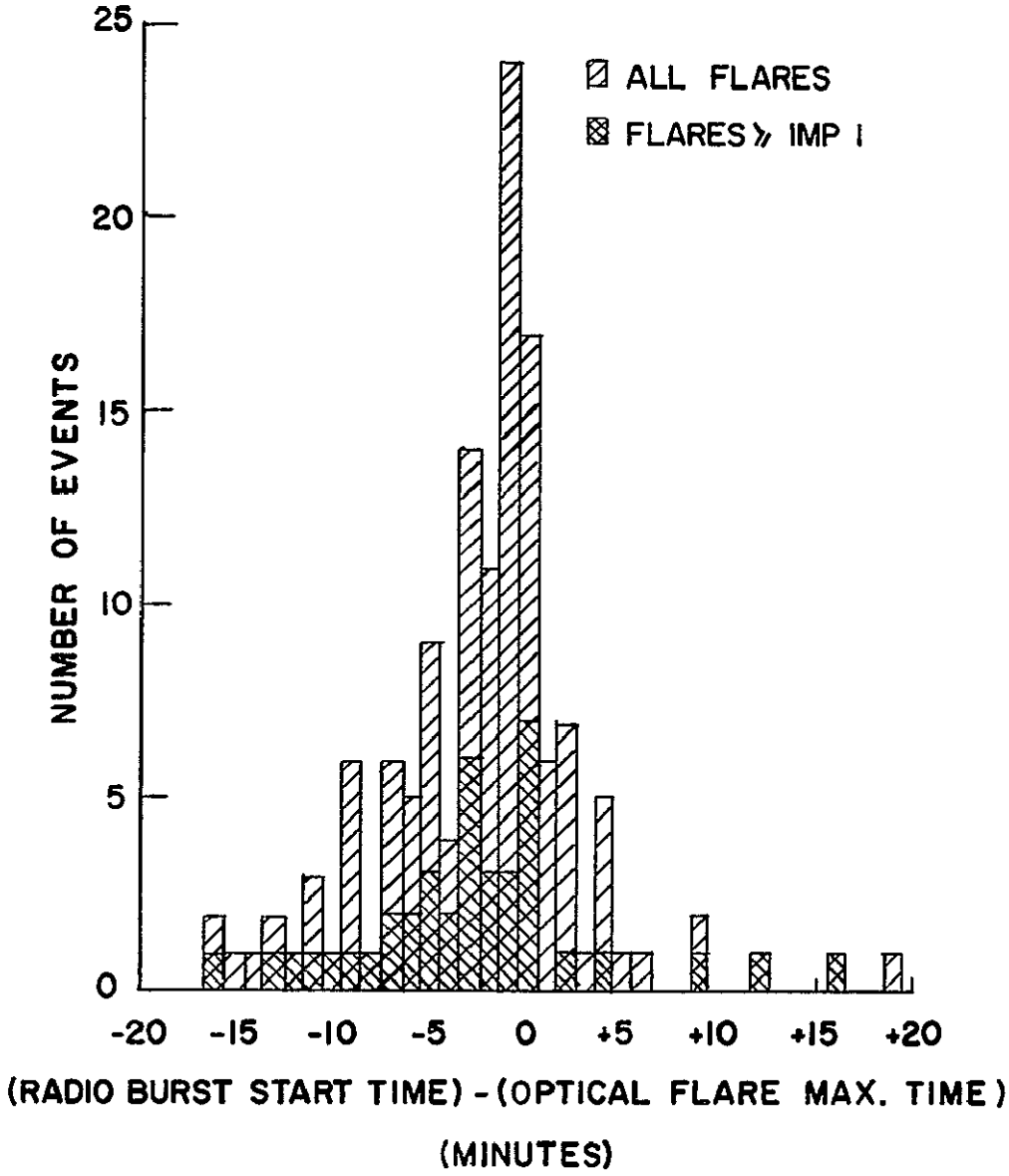

Figure 32 Histogram of Time Interval Between Radio Burst Start and Associated Flare Maximum

3. Characteristics of Associated Regions

A total of 58 plage regions were found to be regions of origin for flares or subflares associated with OGO-III radio bursts It is entirely possible that some of the identifications may be fortuitous, particularly those in which only one or two radio bursts were associated with a particular plage region Several plage regions, however, proved to be prolific producers of flares associated with radio bursts at 4-2 MHz Table 16 lists the plage regions which were associated with the greatest number of bursts for the period June 13, 1966 to September 30, 1967, together with information concerning the characteristics of each region The region ages, intensities, and central meridian passage (CMP) plage areas are those determined by the McMath-Hulbert Observatory Data on CMP sunspot areas and coronal line indices are from the Sacramento Peak Observatory The sunspot field strengths are those measured by Mount Wilson-Palomar Observatories An indication of the radio burst activity of these regions is that they were responsible for 54% of all radio burst-associated flares for the period of study, while all other plage regions contributed the remainder It is these burst-prolific plage regions which must therefore be examined in detail in an attempt to identify the optical solar phenomena which are associated with low-frequency solar radio bursts.

The general characteristics of the plage regions selected by the radio burst data are those of regions judged very important by the

Radio Burst Production Rating	McMath Plage Number	CMP	Number of Associated Radio Bursts	Age (Solar Rotations)	CMP Plage Area (Millionths)	CMP Intensity	CMP Sunspot Area (Millionths)	Maximum Sunspot Field Strength (Gauss)	CMP Coronal G6 Index
1	8905	7/28/67	19	1 and 3*	7,200	3.5	1500	2800	119
2	8907	7/20/67	15	1	4,300	3.0	530	2800	116
3	8740	3/27/67	12	3	9,800	3 5	840	2300	131
4	8863	6/26/67	12	2	5,000	3.0	280	2300	103
5	8704	2/27/67	8	2 and 4	8,500	3.5	1600	2800	119
6	8942	8/26/67	7	2 and 4	15,600	3.5	910	2800	119
7	8818	5/25/67	4	2	10,000	4.0	1700	2800	89
8	8546	10/18/66	4	2	5,000	3.0	390	2300	83
9	8716	3/10/67	4	1	4,500	3.5	580	2300	73
10	8629	1/2/67	4	1	1,800**	3.5	270	2300	31

*Had a resurgence on the invisible solar hemisphere.

**Grew rapidly and reached 3900 before west limb passage

Table 16. Characteristics of Plage Regions Associated with Four or More 4-2 MHz Solar Radio Bursts.

application of nearly every common criterion. For the period covered by this study, Dr. H. D Prince has selected fifteen regions as those which were most flare-rich, using IAU Solar Data Bulletin information. Nine of the ten regions discussed here (the exception being 8716) are included in the list, thus marking them as outstanding flare producers The sunspot areas and field strengths were all quite substantial. The intensities and areas of the plage regions are compared in Figure 33 with those of all regions which appeared on the solar disk during the period of this study It is apparent that the radio burst-associated regions are outstanding by these criteria also, although not every large, bright region was associated with the radio bursts. The regions were not necessarily correlated with major geomagnetic disturbances The two largest in terms of radio burst production, 8905 and 8907, did not produce solar protons or demonstrate any significant geomagnetic effects at all.

The coronal line index is an observational parameter which indicates the level of activity in the lower corona. Table 16 gives the average value of the index G6 for both East and West limb passages of the plage regions studied here. (Intensity measurements are made at 5^{o} intervals along the limb; the G6 index is the average of the six highest measurements in the green coronal line of Fe XIV for the quadrant specified) Although it is impossible to predict which important coronometer structures are streamer-associated (MacQueen, 1968), the lack of a significant line index level at a given position

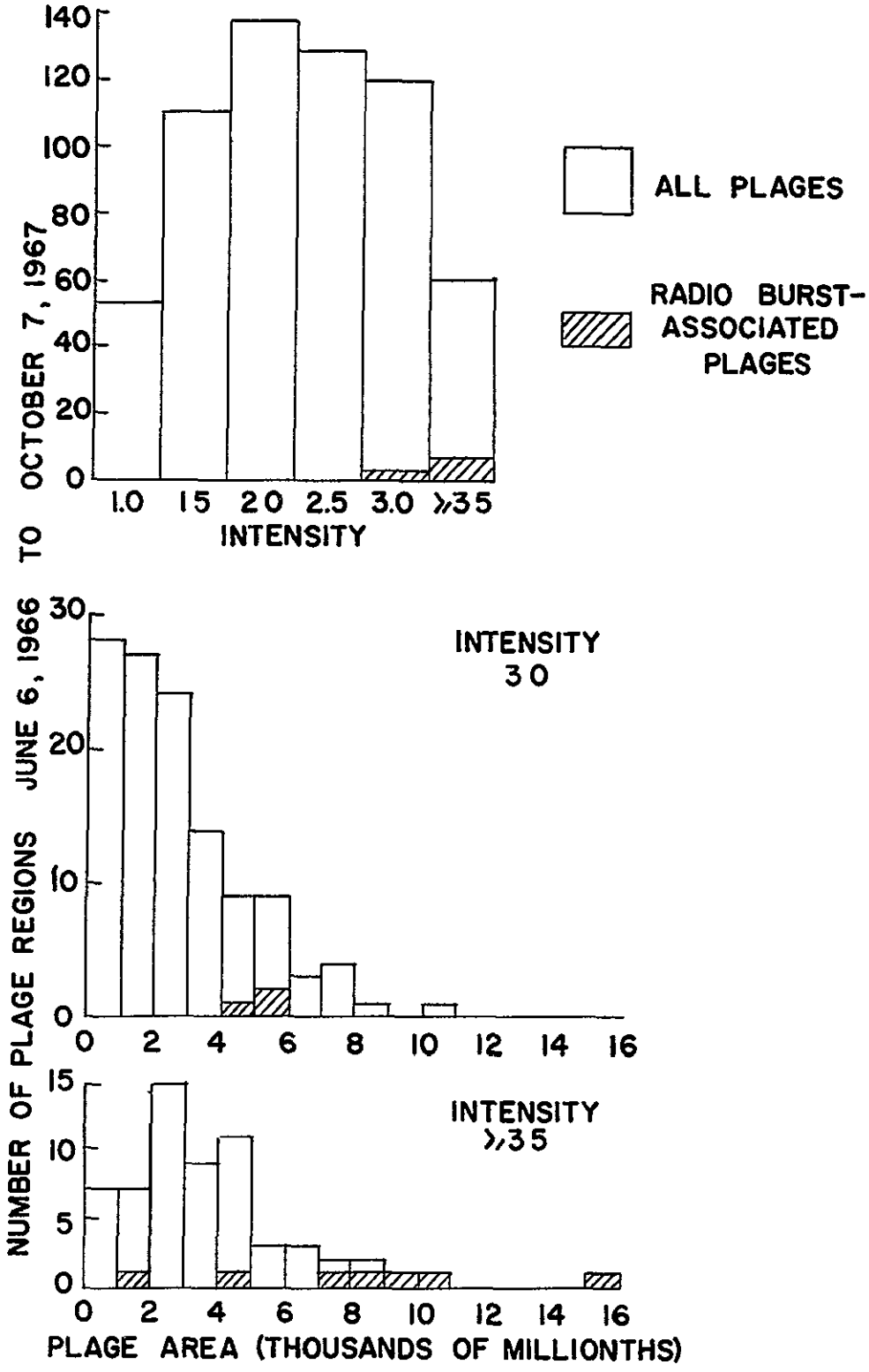

Figure 33 Comparison of Radio Burst-Associated Plages with All Plages for the Period June 6, 1966 to October 7, 1967

presumably indicates that no streamer can have its base at that location (see, for example, the streamer maps and coronometer isophotes illustrated by Bohlin, 1968). It may therefore be of importance that radio burst activity in a region is at least roughly consistent with a high coronal line index, as is shown in Table 16

Some suggestions regarding the evolution of solar conditions suitable for the occurrence of radio bursts of the fast drift type may be gleaned from an examination of the individual plage regions. For this reason a short history of each region is given below, the regions being listed in chronological order along with their radio burst production rating, solar latitude, and CMP date.

Region 8546. (#6) (N 23°) (8/26/67) This region appeared on the East solar limb on October 11, 1966, representing the return of two regions, one of which had been relatively flare-rich in its first rotation On October 19 a large filament to the East of the region began to fade, and had almost disappeared by October 21. The 20th and 21st of October also saw rapid growth of the major sunspot group in the region. Region 8546 was a good flare producer.

Region 8629. (#10) (S 23°) (1/2/67) This region was the first major flare producer in the southern hemisphere for solar cycle 20. It was characterized by rapid change. The plage and spot

formed on the visible disk and grew rapidly on December 29-30 The region's area increased markedly from 1800 millionths at CMP to 3900 millionths before West limb passage.

Region 8704. (#5) (N 23°) (2/27/67)

Representing the return of a smaller region, 8704 was in every sense a strong, large solar center of activity. Flare production was very high. The Mount Wilson-Palomar magnetic field measurements indicated that the field strength of the major sunspot was greater over the disk passage than for any other region discussed here

Region 8716 (#7) (S 22°) (3/10/67)

Born on the back of the solar disk, this plage region was already large and well developed at East limb appearance on March 3, 1967 The region was only a moderate flare producer, and the flares occurred primarily during the first half of its disk passage A filament near the region grew noticeably just prior to CMP.

Region 8740 (#3) (N 22°) (3/27/67)

This large, active region is particularly interesting in that it was the return of Region 8704, which was also an active radio burst producer. Both flare production and burst production remained high. The

sunspot characteristics were not as unusual as those of 8704, but the group was magnetically complex on at least 3 days during its transit of the disk

Region 8818 (#7) (N 25°) (5/25/67)

Many similarities existed between this region and 8704 Both were large, had substantial sunspots, and were good flare producers. Region 8818 was flare-rich during its entire disk passage On May 22 a filament suddenly appeared 15° to the West of the region, remaining essentially stable thereafter.

Region 8863. (#4) (N 22°) (6/26/67)

This region was large and bright, but was only a moderate flare producer with respect to most of the other regions discussed here. Although the principal sunspot was not large, it contained a γ configuration A most distinctive event associated with the region was the disappearance of a very large filament between June 23 and June 24.

Region 8905 (#1) (N 27°) (7/28/67)

This great region is perhaps the most distinctive one of the entire time period studied here Very large and very bright, it produced more flares and radio bursts than any other region. Major growth of a filament to the North of the region between July 25-30 was observed

Region 8907. (#2) (N 17°) (7/30/67)

A close association existed between this region and 8905, which preceded it by two days and was 10° higher in latitude In itself, 8907 was a good flare producer, with a large, strong sunspot group. The combination of this region and 8905 caused an extremely high level of solar activity during its disk passage The filament growth near 8905 may also be significant for this region.

Region 8942. (#6) (N 23°) (8/26/67)

This very large and interesting region represented the return of the combined Regions 8905 and 8907, and as such was the second case in this study in which a region produced radio burst-associated flares on two successive rotations The region very nearly equalled 8905 in flare production. A small filament near the plage became very dark and conspicuous between August 27-28. In addition, a southern region at the same longitude as 8942 showed rapid sunspot growth on August 24-26. Whether any physical relationship existed between the two regions is not known

It is interesting to note that most of the regions discussed here demonstrated extremely erratic radio burst production as a function of time, as shown in Figure 34 In most cases the periods of enhanced radio burst production were not directly dependent on the flare

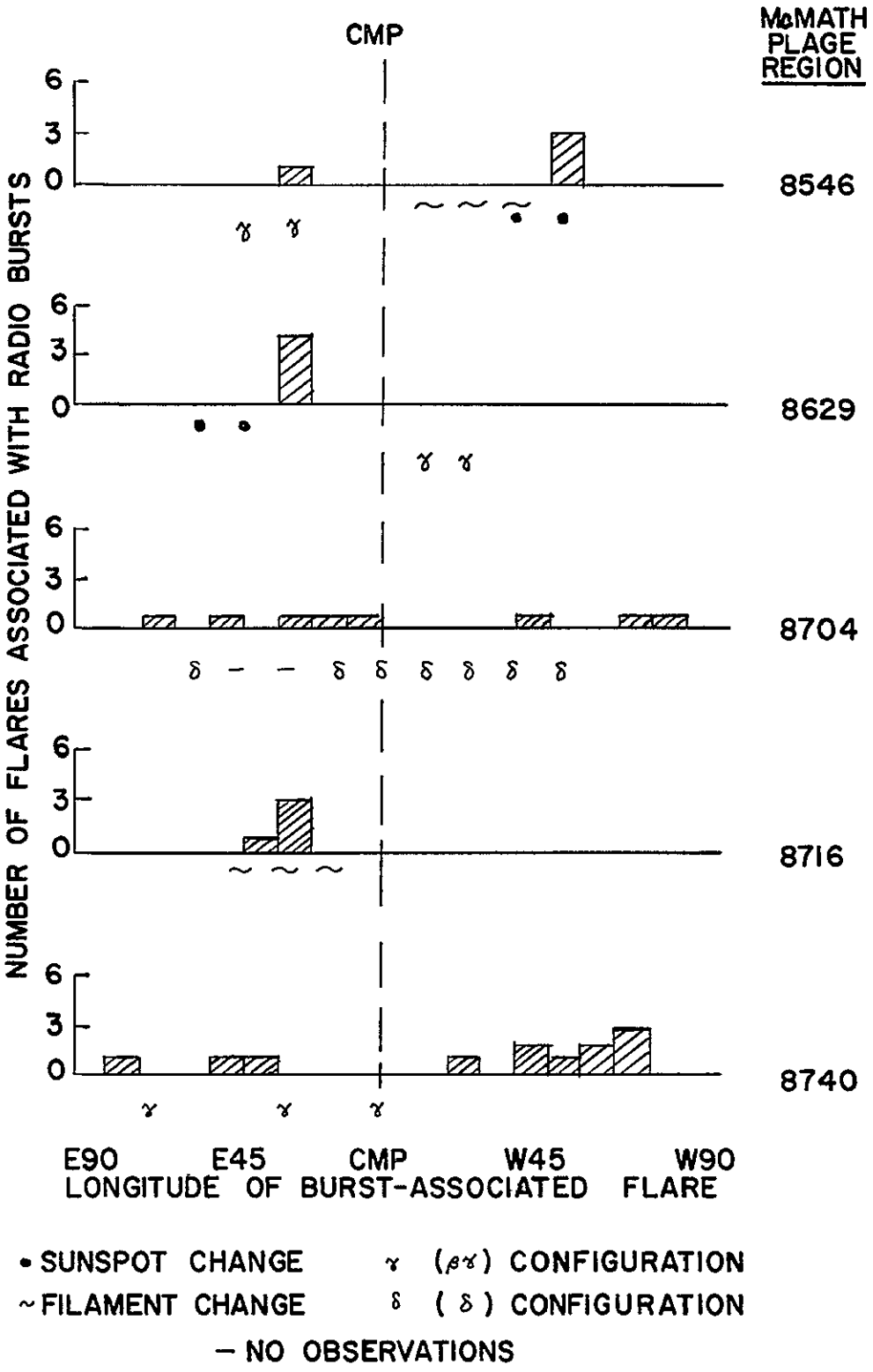

Figure 34A Heliographic Distribution of Burst-Associated Flares in Selected Regions See text for further explanation of indicated changes

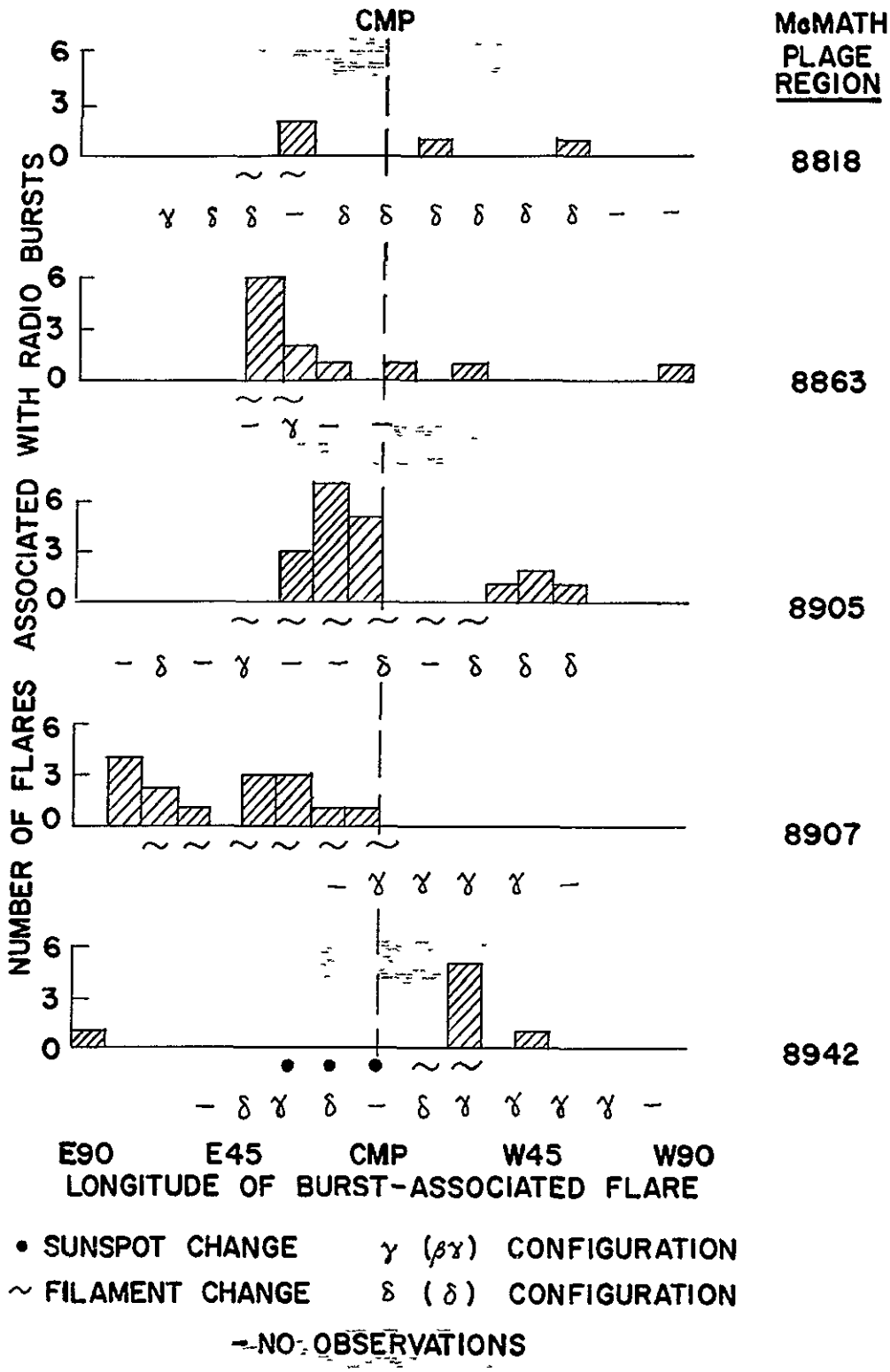

Figure 34B Heliographic Distribution of Burst-Associated Flares in Selected Regions. See text for further explanation of indicated changes

production of the region, which tended to be considerably more uniform The obvious question to ask is whether any observed changes in the regions can be held responsible for the enhanced radio burst production As an approach to this question, Figure 34 shows the periods of major filament or sunspot changes in or near the selected regions, and indicates the days on which $\beta\gamma$ or δ sunspot configurations were observed in the regions. It may be significant that every major sunspot or filament change preceded or coexisted with a period of solar radio burst activity The sunspot magnetic field configuration does not appear to exercise direct control over radio burst production, although the regions certainly tended to possess the $\beta\gamma$ and δ configurations in which mixing of the magnetic field polarities is observed

4 Implications for Coronal Streamer Structure

From the characteristics of the plage regions studied here, it is possible to specify some of the requirements for coronal streamer production It appears that nearly all large, very bright, flare-rich plage regions are associated with streamers having a radial extent of at least 5 $R_{\odot}$ The regions involved had large sunspot groups with strong magnetic fields, and most had high coronal line index values The data also suggest the possibility that any major change in filament or sunspot structure in a large plage can temporarily create or enhance the conditions necessary for the propagation of electron streams to large radial distances.

Although the data are not conclusive, it appears that the formation time for a streamer over a newly-formed active region can be as short as about three days (Region 8629). The majority of the regions associated with 4-2 MHz solar bursts were in at least their second rotation, however, so that a longer streamer formation time appears to be more usual. The two cases in which the same plage region was associated with radio bursts on two successive rotations suggest that well established streamers maintain their integrity and magnetic field structure for up to two rotations. Such lifetimes are in good agreement with the minimum streamer lifetimes deduced by Bohlin (1968).[10]

D. Burst Mechanism Characteristics Indicated by Observations

1 The Average Burst Profile at 3.5 MHz

The measured parameters of the 3.5 MHz burst profiles derived from OGO-III data are listed in Table 7 In order to specify the form of the average 3 5 MHz profile produced by a low-frequency solar radio burst, numerical averages of these parameters have been computed. The resulting values are given in Table 17.

---

[10] The results discussed herein rely upon the assumption that emission occurs at the local plasma frequency After the completion of this paper, the author's attention was called to a recent publication by V I Slysh (Cosmic Res 5, 759, 1967) in which evidence is presented for emission at $f > f_p$ The conclusion is based on just two bursts, only one of which is confirmed by other observers Slysh's work has been criticized by French scientists because of poor calibration techniques and inappropriate theoretical treatment (Weil, private communication)

Fraction of Peak Flux Density at Point of Measurement	A	B	A/B
0 900	6.1 sec	10.6 sec	0.57
0 800	9 5	14.7	0 65
0 600	14 5	24 0	0 60
0 368	21.4	33 8	0 63

Table 17 Profile Parameters for the Average 3 5 MHz Radio Burst.

The best fit to the above profile was obtained for a theoretical model having the characteristics specified in Table 18.

Instantaneous Burst Bandwidth = 900 kHz

Electron Injection Model = G3 (Figure 29)

Collisional Frequency: $\varphi(T) = 0\ 055\ \text{sec}^{-1}$

Kinetic Temperature = $2\ 4 \times 10^{5}\ ^{o}K$.

Table 18 Burst Mechanism Characteristics for the Best-Fit Theoretical Model

Figure 25 depicts the profiles described by Tables 17 and 18 It is apparent that although minor variations exist the forms of both curves are virtually identical The agreement of the leading segments of the profiles suggests that the derived bandwidth is of the correct order of magnitude The distinction between this value and the values of instantaneous observed bandwidth has been discussed in a preliminary

Figure 35. Radio Burst Profiles for Average 3.5 MHz Model and Best-Fit Theoretical Model.

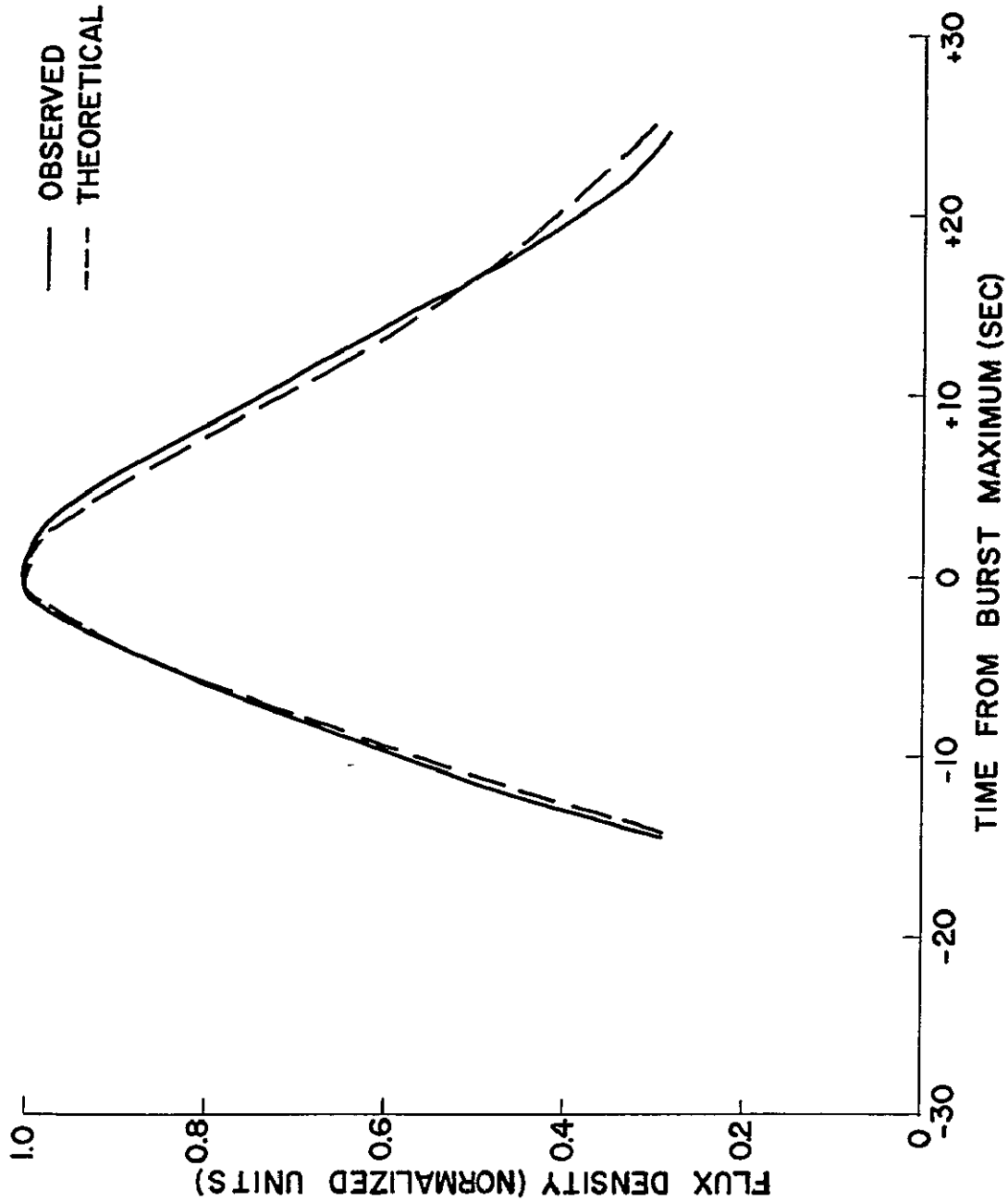

way by Hughes and Harkness (1963). The observed bandwidth is the result of the reception of the total burst emission from all contributing coronal levels at a given time. It is thus strongly influenced by the instrument sweeping rate and the velocity of the burst exciter A burst exciter moving at constant velocity traverses a range of high-frequency electron density levels much more rapidly than it traverses a range of low-frequency levels, due to the coronal electron density gradient, which decreases with distance from the sun. Instruments with similar time resolution should thus observe a much broader instantaneous bandwidth at higher frequencies than at low frequencies The data of Hughes and Harkness (1963) and Hartz (1964) are consistent with such a hypothesis, as are the bursts illustrated by Sheridan and Attwood (1962).

The bandwidth value given in Table 18 refers to the instantaneous bandwidth from the 3 5 MHz coronal level only, rather than to the observed bandwidth, and thus specifies a characteristic of the emission spectrum at that level. Theoretical considerations (Jaeger and Westfold, 1949; Malville, 1962b) have suggested emission bandwidths of less than 1 MHz The evidence presented here fully supports their suggestion In fact, an emission bandwidth of, for example, 5 MHz would predict a rise time of thirty seconds or more from start to maximum for bursts at 4 MHz Such values have not been observed.

The derived electron injection model is incomplete in that it consists of the integration of the dispersion of the electron stream

with the relative enhancement of emission due to its wave coupling mechanism. It has been pointed out in Chapter V that the various wave-coupling models had little effect by themselves on the appearance of the radio burst profile. The coupling model ambiguity cannot be clarified by OGO-III data alone, and thus the electron velocity dispersion cannot be rigorously specified It is, however, possible to place limits on the time scale of the injection of suprathermal electrons at the 3 5 MHz level For the average burst profile discussed here, the time scale must be on the order of twenty seconds, a figure which is reasonable in view of the distance of the level from the suprathermal electron source and the probable distribution of initial electron velocities.

The derived collisional frequency and coronal temperature value will be discussed in detail and compared with other observational data later in this chapter

2. Analysis of Individual Burst Profiles at 3. 5 MHz

Although it is possible to specify an average profile for a 3. 5 MHz solar radio burst, the actual data show variations from this average The differences can be explained by variations in the electron injection profile and in the ambient temperature of the burst region

The derived bandwidths, collisional frequencies and electron kinetic temperatures for individual bursts are given in Table 19.

UM/RAO Event Number	Bandwidth	Collisional Frequency $\varphi(T)$	Kinetic Electron Temperature
2	?	0.100	1.6×10^5 °K
4	400 kHz	0.070	2.0
37	650	0.070	2.0
59a	900	0.050	2.5
59b	900	0.021	4.5
66	900	0.065	2.1
80	400	0.035	3.2
104a	650	0.065	2.1
104b	900	0.035	3.2
155	900	0.070	2.0
159	> 900	0.065	2.1
160a	900	0.100	1.6
160b	900	0.100	1.6
209	900	0.060	2.2
217	900	0.070	2.0
328	< 400	> 0.100	< 1.6
329a	< 400	> 0.100	< 1.6
329b	> 900	0.021	4.5
452	900	0.040	2.9

Table 19 Bandwidths, Collisional Frequencies and Kinetic Electron Temperatures Derived from Analysis of Individual Burst Profiles.

UM/RAO Event Number	Bandwidth	Collisional Frequency $\varphi(T)$	Kinetic Electron Temperature
454	650 kHz	0.070	2.0×10^5 °K
461a	650	0.040	2.9
461b	400	0.040	2 9
474	400	0 070	2 0
477	> 900	0 040	2 9
479	900?	0.021?	4 5?
481	400	0 100	1.6
488	900	0.055	2 4
501	> 900	0.030	3.6
503	< 400	> 0.100	< 1 6
504	400	0 040	2.9
514	900	0.030	3.6
560	900	0.100	1 6
614	400	0 100	1.6
676	400	0 050	2 5
678	< 400	0.040	2 9
680	400	0.100	1 6
683	400	0.070	2 0
684	< 400	0.065	2 1
686	400	0 070	2.0

(Table 19, Cont.)

UM/RAO Event Number	Bandwidth	Collisional Frequency $\varphi(T)$	Kinetic Electron Temperature
687	400 kHz	0 040	2.9×10^5 °K
692	400	0.065	2 1
695	400	0 070	2 0
1101	900	0 021	4 5
1151	900	0.100	1.6

(Table 19, Cont.)

Individual bursts were fitted to an array of electron injection and damping models, and to two bandwidth models within this matrix at 400 kHz and 900 kHz. A computed profile using one of these two bandwidths reproduced the observed data in most cases If the observed profile was obviously between the two values a bandwidth of 650 kHz was assigned. It is apparent from a study of Table 17 that the average profile has been weighted toward a wider bandwidth by a few very large values It appears that about 80% of the bursts studied here are consistent with an emission bandwidth of 650 $\pm$ 250 kHz

No attempt has been made to study in detail the variation in electron injection/wave-coupling models implied by the observed profiles. It is felt that resolution of this problem will require accurate radio burst profiles from a wide range of frequencies Such a program could use, for example, a combination of ground-based radio spectral data and data obtained by OGO-V, or other spacecraft experiments operating over a range of low frequencies. The OGO-III data indicate that the time scale for electron injection into the 3 5 MHz level varies within the range of ten to thirty seconds, being most frequently of the order of twenty seconds.

The temperatures derived from the individual burst profiles cover a range $1.6 \times 10^5 \leq T \leq 4.5 \times 10^5$ ^oK. If a constant coronal temperature function with radial distance is assumed, as has been the approach of Newkirk (1967) and others, a variation of about a factor of five in the densities of different coronal streamers would change the

radial distance of the 3.5 MHz level enough to make this temperature range plausible Such an interpretation implies that solar radio bursts originating from the same streamer within a short time period should satisfy the same density model. The OGO-III data sample is not large, but suggests that this is indeed the case Events 328 and 329a occur about three hours apart; both give $T < 1\ 6 \times 10^5\ ^oK$. Events 683, 684 and 686 take place within a four hour interval; the derived temperature range is $2.0 \times 10^5\ ^oK \leq T \leq 2\ 1 \times 10^5\ ^oK$

Two multiple events in which the two measured profiles are well separated, 160a and b and 461a and b, likewise give similar temperatures Events 59a and b, 104a and b and 329a and b are multi-multiple events in which the individual burst profiles are intermingled or distorted; in each case the individual events give substantially different temperatures Events 503 and 504 represent another situation They occur less than an hour apart, but are identified with completely different centers of activity on the sun The derived temperatures differ by about a factor or two

E Coronal Parameters Inferred From Low-Frequency Observations

1. Electron Density Model

It was pointed out in Chapter IV that the electron density structure of the far corona is not well known and that a density model for streamers is less well known Furthermore, any model is at best an

average over the range of actual density values Even the most cursory glance at a solar eclipse photograph on which more than one coronal streamer is visible is convincing evidence that no unique density structure exists for the streamers This is the probable reason for the differences between the streamer density models of Bohlin (1968), Michard (1954), Saito (1959) and Schmidt (1953), all of whom studied different coronal streamers. The probability of a range of ellipticity in the three-dimensional density structure (Bohlin, 1968) further complicates the problem. It is very important to note that at 5 $R_{\odot}$ the streamer density derived by Michard is greater than that of Saito by about a factor of three and that of Saito exceeds that of Schmidt by approximately the same amount If these electron densities are correct, the effect on temperature models derived from radio bursts originating in different streamers is very great indeed

In spite of these ambiguities, the specification of an average electron density model from streamers is of value. Such a model provides information which is needed for a study of the problems of interaction between the chromosphere, the corona and the solar wind. Radio astronomers have hitherto specified coronal streamer electron densities by interpretation of interferometric measurements. A new method of determining the electron density gradient as a function of frequency which has been developed by the author is presented below

The drift rate of the exciting impulse for 4-2 MHz burst events was found to average 0.095 $\pm$ 0.010 MHz/sec Boischot (1967) has

recently obtained low-frequency drift rates from ground-based harmonic burst observations. His results, together with the higher frequency values of Maxwell, Howard and Garmire (1960) and Wild (1950), are compared with those of this paper in Figure 36 It is seen that the agreement is excellent The relationship between drift rate and frequency may be expressed by the equation for the line of best least squares fit to the points:

$$\log (df/dt) = 1.755 \log f - 1.890 , \qquad \text{(VI-1)}$$

which is plotted on the figure The significance of this equation can be made evident by substitution for some of the variables therein If it is assumed that the electron stream responsible for the burst moves at 0 25 c,

$$v = dr/dt = 0.25\ c = 0.107\ R_{\odot}/\text{sec} \qquad \text{(VI-2)}$$

Rearranging equation (VI-2) gives

$$dt = 9\ 35\ dr \qquad \text{(VI-3)}$$

where the units of t and r are seconds and solar radii, respectively Differentiating equation (V-2) gives

$$df = \frac{4\ 04 \times 10^{-5}}{f}\ dN_e . \qquad \text{(VI-4)}$$

Substituting equations (VI-3) and (VI-4) into equation (VI-1) and rearranging gives

Figure 36 Observed Drift Rate as a Function of Observing Frequency

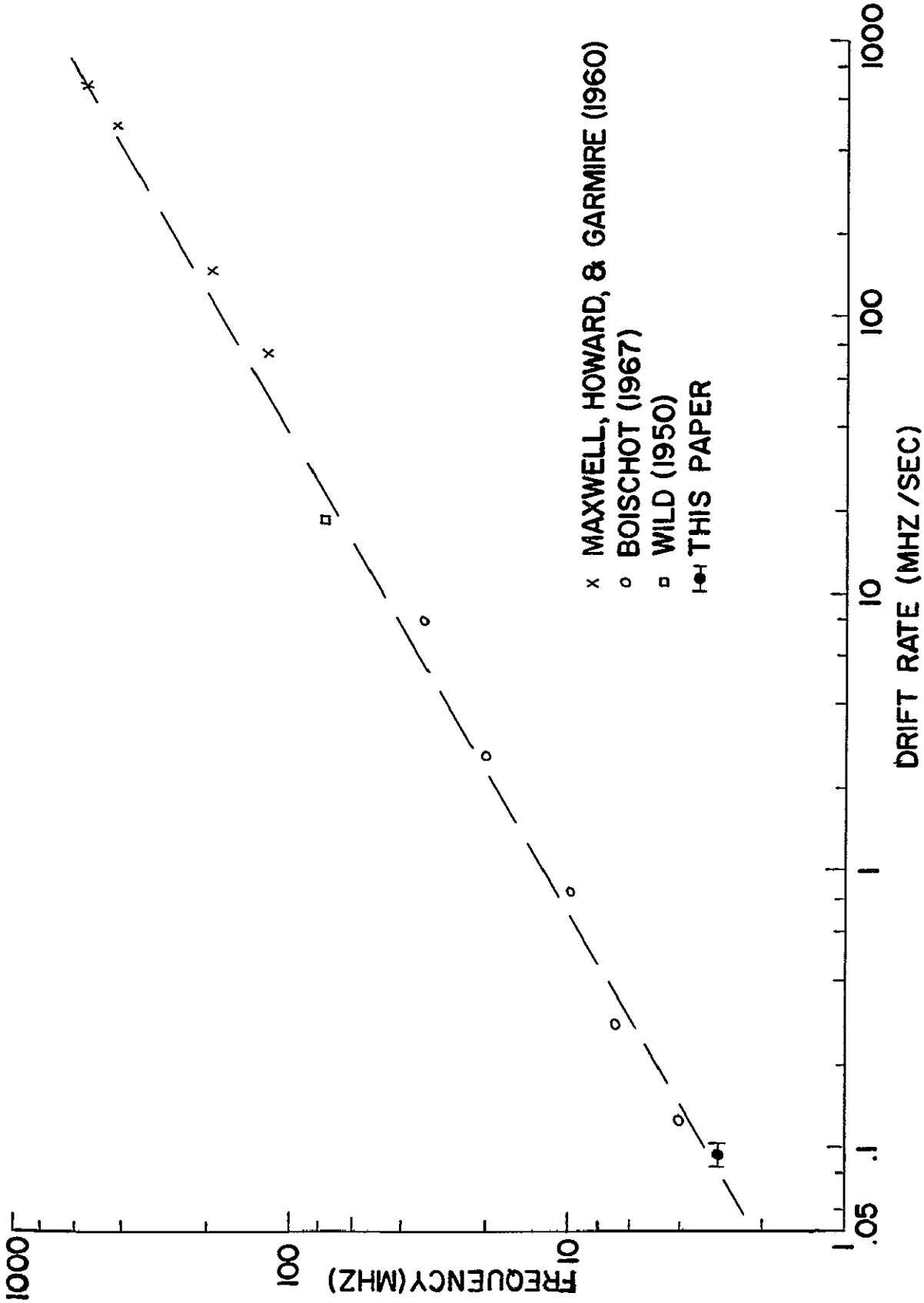

$$\log (dN_e/dr) = 2.755 \log f + 3\ 473 \qquad \text{(VI-5)}$$

which is an observationally determined equation for the change in electron density with coronal path difference as a function of frequency. This relationship is completely independent of interferometric measurements and is based solely on observations of the drift rate of burst impulses from 550-3 MHz, together with the assumption of constant exciter velocity In Table 20 the density gradient values computed from equation (VI-5) at three frequencies are compared with the values derived from the Malitson and Erickson (1966) density model. The agreement is excellent, with the two models converging near f = 10 MHz. The slightly higher values predicted by equation (VI-5) suggest a slightly increased slope for the electron density curve compared with the Malitson-Erickson model for $R < 4\ R_\odot$. A linear extrapolation of the Malitson-Erickson model appears to be satisfactory in the region $4\ R_\odot \leq R \leq 6\ R_\odot$, in view of the observations discussed here

f (MHz)	dN_e/dr Equation (VI-5)	dN_e/dr Malitson-Erickson
100	9.73×10^8 cm^{-3} $R_\odot^{-1}$	$6\ 07 \times 10^8$ cm^{-3} $R_\odot^{-1}$
50	$1\ 79 \times 10^8$	$1\ 03 \times 10^8$
10	$1\ 69 \times 10^6$	1.65×10^6

Table 20 Comparison of Electron Density Gradients Predicted by Equation (VI-5) with Those Derived from the Malitson-Erickson Model.

2. Temperature Model

The use of solar radio burst durations as coronal temperature indicators has been discussed in Chapter IV. The hypothesis is that the duration of a burst is related to the electron temperature at the plasma frequency level by the relationship given in equation (IV-1) which is rewritten here for convenience:

$$T_e = 0.65 \times 10^{-4} f_p^{4/3} \Delta t^{2/3} \qquad \text{(IV-1)}$$

Radio burst durations and the temperatures resulting therefrom have been determined at a wide range of frequencies At less than 5 MHz, the derived values for all frequencies are based on a combined total of less than fifty bursts It is reasonable to consider all published results to date as preliminary in nature. The statements of Hartz (1964) who has done much of the low-frequency work to date, support this assessment. On Figure 37 is plotted the published determinations of coronal temperature as a function of solar radial distance, as determined by radio burst measurements. The temperature derived in this paper from the mean e-folding time of solar bursts at 3.5 MHz is included in the figure The error bar indicates the limits of temperature listed in Table 19, and the limits of radial distance for the 3.5 MHz level, using the density models of Figure 17. Such values are at least semi-independent of those derived by the use of equation (IV-1). They are related, however, in that both are functions of the slope of the declining segment of the burst profile.

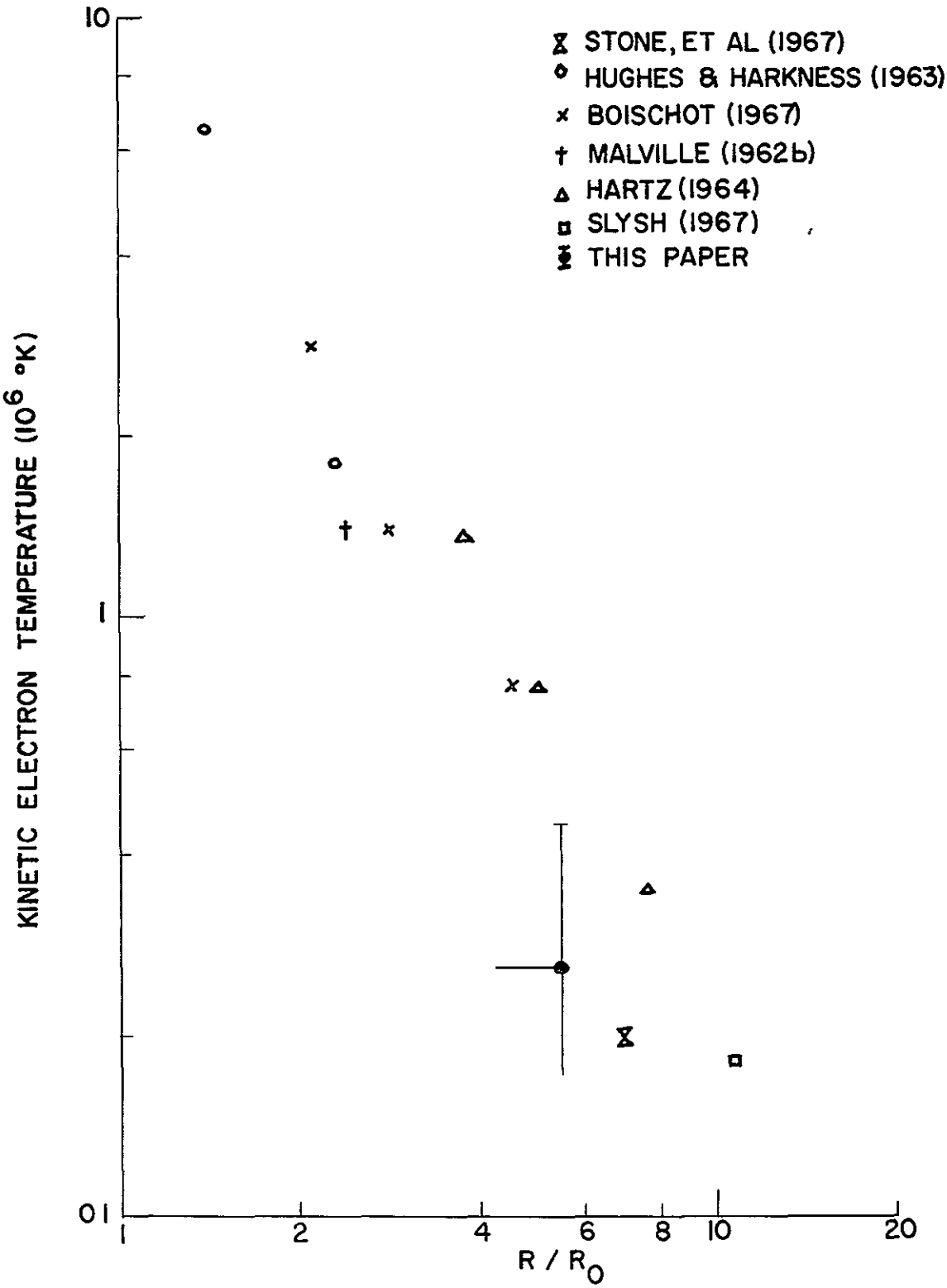

Figure 37 Coronal Temperature Values Derived from Radio Burst Duration Times

The temperature analysis of this paper has suggested that solar radio bursts do in fact originate in regions of substantially different temperature, and that this effect is caused primarily by a density variation in coronal streamers at four or five solar radii. It appears that the use of solar radio bursts for coronal temperature model-building is ill-advised Conversely, the results suggest that solar radio burst information, particularly at the lower frequencies, can provide at least rudimentary data on the evolution of coronal streamers, and on their densities and temperatures

F. Summary

The analysis which has been described in this dissertation was begun with the aim of specifying the characteristics of fast drift solar radio bursts occurring at frequencies below the ionospheric cutoff. The goal of describing these bursts in some detail has been achieved. In addition, theoretical analysis of the radio bursts permitted the observational determination of the average instantaneous emission bandwidth, the time scale of the electron injection responsible for 3 5 MHz radio bursts and the range of temperatures in the regions from which 3 5 MHz emission originates Finally, comparison of the radio burst data with information regarding optical solar features has permitted certain characteristics of the coronal streamer structure to be specified

The conclusions which can be drawn from this work can be summarized as follows:

1. Solar fast drift radio bursts with peak flux densities at least 2.8×10^{-17} watt $m^{-2} Hz^{-1}$ in the 4-2 MHz band were observed at the rate of approximately one burst per 50 hours of observation. These bursts showed a mean frequency drift rate of 0 095 ± 0 010 MHz/sec, and a mean e-folding duration of 23. 3 ± 1. 4 seconds at 3 5 MHz.

2 The tendency for fast drift bursts to occur in groups of from two to ten was not greatly noticeable in the low-frequency bursts studied A lower limit of 9% of all OGO-III bursts demonstrated this clustering characteristic.

3. Type V continuum was observed in 2% of all cases following fast drift bursts at low frequencies. No evidence of Type II radiation at detectable radiated energy levels was found Noise storm radiation may have been present, but the identification was not conclusive.

4. The detection of a reverse drift burst at low frequencies may indicate the presence of significant magnetic fields transverse to the radial direction at distances of approximately 5 $R_{\odot}$.

5. Fast drift radio bursts detected at low frequencies by OGO-III were also detected in 95.8% of all cases by ground-based observations at higher frequencies Conversely, only 20 5% of ground-based events were observed by OGO-III equipment. This is interpreted as being due to the low detection limit.

6 No significant relationship has been found between solar radio bursts at 4-2 MHz and solar X-ray bursts

7. Low-frequency solar radio bursts show a 78% correlation with optical flares and subflares, the bursts generally beginning approximately 2-1/2 minutes prior to the optical maximum of associated subflares and 4-1/2 minutes prior to the optical maximum of associated flares

8 The association of an optical flare or subflare with a low-frequency solar radio burst is only a very moderate function of the importance of the flare

9 The plage regions which produced the associated optical flares and low-frequency solar radio bursts were invariably large, with large sunspot groups and a high incidence of flare activity. The regions were relatively young, most of them being in their second rotation across the visible disk The suggested

radio burst lifetime for the coronal streamers associated with the active regions is ≤ 2 solar rotations.

10. Evidence is present to suggest that rapid change in a sunspot group or a filament may be connected with a temporary increase in low-frequency radio burst production from a plage region

11 The comparison of a theoretical model for the formation of radio burst profiles with observed profiles at 3.5 MHz indicates that the following characteristics are present in solar radio burst emission: instantaneous emission bandwidth = 650 ± 250 kHz; time scale of electron injection = 20 seconds; mean temperature at the 3.5 MHz level = 2.6×10^5 °K.

12 For the low-frequency solar radio bursts observed at 3.5 MHz, temperatures in the emitting regions varied over the range 1.6×10^5 °K $\leq T \leq 4.5 \times 10^5$ °K. Such a variation can be explained by postulating a density difference of up to a factor of five among the streamers associated with the radio bursts, for a constant T(r) model

The results which have been reported in this dissertation have been derived from the first large body of solar dynamic spectra of radio emission at frequencies below the ionospheric cutoff. Because

of the occurrence of the emission at the local plasma frequency, the observations describe coronal regions more distant from the sun than those studied at higher frequencies. Further observations from other spacecraft experiments at even lower frequencies, such as those now in operation aboard OGO-V and Radio Astronomy Explorer-1, promise to increase our knowledge of the solar corona and its radio emission mechanisms.

APPENDIX I

SOLAR RADIO BURSTS OBSERVED BY OGO-III

June 13, 1966 to September 30, 1967

UM/RAO Event No.	Date	Start Time (U.T.)	4-2 MHz Importance	Assoc Flare Imp	Assoc. Plage Region
1	6/13/66	1227	1	--	--
2	6/13	1611	2	sn	8336
3	6/13	2132	3	--	--
4	6/13	2156	2	sn	8336
5	6/14	0007	2	--	--
6	6/14	0328	2	--	--
13	6/17	0646	2	--	--
18	6/23	0525	1	sn	8340
25	6/24	0340	2	--	--
28	6/25	1538	3	1b	8348
35	6/29	0202	3	--	--
37	6/14	0011	3	--	--
59	7/7	0040	3	2b	8362
66	7/8	0953	4	1n	8362
77	7/12	0731	2	1n	8379
78	7/12	1103	1	sn	8397
80	7/12	1620	3	sn	8379

UM/RAO Event No.	Date	Start Time (U.T.)	4-2 MHz Importance	Assoc. Flare Imp.	Assoc. Plage Region
95	7/28/66	2151	3	--	--
99	7/11	2246	1	--	--
103	8/24	1230	3	--	--
104	8/28	1535	4	2b	8461
106	8/3	0037	1	--	--
155	9/9	1727	3	sn	8496
156	9/9	1936	1	sn	8496
158	9/10	1520	1	sn	8484
159	9/10	1722	3	sn	8484
160	9/11	0734	3	sb	8484
162	9/12	1335	2	--	--
166	9/17	0232	2	--	--
167	9/19	1527	3	sn	8496
172	9/21	1932	2	sn	8509
173	9/21	2029	1	sn	8509
176	9/25	1310	3	--	--
183	9/2	0555	2	3b	8461
184	9/17	0345	3	sf	8505
205	10/13	0136	1	--	--
208	10/13	1942	2	--	--
209	10/13	2019	3	sn	8545

UM/RAO Event No.	Date	Start Time (U.T.)	4-2 MHz Importance	Assoc Flare Imp.	Assoc. Plage Region
211	10/14/66	1845	2	--	--
214	10/18	1941	2	sn	8553
217	10/20	2154	2	sb	8546
219	10/21	0348	2	sn	8546
220	10/22	0348	1	sf	8546
255	11/6	1036	2	--	--
264	11/17	1407	2	--	--
270	11/24	2213	3	sn	8589
272	11/27	1825	2	sn	8586
306	12/9	1810	3	2b	8610
316	12/24	1120	1	sn	8624
321	12/26	1120	2	--	--
328	12/31	0844	3	1b	8629
329	12/31	1139	3	sn	8629
330	12/31	1653	4	sb	8629
331	12/31	1842	3	1b	8629
332	12/23	2352	2	sn	8625
333	12/23	0843	1	1n	8620
334	12/23	2109	1	sn	8625
335	12/23	0759	1	1b	8620
351	1/1/67	0242	3	--	--

UM/RAO Event No	Date	Start Time (U.T)	4-2 MHz Importance	Assoc. Flare Imp.	Assoc. Plage Region
367	1/25/67	0621	4	sn	8663
368	1/24	2019	3	1b	8663
369	1/15	2007	1	sn	8647
402	2/4	1650	1	2b	8682
403	2/4	1657	3	2b	8682
404	2/13	1804	2	3b	8687
405	2/23	0110	3	sn	8704
406	2/26	0858	2	1n	8704
407	2/27	0037	1	--	--
408	2/27	1224	3	sn	8704
410	2/4	1720	1	1b	8682
411	2/21	1604	2	1n	8704
412	2/25	1844	1	1b	8704
413	2/27	1339	1	--	--
414	2/4	1707	1	1b	8682
415	2/6	0259	1	sn	8684
451	3/2	2345	3	sn	8704
452	3/3	0524	3	--	--
453	3/3	0918	3	1n	8707
454	3/5	0944	2	1n	8704
455	3/6	2259	1	2n	8715

UM/RAO Event No.	Date	Start Time (U.T.)	4-2 MHz Importance	Assoc. Flare Imp.	Assoc. Plage Region
456	3/7/67	1008	1	1n	8716
457	3/7	1558	2	--	--
458	3/7	1708	3	--	--
459	3/7	1855	2	sn	8716
460	3/7	1902	2	sn	8716
461	3/9	0409	2	--	--
462	3/9	1113	2	1n	8715
463	3/9	1524	2	sf	8711
464	3/11	0927	3	sn	8715
465	3/19	1436	1	--	--
466	3/20	0815	1	1n	8733
467	3/20	1348	2	1n	8733
468	3/20	1718	1	sı	8740
469	3/20	2124	1	--	--
470	3/23	0938	1	sn	8740
471	3/23	1929	2	1b	8740
472	3/24	1440	2	--	--
473	3/26	0656	1	sn	8745
474	3/28	1209	3	sn	8740
475	3/29	2344	2	sn	8739
476	3/30	0337	1	sn	8754

UM/RAO Event No.	Date	Start Time (U.T.)	4-2 MHz Importance	Assoc. Flare Imp.	Assoc. Plage Region
477	3/30/67	0411	3	sn	8740
478	3/30	1725	2	sf	8740
479	3/30	1940	3	sn	8740
480	3/30	2111	1	sn	8740
481	3/31	1017	2	sb	8745
482	3/31	1100	1	--	--
483	3/7	1537	1	sb	8716
484	3/31	1703	2	sb	8740
485	3/22	1527	1	sn	8727
486	3/22	1733	1	--	--
488	3/4	0724	2	1b	8704
489	3/4	1313	1	sn	8714
490	3/23	1734	1	--	--
501	4/1	0758	4	--	--
502	4/1	0852	2	1b	8740
503	4/1	1319	1	sn	8739
504	4/1	1411	2	1b	8740
505	4/1	1609	3	--	--
506	4/1	1854	1	sn	8740
507	4/1	2339	2	--	--
509	4/3	1020	2	--	--
510	4/3	1625	2	--	--

UM/RAO Event No.	Date	Start Time (U.T.)	4-2 MHz Importance	Assoc. Flare Imp.	Assoc. Plage Region
514	4/24/67	1237	3	--	--
522	4/5	1902	1	sf	8758
523	4/14	1709	2	2n	8760
551	5/9	0936	1	--	--
558	5/27	1900	2	sf	8818
559	5/25	1924	2	sb	8818
560	5/29	1427	3	sn	8818
561	5/29	2101	2	sn	8821
562	5/30	2201	2	--	--
563	5/23	1842	2	2b	8818
601	6/12	0738	1	--	--
602	6/22	1637	1	sn	8863
603	6/22	1821	3	sn	8863
604	6/22	1943	2	sf	8863
605	6/22	2258	1	sf	8863
606	6/23	0040	3	1n	8863
607	6/23	0044	1	1n	8863
608	6/24	0208	3	sn	8863
609	6/26	0613	3	sn	8863
610	6/26	1726	1	sf	8862
611	6/26	2321	1	--	--

UM/RAO Event No.	Date	Start Time (U.T.)	4-2 MHz Importance	Assoc. Flare Imp.	Assoc. Plage Region
612	6/28/67	1300	1	sf	8863
613	6/27	0007	1	--	--
614	6/2	1245	2	sn	8821
615	6/23	1932	2	sb	8863
616	6/23	0312	1	sb	8863
651	7/1	0652	1	sb	8863
652	7/1	0846	1	sf	8877
653	7/3	0757	2	1n	8875
655	7/5	1617	2	sf	8875
656	7/5	1718	3	sb	8880
657	7/5	1844	1	1b	8875
663	7/13	0220	2	sb	8886
667	7/22	0229	1	--	--
669	7/24	0034	3	1n	8907
670	7/24	1000	3	1b	8907
671	7/24	2051	4	2b	8907
673	7/27	0008	1	sn	8905
675	7/27	0356	2	sn	8907
676	7/27	0600	1	sn	8905
677	7/27	0631	1	sn	8905
678	7/27	0713	3	sn	8905

UM/RAO Event No.	Date	Start Time (U.T.)	4-2 MHz Importance	Assoc. Flare Imp.	Assoc Plage Region
679	7/27/67	0901	1	sn	8905
680	7/27	0919	2	1n	8905
681	7/27	1004	1	sb	8907
682	7/27	1023	1	sf	8905
683	7/27	1113	2	sn	8905
684	7/27	1143	3	sb	8905
685	7/27	1233	1	sn	8907
686	7/27	1609	3	sn	8905
687	7/27	2012	3	sn	8905
688	7/28	0052	1	sf	8905
689	7/28	0145	1	sn	8907
690	7/28	0546	1	sn	8911
691	7/28	0838	1	sf	8911
692	7/28	1249	2	sf	8911
693	7/28	1301	1	1f	8907
694	7/30	2210	2	sn	8905
695	7/31	0832	2	1n	8905
696	7/21	0946	1	1f	8905
697	7/21	1110	1	sf	8901
698	7/6	2007	2	--	--
700	7/23	1247	1	1b	8907
701	7/23	1300	2	1b	8907

UM/RAO Event No.	Date	Start Time (U.T.)	4-2 MHz Importance	Assoc. Flare Imp.	Assoc. Plage Region
702	7/23/67	1556	2	sb	8907
703	7/23	1650	1	sf	8901
704	7/23	1815	1	sb	8907
705	7/26	1531	1	sn	8907
706	7/26	1621	1	sn	8905
707	7/26	1746	2	sn	8905
708	7/26	2105	1	sn	8907
709	7/26	2212	1	sf	8907
711	7/26	2244	2	sn	8905
712	7/31	1507	1	sn	8905
713	7/31	2049	2	1b	8905
714	7/31	2054	3	1b	8905
752	8/4	0225	2	--	--
753	8/4	0236	1	--	--
758	8/12	1702	1	2n	8926
759	8/12	1842	1	--	-
760	8/12	2109	1	sn	8921
761	8/14	0205	2	sn	8921
763	8/14	0824	4	1n	8921
766	8/19	0002	1	2n	8942
769	8/26	0008	1	1b	8949
771	8/26	1045	1	sn	8942

UM/RAO Event No.	Date	Start Time (U.T.)	4-2 MHz Importance	Assoc. Flare Imp.	Assoc. Plage Region
772	8/26/67	1809	2	sf	8942
773	8/26	1936	2	sn	8942
774	8/26	2305	2	sn	8942
775	8/26	2310	1	sn	8942
778	8/30	0324	1	1n	8942
802	9/3	0302	3	sn	8960
806	9/10	1739	1	sb	8972
807	9/11	2323	1	--	--
811	9/29	2225	2	--	--
1101	3/30/68	0036	3	--	--
1151	4/2	1615	2	--	--

APPENDIX II

MEASURED PHYSICAL PROPERTIES OF SELECTED LOW-FREQUENCY SOLAR BURSTS

UM/RAO Event Number	Drift Rate (MHz/sec)	Duration (sec)					Maximum Flux Density (watt $m^{-2} Hz^{-1}$)	Integrated Flux Density Over 4-2 MHz Band (joule m^{-2})
		4.0 MHz	3.5 MHz	3.0 MHz	2.5 MHz	2.0 MHz		
2	0.111	I[11]	10.2	14.8	15.6	16.2	1.60×10^{-17}	7.48×10^{-11}
4	I	I	14.4	15.1	20.6	23.7	1.31×10^{-17}	1.01×10^{-10}
37	0.125	16.5	19.0	21.9	27.2	I	1.44×10^{-16}	1.43×10^{-9}
59a	I	I	22.9	I	I	I	5.03×10^{-17}	7.38×10^{-10}
59b	0.059	I	43.1	I	I	I	2.50×10^{-17}	5.56×10^{-10}
66	0.125	12.0	14.0	14.6	I	I	3.71×10^{-16}	4.24×10^{-9}
80	0.063	I	26.1	28.6	33.1	40.6	3.94×10^{-16}	4.50×10^{-9}

[11] "I" indicates data which is distorted to such an extent that a measurement is indeterminate.

UM/RAO Event Number	Drift Rate (MHz/sec)	Duration (sec)					Maximum Flux Density (watt $m^{-2} Hz^{-1}$)	Integrated Flux Density Over 4-2 MHz Band (joule m^{-2})
		4 0 MHz	3. 5 MHz	3 0 MHz	2. 5 MHz	2.0 MHz		
104a	I	22. 7	23. 4	24. 7	N[12]	N	2.25×10^{-16}	2.34×10^{-9}
104b	0 125	15. 3	18. 2	I	N	N	1.10×10^{-15}	$1\ 65 \times 10^{-8}$
155	0 125	I	10. 9	11. 7	N	N	$6\ 21 \times 10^{-16}$	6.76×10^{-9}
159	0. 125	15 1	16. 0	16. 1	18. 5	21. 9	3.51×10^{-16}	4.26×10^{-9}
160a	0 125	I	12. 0	I	I	I	1.76×10^{-16}	2.00×10^{-9}
160b	0 125	I	16. 0	I	I	I	2.42×10^{-16}	3.00×10^{-9}
209	0 063	17. 8	20. 4	21. 4	N	N	3.12×10^{-16}	4.26×10^{-9}
217	0 077	I	8. 2	I	N	N	7.36×10^{-16}	7.34×10^{-9}
328	0. 100	4. 4	7. 9	9 4	N	N	5.03×10^{-17}	2.56×10^{-10}
329a	I	I	21. 4	I	N	N	9.48×10^{-17}	5.40×10^{-10}
329b	0. 050	21. 5	23. 1	24. 6	N	N	8.67×10^{-16}	2.56×10^{-8}

[12] "N" indicates that no measurements were made by the experiment for the frequency in question.

UM/RAO Event Number	Drift Rate (MHz/sec)	Duration (sec)					Maximum Flux Density (watt $m^{-2} Hz^{-1}$)	Integrated Flux Density Over 4-2 MHz Band (joule m^{-2})
		4.0 MHz	3.5 MHz	3.0 MHz	2.5 MHz	2.0 MHz		
452	0 125	I	30.9	I	N	N	3.12×10^{-16}	4.00×10^{-9}
454	0 100	I	31 2	40.8	N	N	1.93×10^{-16}	1.79×10^{-9}
461a	I	38 0	60.3	I	N	N	4.20×10^{-17}	5.08×10^{-10}
461b	0.067	I	24.6	I	N	N	8.44×10^{-18}	9.86×10^{-11}
474	0 200	I	10.7	I	N	N	6.57×10^{-16}	5.60×10^{-9}
477	0 143	I	20.2	I	N	N	4.94×10^{-16}	9.08×10^{-9}
479	0 111	I	67.1	I	N	N	3.12×10^{-16}	1.14×10^{-8}
481	0.125	I	10.2	13.0	N	N	5.03×10^{-17}	2.94×10^{-10}
488	0.053	I	18.9	21.8	N	N	8.10×10^{-17}	1.08×10^{-9}
501	0.091	I	28 3	30.0	N	N	4.68×10^{-16}	$8\ 76 \times 10^{-9}$
503	0.100	I	21 1	I	N	N	5.89×10^{-17}	3.26×10^{-10}
504	0.071	I	52.9	I	N	N	1.27×10^{-16}	1.39×10^{-9}
514	0.071	44.3	53.8	I	N	N	2.75×10^{-16}	4.92×10^{-9}

UM/RAO Event Number	Drift Rate (MHz/sec)	Duration (sec)					Maximum Flux Density (watt $m^{-2}Hz^{-1}$)	Integrated Flux Density Over 4-2 MHz Band (joule m^{-2})
		4.0 MHz	3.5 MHz	3 0 MHz	2.5 MHz	2.0 MHz		
560	0.071	13.5	15.1	I	N	N	2.10×10^{-16}	1.86×10^{-9}
614	0.200	I	10.1	14.4	N	N	8.10×10^{-17}	5.56×10^{-10}
676	0.143	I	22.5	26.5	N	N	1.05×10^{-17}	1.20×10^{-10}
678	0.143	27.5	33.4	I	N	N	2.76×10^{-16}	3.14×10^{-9}
680	0.091	I	10.0	11.9	N	N	4.88×10^{-18}	3.38×10^{-11}
683	0.100	32.0	40.1	I	N	N	9.48×10^{-17}	7.38×10^{-10}
684	0.200	18.7	22.3	29 4	N	N	2.42×10^{-16}	$2\ 26 \times 10^{-9}$
686	0.167	5.8	8.2	I	N	N	9.15×10^{-16}	$7\ 84 \times 10^{-9}$
687	0.125	I	15.9	I	N	N	$4\ 94 \times 10^{-16}$	5.18×10^{-9}
692	0.200	I	19.7	25.1	N	N	4.20×10^{-17}	3.86×10^{-10}
695	0.143	I	24.0	28.9	N	N	1.58×10^{-16}	1.30×10^{-9}
1101	0.067	28.2	32.9	I	N	N	3.94×10^{-16}	6.44×10^{-9}
1151	0.167	12 3	13.9	I	N	N	5.89×10^{-17}	5.78×10^{-10}

LIST OF REFERENCES

Anderson, K. A., and Lin, R P. 1966, Phys Rev Letters 16, 1121

Arnoldy, R. L., Kane, S R, and Winckler, J. R. 1967, Solar Phys 2, 171

_____ 1968a, Ap J 151, 711

_____ 1968b, "An Atlas of 10-50 keV Solar Flare X-Rays Observed by the OGO Satellites; 5 September 1964 to 31 December 1966", Cosmic Ray Group Report CR-108, University of Minnesota Minneapolis, Minnesota: January, 1968

Bekefi G 1966, Radiation Processes in Plasmas (New York: John Wiley).

Billings, D. E 1966, A Guide to the Solar Corona (New York: Academic Press)

Bohlin, J. D 1968, Unpublished Ph D. Dissertation, University of Colorado

Bohm, D., and Gross, E P 1949a, Phys Rev 75, 1851.

_____. 1949b, Phys Rev 75, 1864

Boischot, A. 1967, Ann d'Ap 30, 85

_____, and Clavelier, B 1967, Astrophys Letters 1, 7

_____, Lee, R H, and Warwick, J W 1960, Ap. J. 131, 61.

de Groot, T, and Van Nieuwkoop, J 1968, Solar Phys. 4, 332

de Jager, C 1965, Ann d'Ap 28, 125.

Elgaröy, Ö. 1961, Astrophys. Norvegica 7, 5.

_____. 1965, Solar System Radio Astronomy, ed J. Aarons (New York: Plenum Press), 201

_____ 1967, Astrophys Letters 1, 13

Erickson, W. C. 1962, General Dynamics/Astronautics Report ERR-AN-233, cited by M. R. Kundu, Solar Radio Astronomy (New York: John Wiley).

_____ 1964, Ap. J. 139, 1290.

Fokker, A. D 1965, Solar System Radio Astronomy, ed. J. Aarons (New York: Plenum Press), 171.

Gillett, F. C., Stein, W A., and Ney, E. P. 1964, Ap J 140, 292.

Giovanelli, R. G. 1959, Paris Symposium on Radio Astronomy, ed R N Bracewell (Stanford, Calif.: Stanford University Press), 214.

Ginzberg, V L. and Zheleznıakov, V V 1958, Soviet Astr. 2, 653.

_____. 1959a, Paris Symposium on Radio Astronomy, ed. R. N. Bracewell (Stanford, Calif : Stanford University Press), 574.

_____ 1959b, Soviet Astr 3, 235.

Goldberg, L. 1967, Annual Review of Astronomy and Astrophysics, Vol. V, ed. L. Goldberg (Palo Alto, Calif.: Annual Reviews, Inc), 279.

Haddock, F. T. and Graedel, T E. 1968, Paper presented at the 127th Meeting of the American Astronomical Society, Victoria, B. C., August 21, 1968.

Hartz, T. R. 1964, Ann d'Ap. 27, 831.

_____, and Warwick, J. W. 1966, Privately circulated manuscript cited in Newkirk, G A., Jr , Annual Review of Astronomy and Astrophysics, Vol. V, ed L Goldberg Palo Alto, Calif : Annual Reviews, Inc), 214.

Hughes, M. P. and Harkness, R L. 1963, Ap J 138, 239.

Jaeger, J. C., and Westfold, K. C 1949, Austr. Journ. Sci. Res , Series A, 2, 322.

Kai, K , McLean, D J., Payten, W J , Sheridan, K. V., and Wild, J. P. 1968, Proc. Astron. Soc. Austr 1, 79.

Krimigis, S. M 1965, Journ Geophys. Res 70, 2943.

Kundu, M R 1963, Space Sci Rev. 2, 438

_____. 1965, Solar Radio Astronomy (New York: John Wiley)

_____, and Haddock, F T 1961, IRE Trans Antennas and Propagation AP-9, 81.

Lin, R P , and Anderson, K. A 1967, Solar Phys 1, 446

Lin, R P , Kahler, S W , and Roelof, E C 1968, Solar Phys 4, 338

MacRae, B D 1968. "Instrumentation for Radio Astronomy Measurements Aboard the OGO-V Spacecraft", NASA Contract NAS5-9099 Technical Report, University of Michigan Radio Astronomy Observatory

MacQueen. R. M 1968, Private communication

Malitson, H H. , Alexander, J K , and Stone, R G. 1968, Paper presented at the Special Meeting on Solar Astronomy of the American Astronomical Society, Tucson, Arizona, February 3, 1968.

Malitson, H H , and Erickson, W C 1966, Ap J. 144, 337

Malville, J. M 1961, Unpublished Ph D Dissertation, University of Colorado

_____. 1962a, Ap J. 135, 834.

_____ 1962b, Ap J 136, 266

Maxwell, A., Howard, W. E III, and Garmire, C 1960, Journ Geophys. Res. 65, 3581

Michard, R. 1954, Ann d'Ap 17, 429.

Montgomery, D. C , and Tidman, D A 1964, Plasma Kinetic Theory (New York: McGraw-Hill)

Neugebauer, M and Snyder, C W. 1966, The Solar Wind (Pasadena, Calif : Jet Propulsion Laboratory and California Institute of Technology), 3.

Newkirk, G A., Jr 1961, Ap. J 133, 983.

_____. 1967, Annual Review of Astronomy and Astrophysics, Vol V, ed L. Goldberg (Palo Alto, Calif.: Annual Reviews, Inc), 214

_____, and Bohlin, J D 1965, Ann. d'Ap. 28, 234.

Ney, E P , Huck, W F , Kellogg, P J , Stein, W., and Gillett, F C 1961, Ap. J. 133, 661

Noble, L M., and Scarf, F L 1963, Ap. J 138, 1169.

Payne-Scott, R , Yabsley, D. E., and Bolton, J G. 1947, Nature 160, 256

Pottasch, S R. 1960, Ap J 131, 68.

Saito, K. 1959, Pub Astron Soc Japan 11, 234.

Sandlin, G. D., Koomen, M J , and Tousey, R 1968, Paper presented at the Special Meeting on Solar Astronomy of the American Astronomical Society, Tucson, Arizona, February 3, 1968.

Schmidt, M. 1953, Bull. Astron Inst. Neth 12, 61.

Shain, C A , and Higgins, C S 1959, Austr J Phys. 12, 357

Sheridan, K. V., and Attwood, C. F 1962, Observatory 82, 155

Slysh, V. I 1967, Soviet Astr 11, 389.

Smerd, S F., Wild, J P , and Sheridan, K. V 1962, Austr. J Phys 15, 180.

Smith, H J , and Smith, E. v P 1963, Solar Flares (New York: Macmillan)

Solar Geophysical Data 1968, U S Department of Commerce, Environmental Science Services Administration, Descriptive Text

Stone, R G , Malitson, H H , Alexander, J K , and Somerlock, C R 1967, NASA TM-X-60475 (Greenbelt, Maryland: National Aeronautics and Space Administration)

Sturrock, P A 1964, AAS-NASA Symposium on the Physics of Solar Flares (Washington, D. C : U. S. Government Printing Office)

Suzuki, S., Attwood, C F , and Sheridan, K V 1964, Observatory 84, 55.

Takakura, T 1963, Pub Astron Soc Japan 15, 462.

_____. 1964, Pub Astron Soc Japan 16, 230

_____ 1967, Solar Phys. 1, 304

Thompson, A. R., and Maxwell, A 1962, Ap J. 136, 546.

Tidman, D A , and Dupree, T H 1965, Phys Fluids 8, 1860.

Van Allen, J A , and Krimigis, S M 1965, Journ Geophys Res. 70, 5737

van de Hulst, H C 1950, Bull. Astron. Inst Neth. 11, 135.

von Kluber, H 1961, M N R A S 123, 61

Warwick, J W 1965, Solar System Radio Astronomy, ed. J. Aarons (New York. Plenum Press), 131

_____ Ap. J 150, 1081.

Weiss, A A , and Wild, J P 1964, Austr. J Phys. 17, 282.

Whang, Y C , Liu, C K , and Chang, C C 1966, Ap. J. 145, 255

Wild, J P 1950, Austr. Journ Sci Res., Series A, 3, 541

_____, and McCready, L L 1950, Austr Journ Sci. Res., Series A, 3, 387

_____, Murray, J D , and Rowe, W C 1954, Austr J. Phys 7, 439

_____, Sheridan, K V , and Neylan, A. A 1959, Austr. J Phys 12, 369

_____, Smerd, S F , and Weiss, A A 1963, Annual Review of Astronomy and Astrophysics, Vol I, ed. L. Goldberg (Palo Alto, Calif. : Annual Reviews, Inc), 291.

Zirin, H. 1966, Nature 212, 909